Nanoelectrochemical sensors for kinetic measurements and electroanalytical chemistry

By

Yixian Wang

A dissertation submitted to the Graduate Faculty of Chemistry in partial fulfillment of the requirements for the degree of Doctor of Philosophy, The City University of New York

2013

This manuscript has been read and accepted for the
Graduate Faculty in Chemistry in satisfaction of the
dissertation requirement for the degree of Doctor of Philosophy.

Prof. Michael Mirkin

_____ _____

Date Chair of Examining Committee

Prof. Maria C. Tamargo

_____ _____

Date Executive Officer

Prof. Malgorzata Ciszkowska

_____

Prof. Dan Steingart

_____

Prof. Stephen Feldberg

_____

Supervisory Committee

THE CITY UNIVERSITY OF NEW YORK

Abstract

Nanoelectrochemical sensors for kinetic measurements and electroanalytical chemistry

By

Yixian Wang

Adviser: Prof. Michael V. Mirkin

My PhD research is in the field of nanoelectrochemistry. It includes both fundamental kinetics studies of charge transfer processes and chemical reactions at nanoscopic liquid/liquid and solid/liquid interfaces and applications of the nanometer-sized probes and scanning electrochemical microscopy (SECM) as analytical tools.

Nanopipettes can be used to study kinetics of heterogeneous ion transfer (IT) reactions. Common ion voltammetry was developed for determining the kinetic parameters of the rapid tetraethylammonium transfer at the dichloroethane/water interface. This new type of voltammetry provides two limiting currents corresponding to the ingress of the common ion into the pipette and its egress to the external solution, from which one can evaluate the related geometric and transport parameters. Then, the kinetics of IT processes of tetrabutylammonium and similarly sized but asymmetric 1-methyl-3-octylimidazolium at the water/ionic liquid nanointerface was determined for the first time by employing this new approach.

Nanopipettes were also used as SECM tips to carry out feedback-mode imaging of various substrates with the nanoscale resolution. Quantitative SECM measurements performed with the polished pipettes as small as 8 nm radius at extremely short tip/substrate distances (~1 nm). A new mode of the SECM operation—electron transfer/ion transfer mode—was developed for simultaneous mapping of surface reactivity and topography.

We developed the methodology for resistive-pulse sensing with nanopipettes and used it to detect Au nanoparticles, nanoparticles coated with an allergen epitope peptide layer, and gold particles with bound antipeanut antibodies on the peptide layer. The current pulses produced by

antibody-conjugated particles and either bare gold or Au-peptide nanoparticles occurred at different translocation voltages and exhibited opposite signs of the current change, which is essential for selective resistive-pulse sensing of antibodies with nanopipettes.

I modified Pt nanoelectrodes with platinum black and then used them to detect reactive oxygen and nitrogen species (ROS and RNS) inside macrophages. Our results supported the hypothesis of the ROS/RNS leakage from phagolysosomes. The data also showed that a macrophage can avoid oxidative damage by rapidly reducing ROS/RNS concentration levels in its cytoplasm.

Acknowledgements

First of all, I would like to express my great gratitude and sincere respect to Prof. Michael Mirkin for all his guidance and care though these six years. Prof. Mirkin has always been extremely supportive and has constantly encouraged me whenever I felt not confident and I have always been inspired by his learning and intelligence. With his financial support I have been able to focus all my attention to my research work.

I would like to thank Prof. Malgorzata Ciszkowska, Dr. Stephen Feldberg and Prof. Dan Steingart for serving for my committee and their guidance and interest in my education.

I am grateful to Prof. Takashi Kakiuchi, Prof. Shigeru Amemiya, Prof. Christian Amatore and Prof. James F. Rusling for their guidance and help on our collaborative projects.

I would like to express my thanks to Dr. Peng Sun, Dr. François O. Laforge, Dr. James Carpino, Dr. Jeyavel Velmurugan, Dr. Dongping Zhan, Dr. Kaan Kececi, Dr. Wojciech Nogala, Dr. Jean-Marc Noël, Mr. Yun Yu and Ms. Pansy Elsamadisi, who have been working with me and helping me during the past six years.

The financial support from the City University of New York is deeply appreciated.

I would like to express my gratitude to Prof. Rose Kfar Rose for her generosity.

Finally I would like to thank my parents who have always been loving me and supporting me.

Table of content

List of Tables

List of Figures

Chapter I

Nanoelectrochemical sensors

1.1 Introduction

My PhD research is in the field of nanoelectrochemistry. It includes both fundamental kinetics studies of charge transfer processes and chemical reactions at nanoscopic liquid/liquid and solid/liquid interfaces and applications of the nanometer-sized probes and scanning electrochemical microscopy (SECM) as analytical tools.

Nanometer-sized pipettes have been an essential tool in my PhD research, which are pulled from borosilicate or quartz capillaries using a laser puller. A nanopipette offers several important advantages including the ease of fabrication, small physical size (the outer diameter of the pipette tip can be as small as ≤10 nm)[1], and the needle-like geometry, which makes it suitable as a probe for scanning probe microscopies.[2-5] I used them for fundamental kinetics studies of charge transfer processes at the nanoscopic liquid/liquid interface,[6-7] as well as for resistive-pulse sensing[8] and high-resolution imaging by SECM[9-11].

Another important nanoelectrochemical sensor is nanometer-sized platinum electrode. The fabrication process is more complicated. 25-μm annealed Pt wires are pulled into borosilicate glass capillaries under vacuum with the help of laser puller. After pulling, the electrodes are polished to expose the metal surface and also to make an extremely flat surface.[12] I used platinized platinum electrode to detect the redox species inside macrophages.[13] The details of the fabrication and more applications of platinum nanoelectrodes have been dicussed previously[14] and will not be covered in this thesis.

1.2 Fabrication, silanization and characterization of nanopipettes

1.2.1Fabrication Conditions

Nanopipettes can be fabricated by pulling borosilicate or quartz capillaries with a laser-based pipette puller (P-2000, Sutter Instrument Co.). In some cases, those capillaries need to be cleaned in piranha solution before pulling for better results (see Chapter IV, page 110). Choosing the proper capillaries for every experiment is essential. Several factors need to be considered: the material (quartz or borosilicate); properties of a specific capillary (thickness of the wall, with or without filament).

Borosilicate has low melting point and requires HEAT between 300~400 while quartz requires HEAT between 550~900. Borosilicate is easier to work with because the glass properties change gradually with temperature. However, because of the softness of the material it is difficult to produce ultra-small nanopipettes with relatively short taper (for achieving a relatively small resistance). We prefer quartz in most cases because it is easier to make very small but at the same time not very long pipettes with harder materials. The shortcoming of quartz is that it's very sensitive to uneven heating which might result in unsymmetrical pipettes. In this case, using quatz capillaries with thicker wall ($\geq$0.5mm) would help.[15]

For all the experiments, nanopipettes need to be filled completely with one solution. During this process, the filament inside a nanopipette helps to induce aqueous solution to the end of the tip, otherwise it would be very difficult to remove the air or bubbles and to fill the nanopipettes completely. Therefore in most cases we chose capillaries with filaments. Capillaries without filaments were used in the case that organic solution was present in the pipette since with organic solution it is relatively easy to fill the pipettes and at the same time no filament in the pipette can slow down the evaporation speed (see Chapter III).

The pulling process is controlled by adjusting five pulling parameters in the program, which are HEAT, FILAMENT, VELOCITY, DELAY and PULL. Adjusting parameters for pulling is a complicated process. Sutter instrument Co. provides detailed instructions through their technical support. Generally speaking, to obtain smaller tips, one can increase the value of HEAT, VELOCITY or PULL, or decrease the value of FILAMENT or DELAY. To control the length of the taper while maintaining the nanometer size, one can try to limit the value of VELOCITY and increase PULL at the same time. More than one line of programming can be used to achieve better results.[15]

1.2.2 Silanization

Silanization of the outer wall. When a water-filled pipette is immersed in an organic solution a thin aqueous film forms on its hydrophilic outer wall making the true area of the liquid/liquid interface much larger than the geometrical area of the pipette orifice.[16] The film formation can be avoided by silanizing the outer pipette wall to render it hydrophobic while keeping the interior wall nonsilanized. This was always done by dipping the pipette tip into a silanizing agent (chlorotrimethylsilane) while passing a flow of argon through the pipette, which is straightforward micrometer-sized pipettes, but not very easy for nanopipettes.[4,17] One of my projects employing a high-resolution SEM showed that silanization results in a formation of a nm-thick film on the pipette wall.[6b] Typically, such a film does not affect the response of a relatively large (e.g., ≥100 nm) pipette. Silanization of smaller pipettes must be done cautiously to avoid the formation of a film on the inner wall, which can partially block the pipette orifice and induce solvent penetration into its narrow shaft. A new protocol for silanizing pipettes in the vapor phase allows one to avoid oversilanization of relatively small (e.g., ~10 nm radius)

pipettes (see details in Section 2.1.3). However, the possibility of silanizing smaller (e.g., 1 – 5 nm[1b]) pipettes is uncertain.

Silanization of the inner wall. When the pipette is filled with organic solution and immersed in aqueous solution, the inner wall of the pipette needs to be silanized to avoid aqueous solution getting drawn into the pipette, which can be done by dipping the pipetts tip into chlorotrimethylsilane for 5−7 s.[9,10] In this case, both the outer and inner wall of the pipette gets silanized but it has been proven that unlike aqueous solution, organic solution is not likely to form a layer outside wall even though the wall has become hydrophobic[16]. A more controlled method was used in our recent paper.[11] Briefly, the pipettes were fixed in a mini-vacuum desiccator, which was first evacuated by the pump and then the silane vapour was delivered from the flask to the desiccator, where the pipettes were exposed to it for about 15 minutes. (see Section 3.2.4 for details.)

1.2.3 Characterization of the nanopipettes

Nanopipettes with radius smaller than 1μm cannot be seen clearly under normal optical microscope, therefore we normally use electrochemical methods to obtain the geometric information of nanopipettes. Steady-state voltammetry of ion transfer at the interface between two immiscible electrolyte solutions (ITIES) can be used to evaluate the radius of a nanopipette according to the following equation:

$$i = 4xz_iFDca \tag{1.1}$$

where z_i, D and c are the charge of the transferred ion i, its diffusion coefficient and bulk concentration in the external solution (usually 1,2-Dichloroethane (DCE)), respectively; and x is a function of r_g/a, which was tabulated[17, 18] and expressed by an analytical approximation for disk-shaped interfaces.[19] Example of voltammograms will be shown in following chapters.

1.3 Kinetic Studies at the ITIES [20]

1.3.1 Theory

After several decades of intensive studies, the questions about the magnitudes of rate constants of rapid heterogeneous ion transfer (IT) reactions remain open. The fabrication of nanometer-sized nanopipettes enabled electrochemical studies of rapid charge transfer processes at liquid/liquid nanointerfaces. Nanoelectrochemical techniques offer numerous advantages such as fast mass-transfer rate and simplified analysis of data obtained under steady-state conditions. At the same time, kinetic data obtained at nanointerfaces may be affected by double layer effects, deviations from classical electrochemical theory, and other size-related phenomena.

Determination of kinetic parameters of heterogeneous IT processes, i.e., standard heterogeneous rate constant ($k°$) and transfer coefficient (α) have been approached by nanoelectrochemical methods. Butler-Volmer equation is commonly used to express the rates of IT at ITIES at relatively low overpotentials. The IT rate constant can be measured only if it is smaller than or comparable to the mass transfer coefficient, m. For uniformly liquid/liquid interfaces, the mass transfer coefficient can be defined as[21]

$$m = i_d/(nFAc^*) \qquad (1.2)$$

where i_d is the characteristic mass transfer current for a specific electrochemical method, e.g., diffusion limiting current in steady-state voltammetry, n is the number of transferred charges, F is the Faraday constant, A is the interfacial area, and c^* is the bulk concentration of the reactant. For a disk-type interface under steady-state conditions, $m \sim D/a$, where a is the tip radius. Thus, an important feature of nanopipette-supported liquid interfaces is a very high steady-state mass-transfer rate. For example, with $D = 10^{-5}$ cm^2/s, a =10 nm corresponds to m = 10 cm/s. This gives the upper limit for the determinable rate constant of ~50 cm/s. Eq. (1.3) describes the

shape of a steady-state voltammogram at any uniformly accessible electrochemical interface (i.e., when the surface concentrations and diffusion fluxes of electroactive species are uniform over the entire interfacial area):[21]

$$\frac{i}{i_d} = \frac{1}{\theta + m_O \exp[\alpha nF(E - E^{\circ\prime})/RT]/k^{\circ}} \tag{1.3}$$

where $\theta = 1 + \exp[nF(E-E^{\circ\prime})/RT]m_O/m_R$. m_O and m_R represent the mass-transfer coefficients of the transferred ion in two liquid phases, E is the interfacial voltage and $E^{\circ\prime}$ is the standard IT potential.

For a non-uniformly accessible disk-shaped interface, an analytical approximation analogous to Eq. (1.3) is[22]

$$i/i_d = \theta^{-1}\left[1+\frac{\pi}{\kappa'\theta}\frac{2\kappa'\theta + 3\pi}{4\kappa'\theta + 3\pi^2}\right]^{-1} \tag{1.4}$$

where $\kappa' = \frac{\pi\lambda}{4}\exp[-\alpha nF(E-E^{\circ\prime})/RT]$, a is the disk radius, $\lambda = k^{\circ}a/D$, and i_d is given by Eq. (1.5)

$$i_d = 4nFDac^* \tag{1.5}$$

It's the advantages of steady-state voltammetry over the transient methods include the absence of the limitations caused by the charging current and ohmic potential drop, insensitivity to low levels of reactant adsorption, and relative simplicity of data acquisition and analysis. The size of a nanointerface is the origin of these advantages and also of numerous technical difficulties. The smaller the electrode the harder it is to determine its size and shape. Other issues including possible edge effects and deviations from classical electrochemical theory may affect the results of kinetic measurements at nanopipettes.

1.3.2 Analysis of steady-state voltammograms

In most published experimental studies of ET or IT at nanointerfaces the kinetic parameters were determined either by fitting steady-state voltammograms to the theory or by using a three-point method.[23]

Three-point method. Unlike transient methods, the theory used for analysis of steady-state voltammograms is relatively simple. A three-point method[23] based on measurements of the differences between the half-wave potential ($E_{1/2}$) and two quartile potentials, at which the current equals to ¼ and ¾ of the diffusion limiting current ($\Delta E_{1/4} = |E_{1/2} - E_{1/4}|$ and $\Delta E_{3/4} = |E_{3/4} - E_{1/2}|$) was frequently used to extract k^o and α from quasi-reversible steady-state voltammograms of IT at nanointerfaces.[1, 4, 17, 24] The analysis is fast, simple, and suitable for any kind of uniformly accessible interface or for disk-type geometry; however, its application to nanoelectrode voltammetry requires extra care both experimentally and theoretically. The precise extraction of quartile potentials is only possible if a voltammogram is very well shaped and unaffected by background current, noise, or other experimental artifacts—a stringent requirement for a nanoelectrode voltammogram with a low-pA or sub-pA diffusion limiting current. From the $\Delta E_{1/4}$ and $\Delta E_{3/4}$ values alone one cannot detect imperfections in the shape of the voltammogram caused by uncompensated resistance, electrode surface fouling, and other experimental problems. To ensure that the extracted kinetic parameters are meaningful, one must use them to calculate theoretical steady-state voltammograms and check that they are in accordance with the experimental curves; this has not been done in most published studies. Moreover, for near-Nernstian voltammograms, very small uncertainties in measured quartile potentials may result in highly inaccurate values of kinetic parameters. This issue is similar to that of finding the unique fit between theoretical and experimental voltammograms (see below).

Fitting experimental voltammograms to the theory. An alternative and much better approach is to use a curve-fitting computer program to fit the entire experimental voltammogram to equations for IT at the nano-ITIES.[1a] k^o and α (and typically $E^{o\prime}$) are used as adjustable parameters to be determined from the best fit. It was shown previously that a steady-state voltammogram is quasi-reversible when the dimensionless standard rate constant, $\lambda = k^{\circ}a/D$ is $\lesssim$ 10; and kinetic parameters of interfacial charge transfer (CT) can, in principle, be extracted by fitting such a curve to the theory.[22,23] However, this approach works well only if the shape of a voltammogram depends strongly on the values of kinetic parameters. For near-Nernstian CT processes (i.e., $\lambda \gtrsim 1$), the same experimental voltammogram can be fit to the theory using different combinations of kinetic parameters with only minor adjustments in $E^{\circ\prime}$.[6] An example given in Fig. 1.1 for IT of TEA^+ at an ITIES shows a completely satisfactory fit obtain with different k^o (from to 1.2 to 4.3 cm/s) and α (from 0.2 to 0.7) values.

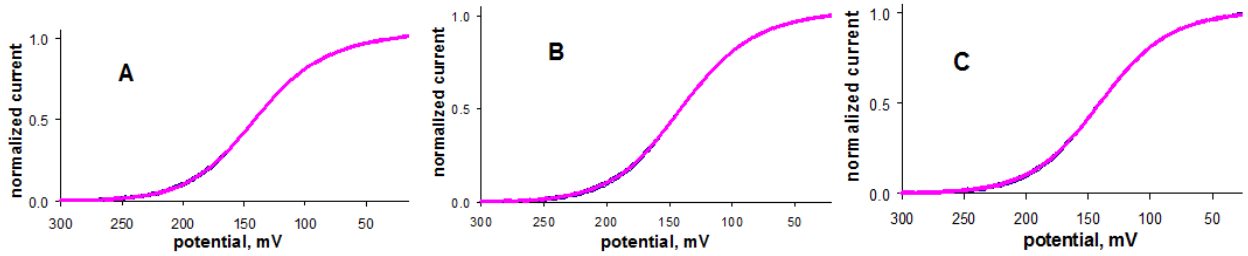

Figure 1.1. An experimental steady-state voltammogram of TEA^+ transfer from external DCE phase to the aqueous solution (solid line) fitted to the theory (symbols) using different combinations of kinetic parameters. k^o, cm/s and α: 4.3 and 0.2 (A); 3.6 and 0.4 (B); 1.2 and 0.7 (C).[20]

Common ion IT voltammetry. A simple modification will be shown in Chapter II, which greatly improves the accuracy and precision of CT kinetic measurements by steady-state voltammetry. For IT at the liquid/liquid interface, this approach—common ion voltammetry—is based on the addition of a transferable ion to both liquid phases, i.e., the filling solution inside

the pipette and the external solution.[6a] The advantages of common ion voltammetry over the conventional protocol, in which a transferable ion is initially present only in one liquid phase, stem from the availability of two waves corresponding to the ingress of the common ion into the pipette and its egress to the external solution.[6b] From two limiting currents of a single voltammogram one can assess asymmetric ion diffusion in the internal and external solutions and evaluate the related geometric and transport parameters.

1.3.3 IT rates at nano-ITIES.

The first rapid IT reaction studied at a nanopipette-supported ITIES was the transfer of potassium ion across the water/1,2-dichloroethane (DCE) interface facilitated by dibenzo-18-crown-6 (DB18C6).[1a] Subsequently, steady-state voltammetry at nanopipettes has been employed to study rapid kinetics of both simple IT and FIT processes; [1, 4,6b, 17, 24] the reported kinetic parameters are summarized in Table 1.1.

1.3.4. Effects of charged glass surface on mass-transfer and IT rate.

Kinetic analysis of nanopipette voltammograms can be further complicated by electrostatic effects produced by the negatively charged inner glass wall.[6b] The surface charge can influence ion transport along the wall electrostatically and also affect the IT rate at the edge of the nano-ITIES. Various effects of the surface charge and electrical double layer present at the inner wall including current rectification,[25,26] accumulation or depletion of ions near the orifice,[27,28] and electrostatically gated transport[29] have been investigated theoretically and experimentally for nanopipettes and glass nanopore electrodes immersed in an aqueous electrolyte solution (i.e., single-phase systems with no liquid/liquid interface). Also, double layer effects at the nanoscopic ITIES, where the diffusion layer thickness is comparable to that of the diffuse double layer, may result in deviations from the conventional electrochemical theory.

Table 1.1 IT kinetic parameters measured at nano-ITIES.[20]

ion	IT process	k^o, cm/s	α	nanopipette, *a* (nm)	data analysis	ref.
K^+	FIT from water to DCE with DB18C6	1.3 ± 0.6	0.4 ± 0.1	nonsilanized quartz 5 – 250	three-point method and curve fitting	1a
Li^+	FIT from water to DCE with DB18C6	0.38 ± 0.24	0.59 ± 0.17	nonsilanized quartz 75 – 898	three-point method	17
		0.34 ± 0.20	0.83 ± 0.17	silanized quartz		
Na^+		1.24 ± 0.34	0.53 ± 0.26	nonsilanized quartz 20 – 320		
		0.94 ± 0.37	0.36 ± 0.08	silanized quartz		
K^+		1.71 ± 0.26	0.67 ± 0.10	nonsilanized quartz 31 – 173		
		1.73 ± 0.49	0.54 ± 0.24	silanized quartz		
Rb^+		0.71 ± 0.33	0.61 ± 0.15	nonsilanized quartz 37 – 595		
		0.68 ± 0.20	0.55 ± 0.24	silanized quartz		
Cs^+		0.22 ± 0.10	0.66 ± 0.04	nonsilanized quartz 132 – 383		
		0.29 ± 0.05	0.45 ± 0.08	silanized quartz		
K^+	FIT from water to DCE with DB18C6	0.9 ± 0.4	0.4 ± 0.1	silanized quartz 67.5 – 150.2	three-point method and curve fitting	4
		0.7 ± 0.2	0.4 ± 0.07	nonsilanized quartz 67.5 – 150.2		
TEA^+	simple IT from DCE to water	2.1 ± 0.2	0.70 ± 0.04	silanized borosilicate 15 – 148		
	simple IT from water to DCE	2.3 ± 0.5	0.6 ± 0.1	silanized borosilicate 65 – 123		
TMA^+	simple IT from DCE to water	1.5 ± 0.3	0.60 ± 0.04	silanized borosilicate 19 – 257		
LA^-	simple IT from water to *n*-octanol	0.24 ± 0.05	0.71 ± 0.24	nonsilanized quartz 42 – 71	three-point method	24
	simple IT from water to DCE	1.35 ± 0.65	0.74 ± 0.10	nonsilanized quartz 28 – 55		
TEA^+	simple IT from water to DCE	110 ± 23	0.57 ± 0.08	nonsilanized quartz 1.2 – 3.2	three-point method	1b
K^+	FIT from water to DCE with DB18C6	95 ± 31	0.56 ± 0.13	nonsilanized quartz 1.1 – 2.0		
ClO_4^-	simple IT from water to DCE	35 ± 8	0.63 ± 0.05	nonsilanized quartz 1.0 – 5.2		
TEA^+	simple IT between water and DCE	6.1 ± 0.9	0.49 ± 0.09	silanized quartz 9.7 – 33	common-ion voltammograms fitted to theory	6b

In nanopipette voltammetry across the nanoscale ITIES, interfacial transfer of an ion at a few mM bulk concentration produces a pA-range current, which is much lower than that in single-phase experiments. Typically, the potential gradient and the ohmic potential drop inside the pipette are too small for significant electromigration or electroosmotic flow along its charged inner wall.[6b, 30] The electrostatic and double layer effects are more significant for smaller nanopipettes, e.g., $a \leq 5$ nm, and more experiments are needed to check whether they can significantly influence kinetic parameters determined from IT voltammograms.[1b]

1.4 SECM with micro- or nanometer-sized pipette probes[31]

Micropipettes [32,33] and nanopipettes[4] have been used as SECM probes since 1990's. In most SECM applications, the pipette was filled with a solvent (*e.g.*, organic) immiscible with the outer solution (*e.g.*, aqueous), so that a liquid/liquid interface was formed at its tip. This setup is suitable for probing ET and ion-transfer processes across the liquid phase boundary. Alternatively, the same solvent can be used inside and outside the pipette for single-phase experiments.[2] This type of probes is most commonly employed in scanning ion conductance microscopy (SICM)[34] and its combination with SECM.[5] A very small RG of a nanopipette-based probe is advantageous if one has to image a rough solid substrate without crashing the tip or a biological cell.

1.4.1 Ion-transfer (IT) feedback mode.

In IT experiments, the tip current is produced by the transfer of an ion across the liquid/liquid interface, which could either be facilitated ion transfer [35] or simple ion transfer.[10] This current decreases when the tip is brought close to a solid substrate, which blocks the diffusion of the transferable ion (or ionophore) from the bulk solution to the pipette tip. The theory developed for the IT feedback mode is similar to the conventional SECM feedback theory, and the quantitative agreement between theoretical and experimental current-distance curves was demonstrated for nanopipette tips.[4]

Ishimatsu *et al.* used pipette-based amperometric tips to characterize ion-transport properties of ultrathin nanoporous silicon membranes.[36] The reliable measurement of ion-selective permeabilities are needed for better understanding of the structure and successful applications of molecularly thin nanoporous membranes. Conventional heat-pulled glass pipettes were milled using a focused ion beam to obtain smoother, better defined glass tips that could be brought closer to the membrane surface. The membrane permeabilities to small, monovalent ions were determined and shown to be controlled by ion diffusion across water-filled nanopores. In contrast, the experiments with pipette-based tips selective for biomedically important large polyions yielded the membrane permeability values lower than those corresponding to diffusion-controlled permeation.

Zhan *et al*.[35] reported the use of a micropipette-supported ITIES to detect silver ions and investigate their effects on living cells. A micropipette was filled with DCE solution containing calixarene-based silver ionophore (IV) and used as an ion-selective amperometric SECM probe to monitor the local Ag^+ concentration around living fibroblast cells. Both approach curves and images of the uptake and efflux of Ag^+ were obtained and used to indentify several stages of interaction between Ag^+ and fibroblast cells.

In chapter III, imaging of silicon wafer surface using a 106-nm-radius pipette-based tip based on negative feedback mode will be introduced.[9] It will also show that polishing a pipette can improve the quality of approach curves and enable extremely small separation distances[10].

1.4.2 Pipette delivery mode of the SECM.

The possibility of using a micropipette-based SECM tip to deliver a reagent to the substrate surface (*e.g.*, metal ions for local electrodeposition delivered via facilitated IT across the liquid/liquid interface) was first demonstrated by the Mandler group.[37] Lin *et al.* developed the micropipette delivery−substrate collection mode, in which a neutral species partitions from the organic phase inside a micropipette to the external aqueous solution (Fig. 1.2).[38] A micropipette (a = 10 - 15 μm) was used to deliver neutral species (R) to the substrate, where it

was oxidized electrochemically. The substrate current was recorded to produce a reactivity map while the micropipette was scanned laterally over its surface. This new approach enabled SECM imaging of heterogeneous reactions of neutral species such as FcMeOH oxidation and benzoquinone reduction and also electrocatalytic processes such as the oxidation of formic acid. It was used to study electrocatalytic oxidation of methanol, which could not be probed in the tip generation/substrate collection mode because methanol cannot be generated electrochemically. In this way, arrays of different catalysts were screened in order to find the most efficient bimetallic catalyst for this process—$Pt_{0.8}Ce_{0.2}$.[38] A somewhat similar setup, in which both inner and outer solutions were aqueous, and a redox mediator diffused out of the pipette, was introduced earlier by Walsh *et al.*[39]In that work, a Au ring electrode was formed around the pipette orifice and used for feedback mode measurements.

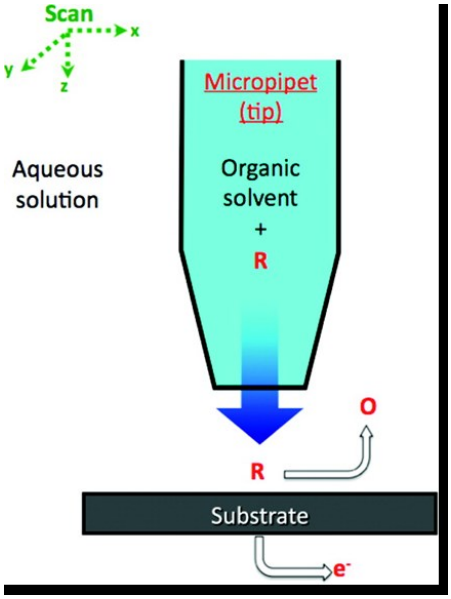

Figure 1.2. Schematic representation of the micropipette delivery−substrate collection mode of the SECM operation. [38]

Williams et al. developed a scanning micropipette contact method (SMCM) for high-resolution imaging of electrode surface redox activity.[40] As shown in Fig. 1.3, a micropipette is brought close to a substrate electrode where the electrolyte solution from the capillary forms a micrometer-thick liquid layer between the pipette tip and the sample surface. Two-electrode

voltammetric experiments were performed by applying voltage between the substrate and the reference electrode inside the pipette. SMCM is capable of probing the localized electroactivity of heterogeneous electrode surfaces (*e.g.*, local rate of trimethylammoniomethylferrocene oxidation in Fig. 1.3). The authors developed a comprehensive theoretical description for this type of experiments and investigated the electroactivity of basal plane of highly oriented pyrolytic graphite and two types of aluminum alloys.

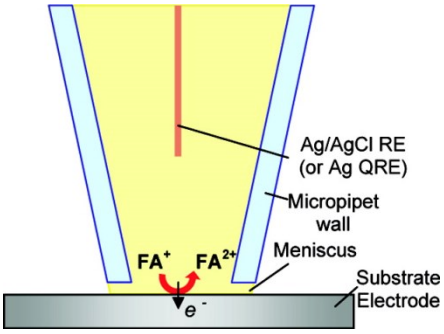

Figure 1.3 Scheme of the SMCM experiment showing an example of the oxidation of trimethylammoniomethylferrocene confined to a small region of a substrate electrode by the micropipette contact method. [40]

1.4.3 SECM/SICM combination.

In SICM, the ionic current flows through the nanopipette tip when one applies voltage between two reference electrodes—one inside and one outside the pipette (both inner and outer solutions are typically aqueous). Similarly to the negative feedback in SECM, this current decreases when the pipette approaches the substrate whose surface blocks the flow of ions to the orifice. With no liquid/liquid interface, most of the applied voltage in SICM drops inside the pipette, and therefore a typical approach curve shows very small decrease in the tip current (*e.g.*, ~1% as opposed to a typical 50 – 90 % decrease in a negative feedback SECM experiment). The absence of the liquid interface also results in a generally higher current, relatively small noise, and significantly simpler probe handling as compared to SECM with pipette-based tips; all these factors contribute to high quality of nanoscale topographic SICM images.[34] At the same time this technique lacks chemical specificity of the SECM and is not suitable for kinetic measurements.

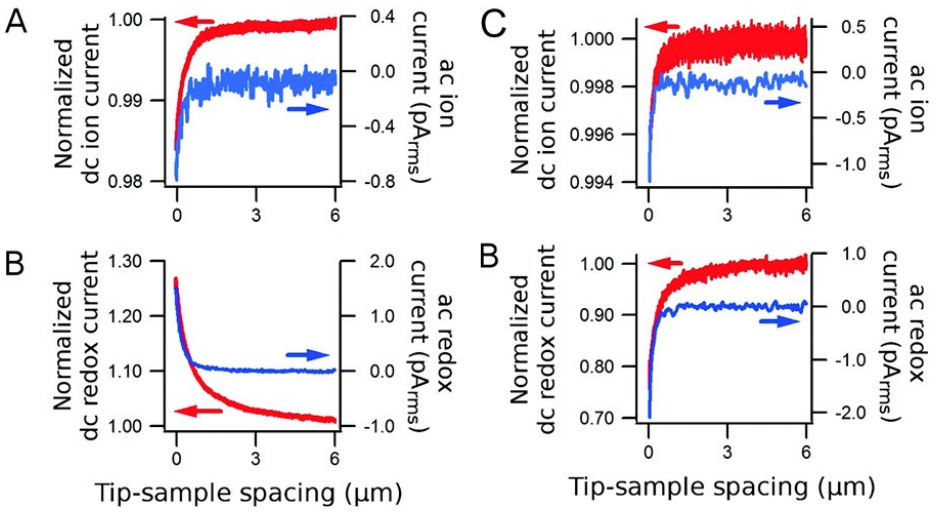

Figure 1.4. Approach curves to a conducting gold (A, B) and insulating Teflon (C, D) surface obtained in 10 mM $Ru(NH_3)_6Cl_3$, 100 mM KNO_3 solution. (A and C) Normalized dc ion current and ac ion current response; (B and D) normalized dc redox current and ac redox current response. [5a]

By integrating SICM and SECM, one can have the best of both worlds. The SICM sensor is used to monitor the tip-substrate distance and produce a topographic image, while the SECM response yields electrochemical information in a constant-distance mode. Comstock *et al.*[5a] fabricated submicrometer-sized pipette probes with an integrated microelectrode for simultaneous SICM and SECM imaging. The authors evaporated gold on the pipette wall, coated it with a layer of aluminum oxide and finally exposed a microelectrode at the tip by FIB milling that resulted in an ~100 nm diameter nanopipette and a ring electrode with an effective radius of ~300 nm calculated from cyclic voltammetry. Fig. 1.4 shows the approach curves obtained at a conducting gold surface (A and B) and an insulating Teflon surface (C and D). As expected, the SICM ionic current was independent of surface reactivity, while SECM curves exhibited positive feedback at Au and negative feedback Teflon surface. Variations in the dc and ac components of the ionic and redox currents were also compared. Integrated SECM/SICM

imaging of a patterned surface was carried out in both feedback and SG/TC modes, and the features as small as ~180 nm were visualized.

Another SECM/SICM system with a pipette/metal ring probe was used to simultaneously image the topography and electrochemical reactivity of two enzymes—horseradish peroxidase (HRP) and glucose oxidase—and single live cells (A6 cells, superior cervical ganglion cells, and cardiac myocytes).[5b] SECM/SICM images of the HRP spot edge are shown in Fig. 1.5. The enzyme was in a PBS solution with 0.50 mM FcMeOH. Top pictures are images obtained before adding H_2O_2 to the solution while the bottom pictures are obtained after. SICM gave clear topographic images in both cases. SECM image shows obvious changes after adding H_2O_2, whose reduction by FcMeOH is catalyzed by HRP.

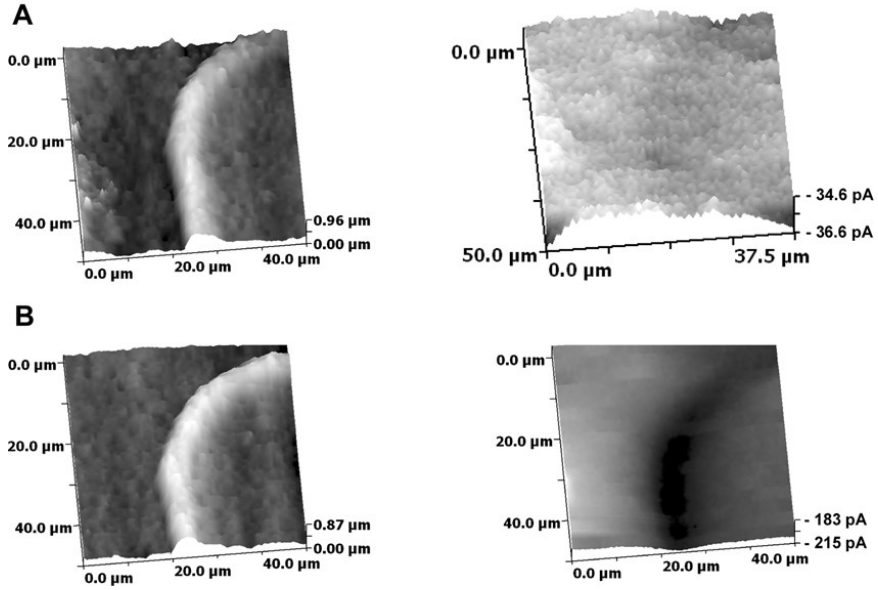

Figure 1.5. Topographic (left) and electrochemical (right) images of a portion of the HRP spot immobilized on a glass substrate (A) before and (B) after adding 0.50 mM H_2O_2 dissolved in 0.50 mM FcMeOH and PBS. The SECM ring-shaped tip and SICM pipette probe were held at 50 and 300 mV vs Ag/AgCl, respectively. [5b]

In Chapter III, a new mode of SECM with nanopipettes will be introduced.

1.6 Nanoelectrochemistry of Living Cells

Nanoelectrodes have been utilized for direct characterization of the intracellular redox state and high-resolution imaging of living cells.[41] It was proven that a small and sharp nanoelectrode (radius ~1,000 times smaller than that of a cell), can penetrate a cell and move inside it without damaging the membrane. The possibility of utilizing nanoelectrodes for studying the transmembrane charge transport and membrane potential and probing redox properties at the subcellular level was also demonstrated.

Fig. 1.6 shows the schematic diagrams of the SECM experiments with single cells. Fig. 1.6A and Fig.1.6B show the measurements which can be done outside the cell membrane. The tip electrode is placed in solution containing a redox mediator and moved toward the surface of a cell. The redox mediator gets oxidized or reduced by the electrode. The product will either cross the cell membrane (hydrophobic) and be reduced or oxidized by intracellular redox reaction (Fig. 1.6A), or stay outside the membrane (hydrophilic), which blocks the diffusion of the original mediator to the tip (Fig. 1.6B). The tip current (i_T) increases in the first case (positive feedback) and decreases in the latter case with distance d (negative feedback). By analyzing the i_T vs. d curves, information about intracellular redox state can be extracted. [42] With a well-polished sharp nanoelectrode ($rg \approx 3a$, Fig. 1.6E), electrochemical measurements can also be done inside living cells (Fig. 1.6C and Fig. 1.6D).

Chapter V will introduce the preparation of platinum deposited sharp Pt nanoelectrodes to enable selective and highly sensitive detection of reactive oxygen species and reactive nitrogen species and the in-vivo and in-situ experiments with activated macrophage.

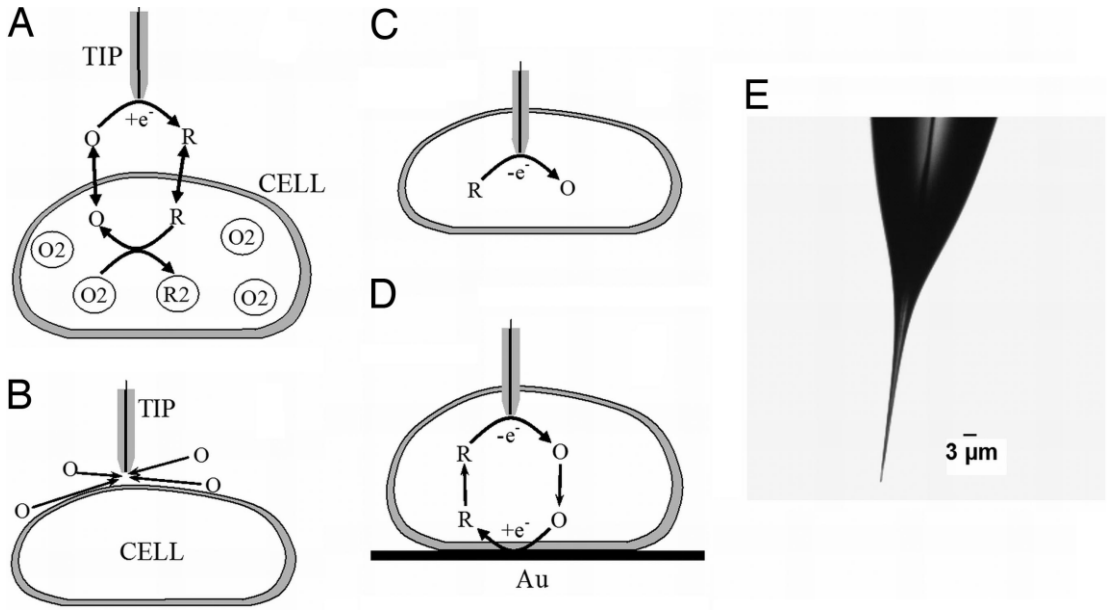

Figure. 1.6. Schematic diagrams of the SECM experiments with single cells (A–D) and an optical micrograph of a typical nanotip used in such experiments (E). (A)The tip is positioned in the solution close to the cell surface. Positive feedback is due to bimolecular electron transfer between hydrophobic redoxmediator (O/R) and cell-bound redox moieties (O2/R2). (B) The lipid cell membrane is impermeable for a hydrophilic redox mediator. Negative feedback is due to the hindered diffusion of redox species to the tip electrode. (C) Nanoelectrode voltammetry inside the cell. (D) Positive feedback is produced by mediator regeneration by way of electron transfer at the underlying Au surface. [41]

Chapter II

Common Ion Voltammetry for Kinetic Study of IT at ITIES

2.1 Kinetic Study of Rapid Transfer of Tetraethylammonium at the DCE/Water Interface

2.1.1 Introduction

Steady-state voltammetry at the pipette-supported liquid/liquid interface has previously been used to measure kinetics of simple and facilitated IT processes. Recently, we showed that the conventional experimental protocol and data analysis produce large uncertainties in kinetic parameters of rapid IT processes extracted from pipette voltammograms. Here, we used a new mode of nanopipette voltammetry, in which a transferable ion is initially present as a common ion in both liquid phases, and improved methodology for silanization of the outer pipette wall to investigate the kinetics of the rapid transfer of the tetraethylammonium cation (TEA^+) at the 1,2-dichloroethane/water interface. This reaction was often employed as a model system to check the IT theory. The determined standard rate constant and transfer coefficient of the TEA^+ transfer are compared with previously reported values to demonstrate limitations of conventional nanopipette voltammetry with a transferrable ion present only in one liquid phase.

IT at the ITIES have been extensively studied because of its intrinsic interest as well as its relevance to many important chemical and biological systems including sensors, batteries, separations, drug delivery systems, and biomembranes.[1-6] Micropipette-based electrochemical probes pioneered by the Girault group[7] as well as later developed nanopipettes[8] have been employed to study these processes. The advantages of small pipette electrodes for studying kinetics of IT reactions include fast mass-transfer rate, negligibly small resistive potential drop,

low double-layer charging current, and simple steady-state measurements.[9] Micropipette voltammetry revealed a broad spectrum of standard heterogeneous IT rate constants, k^0 (from ~10^{-1} cm/s to <~10^{-7} cm/s) for simple transfers of alkyl and perfluoroalkyl oxoanions[10] and facilitated transfers of hydrophilic anions,[11] alkali-earth metal cation,[12] polypeptide protamines,[12, 13] and synthetic heparin mimetic.[14, 15] A higher mass-transfer rate at nanopipettes allows faster facilitated[8, 16] and simple[17-21] IT reactions (e.g., $k^0 \geq 1$ cm/s) to be probed by steady-state voltammetry. Pipette-supported ITIES tips were also employed as probes for SECM to investigate ITs at a large ITIES under enhanced mass-transfer conditions.[22, 23]

The behaviors of tetraalkylammoniums at the interfaces between water and organic solvents—typically, either 1,2-dichloroethane (DCE) or nitrobenzene—have been studied in detail using various approaches including electrochemical methods,[1-4] synchrotron X-ray reflectivity measurements,[24-26] and molecular dynamics simulations.[24, 27] Rapid, mechanistically simple transfers of tetraalkylammoniums have been widely used as model experimental systems for IT studies. In particular, Marcus pointed out that a small standard Gibbs free energy of TEA^+ transfer at a DCE/water interface eliminates the need to take into account large effects of the applied field and the supporting electrolyte, thus, simplifying theoretical treatment.[28] The reported experimental values of of k^0, however, vary dramatically from ~10^{-3} cm/s to ~110 cm/s,[18, 21, 29-37] and there seems to be a strong correlation between the obtained value and the mass-transfer rate of the employed method. In a recent study employing 10–300 nm-radius nanopipettes, $k^0 = 2.3$ cm/s was found from quasi-steady-state voltammetry of the TEA^+ transfer from DCE to the aqueous filling solution, and a very similar value ($k^0 = 2.1$ cm/s) was obtained by steady-state voltammetry for the reverse reaction.[18] The corresponding transfer coefficients, $\alpha = 0.70$ and $\beta = 0.60$,[18] however, are larger than 0.5, and their sum is larger than the theoretically

expected value of 1.[28, 38] More recently, 1.2–3.2 nm-radius pipettes were employed to obtain a k^0 value of 110 cm/s,[21] which seems to be overestimated (see below).

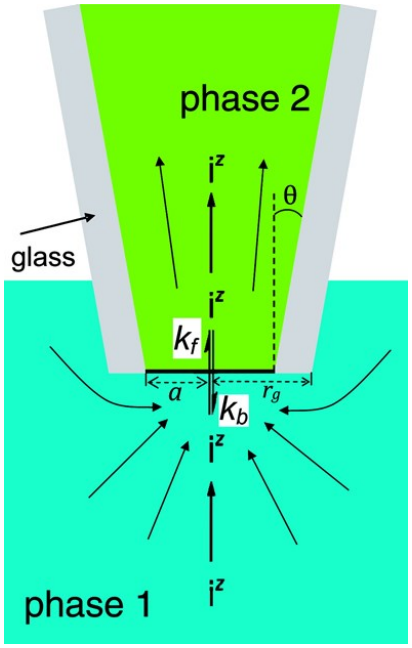

Figure 2.1.1. Scheme of IT and diffusion at a tapered nanopipette.

At first glance, a nanopipette appears to be an extremely simple nanodevice (Figure 2.1.1). It is created in a flash by pulling a quartz capillary, filling it with an aqueous (or organic) solution and immersing in another liquid immiscible with the filling solution. With one reference electrode inserted into the pipette and the second reference in the external solution, the system is ready for experiments. More detailed studies, however, revealed significant complexity of quantitative nanopipette voltammetry, which requires well-defined nanoscopic ITIES formed at the pipette tip. One issue is the formation of a thin aqueous film on the hydrophilic outer wall of the pipette.[22, 39] Such a film appears when a water-filled pipette is immersed in an organic solution and results in the true area of the liquid/liquid interface being much larger than the geometrical area of the pipette orifice. The film formation can be avoided by silanizing the outer pipette wall to render it hydrophobic while keeping the interior wall non-silanized. The

formation of a flat ITIES at the orifice of a silanized micropipette[22, 40] and nanopipette[18] was confirmed by SECM.

The pipette geometry and dimensions strongly affect asymmetric diffusion of ions in the inner and outer solutions and, subsequently, IT voltammograms. The steady-state, quasi-spherical diffusion flux of ions from the external solution to the pipette tip (ingress current) depends on two geometric parameters, the orifice radius, a, and the outer wall radius at the tip, r_g. For micrometer-sized pipettes, both a and r_g can be determined by optical microscopy. For a nanopipette, both parameters can be evaluated by combination of steady-state voltammetry and SECM.[18] On the other hand, the diffusion flux in the internal solution (egress current) depends on the inner tip angle, θ, in addition to the orifice radius. Recent simulations[12, 41, 42] and experiments at micropipettes[12] and nanopipettes[21] showed that θ can be determined from the egress current. However, the results of nanopipette studies of simple ITs are inconsistent: sigmoidal and retraceable steady-state cyclic voltammograms (CVs) were obtained with non-silanized[17, 21] and silanized nanopipettes,[18] while the latter also gave peak-shaped, transient voltammograms of egress TEA^+ transfer.[18] Improved methodology for silanization of nanopipettes discussed below can help to eliminate such artifacts and attain better reliability of nanopipette voltammetry.

In this paper, we employ a new mode of nanopipette voltammetry to study kinetics of rapid TEA^+ transfer at the DCE/water interface. Our recent simulations[43] showed that steady-state pipette voltammograms of a common ion present in both inner and outer solutions comprise positive and negative waves due to ingress and egress ITs. The presence of these two waves enables precise determination of kinetic and thermodynamic parameters along with θ and a values from a single IT voltammogram. Kinetic parameters of the TEA^+ transfer thus

determined are compared with the values obtained previously from conventional nanopipette voltammetry (with TEA^+ initially present only in one liquid phase),[18, 21] and origins of the discrepancies are investigated.

2.1.2 Experimental Setup

Chemicals. The following chemicals were used as received: LiCl and chlorotrimethylsilane from Aldrich; tetraethylammonium chloride (TEACl) from Sigma; potassium tetrakis(4-chlorophenyl)borate (KTPBCl), and tetrahexylammonium chloride (THACl) from Fluka. 1,2-dichloethane (DCE) from Sigma was distilled before use. Tetraethylammonium tetrakis(4-chlorophenyl)borate (TEATPBCl) and tetrahexylammonium tetrakis(4-chlorophenyl)borate (THATPBCl) were prepared by metathesis of KTPBCl with TEACl and THACl, respectively, as described previously.[44] All aqueous solutions were prepared from deionized water (Milli-Q, Millipore Corp.).

Nanopipette Preparation and Characterization by SEM. Nanopipettes were made from 10 cm long quartz capillaries (outer/inner diameter ratio of 1.0/0.70; Sutter Instrument Co., Novato, CA) using a laser-based pipette puller (P-2000, Sutter Instrument Co.) as described previously.[8, 18-20] The outer glass wall of a pipette was silanized to render it hydrophobic. An improved method of nanopipette silanization is described in Results and Discussion. An Olympus BH2 optical microscope was used to inspect all prepared pipettes before measurements.

A field-emission SEM—either Philips Electron Optics XL-30 (image in Fig. 2) or Zeiss Supra 55 VP (images in Fig. 3) was employed to visualize the tips of silanized nanopipettes. Either an ~3 nm-thick Au (Fig. 3) or a 20 nm-thick Pd (Fig. 2) layer was coated on the otherwise insulating nanotip to be imaged without significant charging. A ~1 cm-long tip was cut from the

nanopipette and coated with a Au or Pd layer by sputtering while the tapered end was directed vertically toward the target.

Voltammetric Measurements. Voltammetric experiments were carried out at room temperature (23 ± 2 ºC) in a two-electrode cell:

$$\underset{\text{outer DCE solution}}{\text{Ag|AgTPBCl|}c_{\text{DCE}}\text{ mM TEATPBCl + 9.4 mM THATPBCl||}c_{\text{w}}\text{ mM TEACl + 0.1 M LiCl|AgCl|Ag}}_{\text{pipette}} \qquad \text{(cell 1)}$$

The pipettes were filled with aqueous solution from the rear using a small (10 μL) syringe. CVs were obtained with a BAS 100B/W electrochemical workstation (Bioanalytical Systems, West Lafayette, IN). The voltage was applied between two 0.25-mm-diameter Ag wires coated with either AgCl (aqueous reference inside a pipette) or AgTPBCl (external organic reference). The current produced by the cation transfer from the outer DCE phase to the inner aqueous phase was designated as positive.

2.1.3 Results and Discussion

Silanization and SEM of Nanopipettes. In previous publications, [8, 18-20, 22, 39] the silanization of the outer wall was done by dipping the pipette tip into a silanizing agent (chlorotrimethylsilane) while passing a flow of argon through the pipette. We found that for nanopipettes this method yields less consistent results than for micrometer-sized pipettes and often gives "oversilanized" pipettes as revealed by SEM. The wall of an "oversilanized" pipette is very thick (Figure 2), and $r_g/a \cong 3.9$ is exceedingly large for a pipette pulled from a thin-wall quartz capillary. Consequently, not only the inner tip radius is decreased but also the pipette shaft can be narrowed, which complicates ion diffusion in the internal solution and may impair the data analysis.

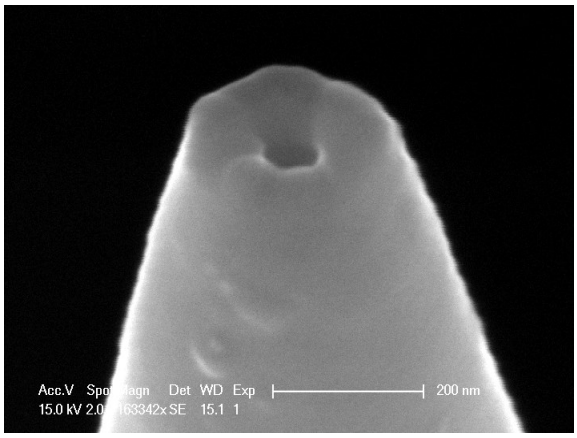

Figure 2.1.2. An SEM image of an "oversilanized" nanopipette.

To avoid oversilanization, we silanized nanopipettes in the vapor of chlorotrimethylsilane. This was done by holding a pipette 1–2 cm above the surface of liquid chlorotrimethylsilane for ~1 min, while the flow of argon was passed through the pipette from the back to avoid silanization of the inner pipette wall. The required silanization time depends on the distance between the chlorotrimethylsilane surface and the pipette, its radius, and room temperature. SEM images of a typical, correctly silanized nanopipette are shown in Figure 3a, where no orifice blocking occurred. The orifice size and shape of the silanized nanopipette are very similar to those of a non-silanized nanopipette (Figure 2.1.3b), which was pulled from the same quartz capillary as a pair of the silanized pipette. This result indicates that the thickness of the hydrophobic surface layer produced by silanization is much smaller than the pipette wall thickness. From a series of SEM images, a typical thickness of this layer is a few nm. This number is negligible for a large (e.g., $a > 100$ nm) pipette, but it may be significant for smaller ($a \sim 20$ nm) pipettes, which require very careful silanization; silanizing very small pipette (e.g., $a < 5$ nm[21]) may be difficult if at all possible. Additionally, side-view images of a correctly silanized nanopipette(data not shown) demonstrate that the pipette barrel has a single taper with an outer

angle of ~18° along the length of >3 μm from the tip, which supports an assumption in our theoretical model.[43] SEM determination of θ, however, was hampered by the pipette wall.

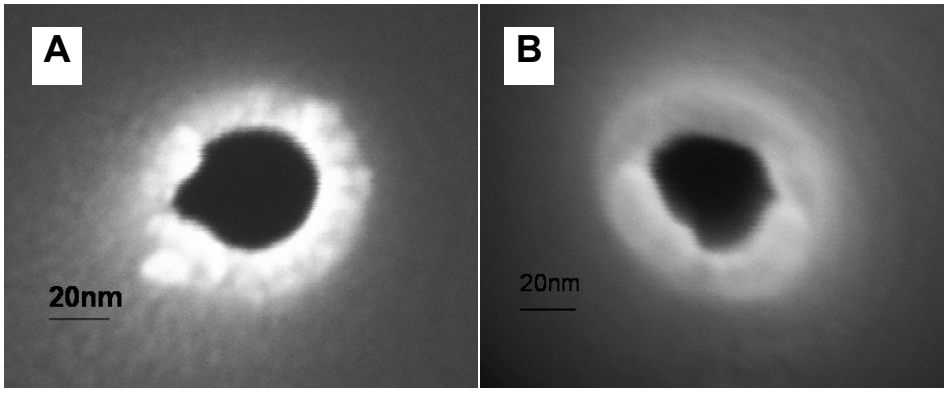

Figure 2.1.3. Top view SEM images of (A) silanized and (B) non-silanized nanopipettes.

Voltammetric Characterization of Silanized and Non-Silanized Nanopipettes. Voltammetry of TEA^+ as a common ion was used to characterize silanized and non-silanized nanopipettes. A pair of pipettes with the same radius was pulled from the same quartz capillary to compare the responses of silanized and non-silanized nanopipettes. Both pipettes were filled with aqueous TEA^+ solution and immersed in a DCE containing TEA^+ to obtain CVs of TEA^+ egress and ingress (Figure 2.1.4). Both forward and reverse waves of the CVs are sigmoidal, thereby confirming steady-state diffusion of TEA^+ on both sides of the nanoscale interface, in agreement with our simulation results.[43] These steady-state voltammograms are not perfectly retraceable, because of capacitive current.

Noticeably, the positive limiting current produced by the ingress of TEA^+ at the non-silanized pipette is ~2.2 times larger than that at the silanized nanopipette. A steady-state diffusion limiting current based on ingress IT is given by

$$i_{ing} = 4xz_iFD_{DCE}c_{DCE}a \qquad (2.1.1)$$

where z_i, D_{DCE} and c_{DCE} are the charge of the transferred ion i, its diffusion coefficient and bulk concentration in the external DCE solution, respectively; and x is a function of r_g/a, which was

tabulated[22, 45] and expressed by an analytical approximation for disk-shaped interfaces.[46] Assuming a disk-shaped interface formed at the tip of the silanized pipette with $r_g/a = 1.5$ for $x = 1.16$,[22, 45] $a = 16$ nm was found from the ingress limiting current using eq 1 with $D_{DCE} = 1.0 \times 10^{-5}$ cm^2/s.[14, 39] This radius is very similar to the radius determined from the positive limiting current at the non-silanized pipette, where formation of a thin water layer on the outer wall results in a larger x value of $3.35\pi/4$.[18] The nearly identical radii of the silanized and non-silanized pipettes are consistent with their originating from the same capillary.

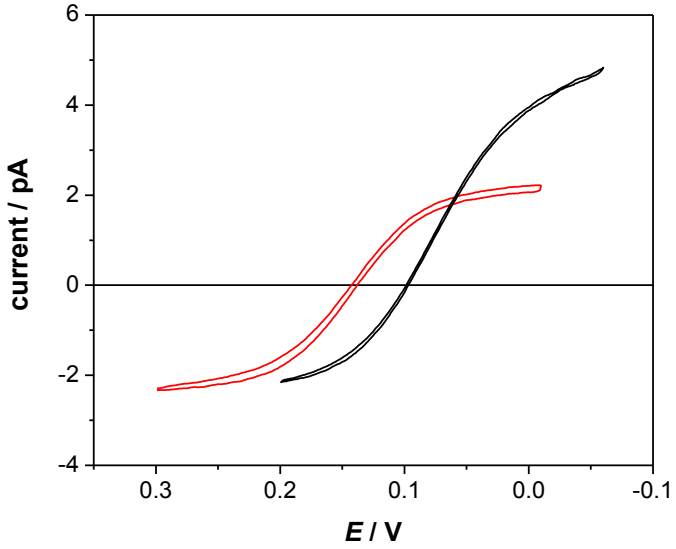

Figure 2.1.4. CVs of TEA^+ transfer across the DCE/water interfaces obtained with a pair of silanized (red) and non-silanized (black) pipettes. The CVs were obtained in cell 1 with $c_w = 0.3$ mM and $c_{DCE} = 2.7$ mM. The CV at the silanized pipette corresponds to entry 2 in Table 2.1. Scan rate was 10 mV/s.

In contrast, similar negative limiting currents were obtained with the pair of the silanized and non-silanized nanopipettes. With a disk-shaped interface formed at the tip of a silanized nanopipette, the corresponding egress limiting current is given by

$$i_{eg} = 4f(\theta)z_iFD_wc_wa \qquad (2.1.2)$$

where D_w and c_w are the diffusion coefficient and bulk concentration in the internal aqueous solution, respectively, and $f(\theta)$ is a tabulated function of the tip inner angle, θ.[12] An analytical approximation for this function

$$f(\theta) = 0.0023113912 + 0.013191803\theta + 0.000317385 96\theta^{1.5} - 5.8554625\times10^{-5}\theta^2 \quad (2.1.3)$$

fits the simulated values over the entire range of θ from 1º to 89º within <1%. With the tip radius determined from the ingress limiting current, the corresponding egress limiting current at the silanized nanopipette yields $f(\theta) = 0.16$ with $D_w = 1.0 \times 10^{-5}$ cm^2/s.[14, 39] According to eq 3, $f(\theta) = 0.16$ corresponds to $\theta = 10°$. The very similar egress currents at the silanized and non-silanized nanopipettes suggest that inner angles of the pair of the nanopipettes pulled from the same capillary are also similar. The geometric quantities, a and θ, are necessary for the determination of kinetic parameters from a nanopipette voltammogram (see below). These parameters control the mass transfer coefficients for ion diffusion in the external (DCE) and internal (aqueous) solutions, respectively, as given by[43]

$$m_{DCE} = \frac{4xD_{DCE}}{\pi a} \quad (2.1.4a)$$

$$m_w = \frac{4f(\theta)D_w}{\pi a} \quad (2.1.4b)$$

For a = 16 nm and $\theta = 10°$, eqs 2.1.4a and 2.1.4b yield m_{DCE} = 9.0 cm/s and m_w = 1.1 cm/s. The m_w value is smaller than m_{DCE}, because the diffusion geometry in the pipette shaft is closer to linear than to hemispherical due to the relatively small taper angle ($f(\theta) << 1$). Importantly, a conventional nanopipette voltammogram obtained with TEA^+ present only in one phase contains either an ingress or an egress wave, so that it is impossible to extract both geometric parameters (and subsequently both m_{DCE} and m_w) from such a voltammogram. Therefore, kinetic parameters

cannot be precisely determined from a single conventional voltammogram if it is affected by ion diffusion in both phases.[43]

It should be noted that CVs of a common ion contain a zero current point, at which the potential (equilibrium potential, $\Delta^{\mathrm{w}}_{\mathrm{DCE}}\phi_{\mathrm{eq}}$) is given by the Nernst equation

$$\Delta^{\mathrm{w}}_{\mathrm{DCE}}\phi_{\mathrm{eq}} = \Delta^{\mathrm{w}}_{\mathrm{DCE}}\phi^{0'}_{\mathrm{TEA}^+} + \frac{RT}{z_{\mathrm{i}}F}\ln\frac{c_{\mathrm{DCE}}}{c_{\mathrm{w}}} \tag{2.1.5}$$

where $\Delta^{\mathrm{w}}_{\mathrm{DCE}}\phi^{0'}_{\mathrm{TEA}^+}$ is the formal potential of the TEA^+ transfer. (The difference between $\Delta^{\mathrm{w}}_{\mathrm{DCE}}\phi_{\mathrm{eq}}$ values in CVs obtained with silanized and non-silanized nanopipettes in Figure 2.1.4 is due to the use of different organic reference electrodes.) Importantly, $\Delta^{\mathrm{w}}_{\mathrm{DCE}}\phi^{0'}_{\mathrm{TEA}^+}$ can be found directly from $\Delta^{\mathrm{w}}_{\mathrm{DCE}}\phi_{\mathrm{eq}}$ using eq 2.1.5. In contrast, no $\Delta^{\mathrm{w}}_{\mathrm{DCE}}\phi_{\mathrm{eq}}$ value can be found from a conventional steady-state IT voltammogram, and $\Delta^{\mathrm{w}}_{\mathrm{DCE}}\phi^{0'}_{\mathrm{TEA}^+}$ has to be determined as an additional fitting parameter; this increases the uncertainties in the extracted k^0 and α values.

Kinetic Analysis of Nanopipette Voltammograms of TEA^+ as a Common Ion. After the a and θ values are evaluated from the limiting currents, the kinetic parameters (k^0 and α) for rapid TEA^+ transfer can be determined from the same quasi-reversible nanopipette voltammogram of TEA^+. Both parameters are obtained by fitting a whole voltammogram to the theory (eq 2.1.6)[43]

$$\frac{i}{i_{\mathrm{ing}}} = \frac{1}{m_{\mathrm{ing}}/m_{\mathrm{eg}} + m_{\mathrm{ing}}/k_{\mathrm{b}} + k_{\mathrm{f}}/k_{\mathrm{b}}}\left(\frac{k_{\mathrm{f}}}{k_{\mathrm{b}}} - \frac{c_{\mathrm{w}}}{c_{\mathrm{DCE}}}\right) \tag{2.1.6}$$

The heterogeneous rate constants, k_{f} and k_{b}, are given by the Butler-Volmer-type model as

$$k_{\mathrm{f}} = k^0 \exp\left[\frac{-\alpha z_{\mathrm{i}} F(\Delta^{\mathrm{w}}_{\mathrm{DCE}}\phi - \Delta^{\mathrm{w}}_{\mathrm{DCE}}\phi^{0'}_{\mathrm{TEA}^+})}{RT}\right] \tag{2.1.7a}$$

and

$$k_{\mathrm{b}} = k^0 \exp\left[\frac{(1-\alpha) z_{\mathrm{i}} F(\Delta^{\mathrm{w}}_{\mathrm{DCE}}\phi - \Delta^{\mathrm{w}}_{\mathrm{DCE}}\phi^{0'}_{\mathrm{TEA}^+})}{RT}\right] \tag{2.1.7b}$$

where $\Delta^{\mathrm{w}}_{\mathrm{DCE}}\phi$ is the Galvani potential difference between the aqueous and DCE phases.

In practice, the precision of kinetic analysis is largely determined by the quality of the experimental voltammogram and particularly by the magnitude of the background current. In previous studies,[8,18] the quality of steady-state voltammograms was improved by background subtraction. In voltammetry of a common ion, the background subtraction is not straightforward because it is difficult to fill the pipette with a blank solution for background measurements and then to refill it with a solution containing the common ion. Without the background subtraction, the aforementioned CV of TEA^+ in both phases of the silanized nanopipette shows significant capacitive current (Figure 2.1.5a). Nevertheless, it fits well the theoretical curve calculated from eq 2.1.6, and the unique combination of the kinetic parameters, $\alpha = 0.67$ and $k^0 = 6.4$ cm/s can be extracted from the best fit. As discussed in ref. 43, the unique fit of the experimental steady-state voltammogram to the theory can be obtained only when both ingress and egress IT waves are quasi-reversible. Different extents of reversibility (i.e., kinetic vs. diffusion control) of the ion ingress and egress processes can be assessed using two dimensionless parameters, $\lambda_{\mathrm{ing}} = k^0/m_{\mathrm{DCE}} = 0.71$ and $\lambda_{\mathrm{eg}} = k^0/m_{\mathrm{w}} = 5.8$.[42] Both λ_{ing} and λ_{eg} are smaller than 10, confirming that both ingress and egress ITs are quasi-reversible.

Similar kinetic parameters were determined with various pipettes at different TEA^+ concentrations (Table 2.1). Higher quality CVs with less interference from background currents allow for more accurate and precise determination of kinetic parameters. The measured charging current was always much higher than expected for nm-sized liquid/liquid interfaces, and its value did not decrease significantly with decreasing *a* (data not shown). These observations suggest that the charging current is mostly due to the stray capacitance of a nanopipette. The background current can be diminished by decreasing the scan rate (e.g., $v = 2$ mV/s in Figure 6b and entries 5 and 6 in Table 1). Also, larger egress current with respect to charging current was obtained at a nanopipette with a larger tip angle ($\theta = 22°$ in Figure 2.1.6c; entry 7 in Table 2.1), where ingress current was also enhanced by employing a higher concentration of TEA^+ in the outer solution.

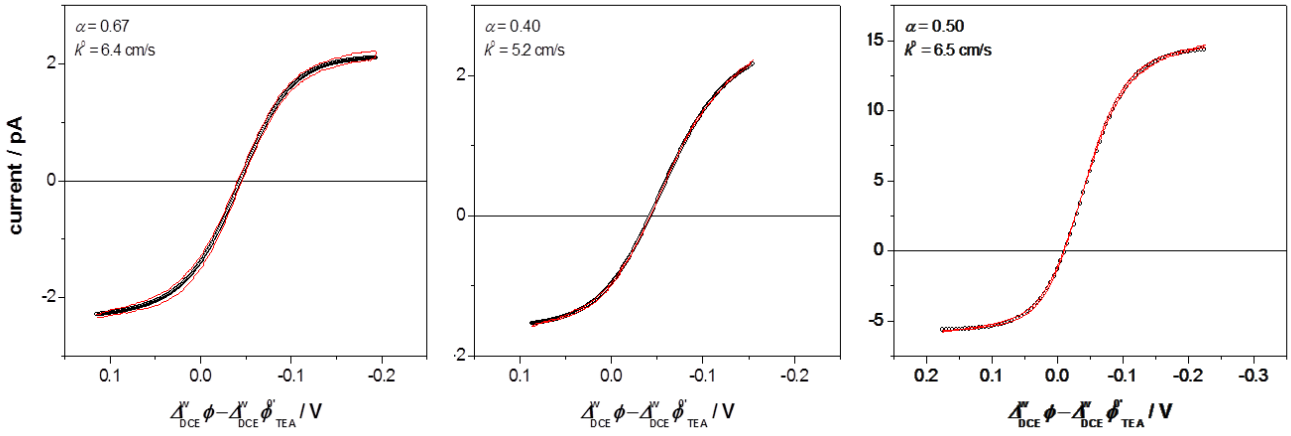

Figure 2.1.5. Steady-state CVs of TEA^+ transfer across the DCE/water interface obtained with nanopipettes in cell 1. The best theoretical fits (closed circles) to the experimental curves (red line) were calculated from eq 6 with parameters in entries (a) 2, (b) 5, and (c) 7 of Table 2.1. Scan rates are 10, 2, and 10 mV/s, respectively.

Table 2.1. Geometric, Transport, and Kinetic Parameters Determined from Nanopipette Voltammograms of TEA^+ at DCE/Water Interfaces.

		geometric parameters			transport parameters		kinetic parameters	
No.	c_{DCE}:c_w	a nm	$f(\theta)$	$\theta°$	m_{DCE} cm/s	m_w cm/s	k^0 cm/s	α
1	0.3:2.7	20	0.16	12	7.1	1.0	6.5	0.44
2	0.3:2.7	16	0.14	10	9.0	1.1	6.4	0.67
3	0.2:2.1	9.7	0.15	11	15	1.9	4.8	0.51
4	0.4:2.1	11	0.15	11	14	1.8	7.6	0.48
5	0.4:2.1	15	0.13	9.5	9.7	1.1	5.2	0.40
6	0.4:2.1	16	0.12	9.0	9.1	0.97	5.4	0.40
7	1.7:2.6	19	0.29	22	7.8	2.1	6.5	0.50
8	0.56:2.6	33	0.23	17	4.5	0.97	6.5	0.50
9	0.21:2.1	215	0.24	17	0.67	0.14	Nernstian	

In Table 2.1, k^0 = 6.1 ± 0.9 cm/s and α = 0.49 ± 0.09 were obtained using seven nanopipettes with different radii. This α value is expected for a simple one-step IT process[28] not complicated by double-layer effects produced either by ITIES or by the negatively charged orifice and wall of a quartz pipette.[43] The independence of kinetic parameters from pipette size indicates that these tips are large enough to avoid significant double-layer effects. The small voltage required to drive the TEA^+ transfer due to its near-zero standard Gibbs energy is another important factor diminishing the interfacial double layer effects.[28]

The kinetic parameters determined here with TEA^+ as a common ion is significantly different from values previously determined from conventional nanopipette voltammograms of TEA^+ only in one phase. In the latter case, analysis of a nearly reversible voltammogram with λ_{ing} (or λ_{eg}) > 1 does not give a unique combination of kinetic and thermodynamic parameters for rapid IT,[43] which is a major source of errors in previously reported k^0 and α values for the TEA^+ transfer.[18] In this way, the underestimated standard rate constants (k^0 ~ 2 cm/s) and overestimated transfer coefficients ($\alpha, \beta > 0.5$) were obtained from CVs of ingress and egress TEA^+ transfer recorded at different nanopipettes.[18] The errors in the β and k^0 values reported for the egress of TEA^+ from water-filled pipettes were somewhat larger because of the neglected effect of ion diffusion in the internal solution.

In a recent paper,[21] the mass transfer coefficient for TEA^+ egress from ultra-small nanopipettes was overestimated: $m_{eg} \geq 100$ cm/s was reported for $a = 1$ nm, while eq. 4b yields $m_{eg} = 12.4$ cm/s for $\theta = 7°$ assumed in ref. 21. For 1.8 nm $\leq a \leq$ 3.2 nm employed in ref. 21, eq. 4b yields 3.9 cm/s $\leq m_{eg} \leq$ 6.9 cm/s. With these m_{eg} values and $k^0 = 110$ cm/s, $k^0/m_{eg} \geq 10$ for all TEA^+ voltammograms analyzed in Table 1 of ref. 21. Therefore, all those voltammograms would be Nernstian if the k^0 value were as high as 110 cm/s. Another likely reason for significant overestimation of k^0 was the lack of pipette silanization, which may result in the true ITIES area much larger than that evaluated from the diffusion limiting current.[39]

2.1.4 Conclusion

A new approach to IT kinetic measurements based on nanopipette voltammetry of a common ion was employed to determine kinetic parameters of the rapid TEA^+ transfer at the DCE/water interface, $k^0 = 6.1 \pm 0.9$ cm/s and $\alpha = 0.49 \pm 0.09$. Both α and k^0 were found to be

essentially independent of the pipette radius. The determined α value agrees with the theoretical predictions, and the k^0 value may be representative for IT reactions with a near zero standard Gibbs energy of transfer.[28] The availability of two current waves in the steady-state voltammogram corresponding to the ingress and egress of the common ion improves the reliability of our kinetic analysis and ensures the unique fit of an experimental voltammogram to the theory.

To carry out successful kinetic experiments at the nano-ITIES, one has to correctly silanize the outer nanopipette wall. The developed new protocol helps to avoid the oversilanization problem that was likely undetected in previous nanopipette studies. High-resolution SEM images showed that proper silanization does not significantly affect *a* and causes only a minor increase in r_g even when the pipette radius is as small as ~20 nm. Carefully silanized nanopipettes with different tip radii are needed for assessment of double layer effects, which are expected to depend on *a*.[43] Silanized nanopipettes can also be employed as SECM probes for high-resolution, chemically selective imaging of topography and ionic conductivity of membranes and various interfaces.[47]

2.2 Kinetics of Ion Transfer at the Ionic Liquid/Water Nanointerface

2.2.1 Introduction

Ion transfer (IT) reactions at the water/ionic liquid (IL) interface are central to a growing number of useful applications of ILs, e.g., in fuel cells, sensors, and solvent extraction.[1-3] Although a number of theoretical and experimental studies of IL electrochemistry have been reported,[4] to our knowledge, the kinetics of IT reactions have not yet been measured. Many fundamental questions in this area remain open including the double layer structure in ionic

liquids and its effects on IT, the applicability of existing IT theory, and the dynamics of the responses of the IL/water interface to the applied voltage.[5-9]

In all previous studies of IT at the interface between two immiscible electrolyte solutions (ITIES) the two liquid phases were water and an organic solvent.[10] The unique structural and physicochemical properties of ILs (e.g., viscosity, conductivity and solvation) offer an opportunity to study dynamics of interfacial IT reactions in a system substantially different from conventional ITIES. Two main obstacles hindering electrochemical studies of ITs at the water/IL interface are the difficulties in obtaining a sufficiently wide polarization window and slow mass transfer in ILs. Our previous electron transfer studies were carried out at a non-polarizable IL/water interface, where the width of a polarization window was not an issue.[7] For IT studies at a polarizable IL/water interface, one needs highly hydrophobic ILS, which became available only a few years ago.[11] Such ILs are typically much more viscous than water or regular organic solvents, thus, giving us a chance to investigate a largely unexplored effect of viscosity on the IT rate at the liquid/liquid interface. For instance, trihexyltetradecylphosphonium bis(1,1,2,2,3,3,4,4,4-nonafluoro-1-butanesulfonyl)imide ($[THTDP^+][C_4C_4N^-]$) employed in our study yielded voltammograms with low background current and good polarization window (>400 mV); however slow diffusion in this viscous IL resulted in very small diffusion currents at nanopipettes and other challenges in determination of fast interfacial IT kinetics.

The heterogeneous kinetics can be measured by an electrochemical method only if the mass-transfer coefficient (m) is not much smaller than the standard rate constant (k^o). Generally, $k^o \geq 10m$ corresponds to essentially diffusion controlled (Nernstian) charge transfer reaction.[12] Rapid IT kinetics were previously studied at water/organic solvent interfaces formed at the tip of a nanometer-sized pipette to ensure sufficiently high rate of mass transfer.[13-18] When an ion is

transferred from the external liquid phase (here, it is IL; Fig. 2.2.1A) to the filling solution inside the pipette (water), the steady-state diffusion limiting current (i_{ing}, i.e., ingress current) and the corresponding mass-transfer coefficient (m_{ing}) are

$$i_{ing} = 4xzFD_{IL}c_{IL}a \tag{2.2.1}$$

and

$$m_{ing} = \frac{4xD_{IL}}{\pi a} \tag{2.2.2}$$

where z, D_{IL} and c_{IL} are the charge of the transferred ion, its diffusion coefficient and bulk concentration in the external solution, respectively; a is the pipette radius, and x is a function of r_g/a (r_g is the outer wall radius; $r_g/a \cong 1.5$; and $x = 1.16$ for typical quartz pipettes).[19]

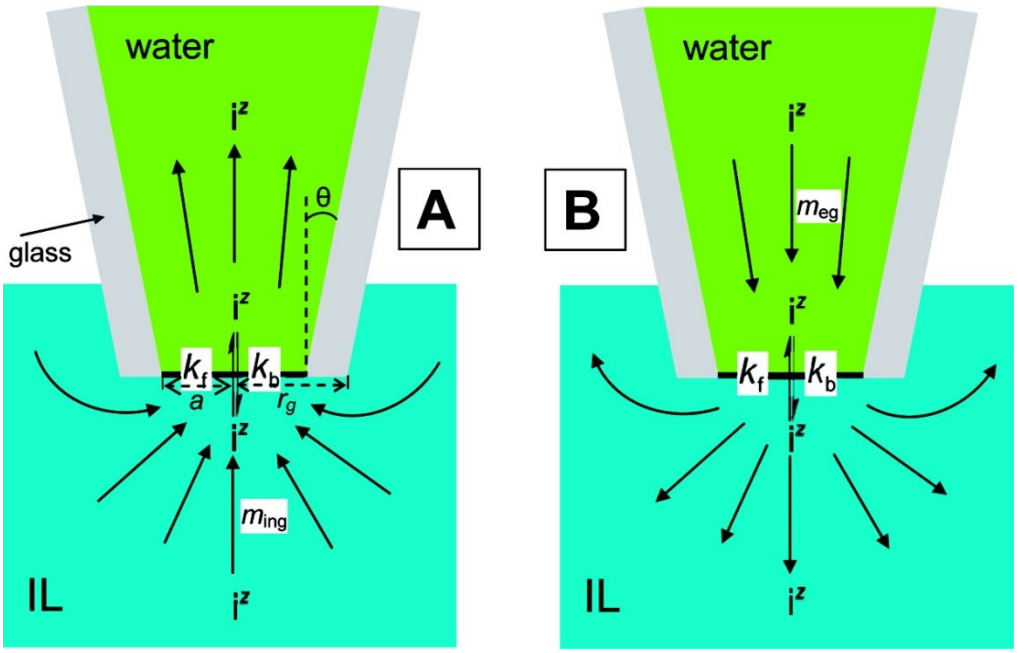

Figure 2.2.1 Scheme of simple IT at a nanopipette-supported ITIES showing the transfer of i^z ion from the external IL solution to the aqueous filling solution (A) and the reverse process (B).

Because of the asymmetry of the diffusion field at a pipette-based ITIES, where the diffusion inside a cylindrical shaft is quasi-linear in contrast to the spherical diffusion of ions to the pipette orifice in the external IL solution, an IT voltammogram at a micrometer-sized ITIES

consists of a steady-state, sigmoidal ingress wave and a time-dependent, peak-shaped wave produced by the reverse reaction (i.e., egress of the same ion to the external solution; Fig. 2.2.1B).[19] The egress IT can reach a steady state if the pipette orifice is sufficiently small (a << 1 μm) and the potential sweep rate is not fast (e.g., a few mV/s).[16,20] Under these conditions, the steady-state diffusion limiting egress current, i_{eg} and the corresponding mass-transfer coefficient (i.e., current) are given by Eqs. (2.2.3) and (2.2.4)[21]

$$i_{eg} = 4f(\theta)z_i F D_w c_w a \tag{2.2.3}$$

$$m_{eg} = \frac{4f(\theta)D_w}{\pi a} \tag{2.2.4}$$

where D_w and c_w are the diffusion coefficient and bulk concentration in the internal aqueous solution, respectively, and $f(\theta)$ is a tabulated function of the tip taper angle, θ.[18,21]

In earlier studies it was assumed that a steady-state response produced by ingress IT is essentially independent of the ion transport inside the pipette.[16,19] However, recent simulations showed that geometry of the pipette inside can significantly affect IT voltammograms.[21-23] Additionally, it was found that an experimental voltammogram of rapid (near-Nernstian) IT obtained with a trasferable ion present only in one liquid phase (i.e., either in the external (Fig. 2.2.1A) or internal (Fig. 2.2.1B) solution) can be fit to the theory using different combinations of kinetic parameters.[24] The unavailability of the unique fit can lead to large uncertainties in kinetic parameters (i.e., k^o and the transfer coefficient, α) extracted from such voltammograms. The accuracy and precision of IT kinetic measurements can be greatly improved by using common ion voltammetry, in which a transferable ion is added to both immiscible liquid phases.[18,24] The advantages of common ion voltammetry stem from the availability of two waves corresponding to the ingress of the common ion into the pipette(Fig. 2.2.1A) and its egress to the external solution (Fig. 2.2.1B). From two limiting currents of a single voltammogram one can assess

asymmetric ion diffusion in the internal and external solutions and evaluate the related geometric and transport parameters using Eqs. (2.2.1) – (2.2.4). Moreover, the unique combination of kinetic parameters can be found by fitting an experimental voltammogram to the theory expressed by Eq. (2.2.5)[24]

$$\frac{i}{i_{ing}} = \frac{1}{m_{\mathrm{ing}} / m_{\mathrm{eg}} + m_{\mathrm{ing}} / k_{\mathrm{b}} + k_{\mathrm{f}} / k_{\mathrm{b}}} \left(\frac{k_{\mathrm{f}}}{k_{\mathrm{b}}} - \frac{c_{\mathrm{w}}}{c_{\mathrm{IL}}} \right) \tag{2.2.5}$$

k_{f} and k_{b} in Eq. (2.2.5) are the heterogeneous rate constants given by the Butler-Volmer-type model

$$k_{\mathrm{f}} = k^0 \exp\left[\frac{-\alpha z_{\mathrm{i}} F (\Delta\phi - \Delta\phi_{\mathrm{i}}^{0'})}{RT} \right] \tag{2.2.6a}$$

$$k_{\mathrm{b}} = k^0 \exp\left[\frac{(1-\alpha) z_{\mathrm{i}} F (\Delta\phi - \Delta\phi_{\mathrm{i}}^{0'})}{RT} \right] \tag{2.2.6b}$$

where $\Delta\phi$ is the Galvani potential difference between two liquid phases and $\Delta\phi_{\mathrm{i}}^{0'}$ is the formal transfer potential of ion *i*. The precision is further enhanced by separate determination of $\Delta\phi_{\mathrm{i}}^{0'}$ from the potential value at zero current, $\Delta\phi_{\mathrm{eq}}$, in a nanopipette voltammogram

$$\Delta\phi_{\mathrm{eq}} = \Delta\phi_{\mathrm{i}}^{0'} + \frac{RT}{z_{\mathrm{i}} F} \ln \frac{c_2}{c_1} \tag{2.2.7}$$

In studies at the water/organic solvent interface, the diffusion coefficents of the trasferable ion in both phases were of the same order of magnitude, and m_{ing} was typically several times larger than m_{eg} because radial diffusion of ions to the tip in the external solution is much less hindered by the pipette wall.[18,21] In contrast, at the water/IL interface, $D_{\mathrm{IL}} << D_{\mathrm{w}}$ and consequently $m_{\mathrm{ing}} << m_{\mathrm{eg}}$. Different extents of reversibility (i.e., kinetic vs. diffusion control) of the ion ingress and egress processes can be assessed using two dimensionless parameters, λ_{ing} =

k^0/m_{ing} and $\lambda_{eg} = k^0/m_{eg}$. Here, we explore this unusual situation and show that common ion voltammetry can be used to investigate the kinetics of such IT processes.

2.2.2 Experimental Section

Chemicals. The following chemicals were used as received: LiCl, $MgSO_4$, 1-methyl-3-octylimidazolium chloride (C_8mimCl) and chlorotrimethylsilane from Aldrich; tetraethylammonium chloride (TEACl) from Sigma; potassium tetrakis(4-chlorophenyl)borate (KTPBCl), tetrabutylammonium chloride (TBACl), tetrahexylammonium chloride (THACl), and tetrabutylammonium perchlorate ($TBAClO_4$) from Fluka. 1, 2-dichloethane (DCE) from Sigma was distilled once. Tetrabutylammonium tetrakis(4-chlorophenyl)borate (TEATPBCl) and tetrahexylammonium tetrakis(4-chlorophenyl)borate (THATPBCl) were prepared by metathesis of KTPBCl with TEACl and THACl, respectively, as described previously.[25] The ionic liquids, trihexyltetradecylphosphonium bis(1,1,2,2,3,3,4,4,4-nonafluoro-1-butanesulfonyl)imide ($[THTDP^+][C_4C_4N^-]$) and 1-methyl-3-octylimidazolium bis(pentafluoroethylesufonyl)imide ($[C_8mim^+][C_2C_2N^-]$) were synthesized by Kakiuchi group from Kyoto University. Tetrabutylammonium bis(1,1,2,2,3,3,4,4,4-nonafluoro-1-butanesulfonyl)imide ($TBA[C_4C_4N^-]$) was prepared by metathesis of HC_4C_4N and TBACl. All aqueous solutions were prepared from deionized water (Milli-Q, Millipore Corp.).

Nanopipette Preparation. The nanopipettes (with radii from 10 to 150 nm) were made from 15-cm-long borosilicate capillaries (outer/inner diameter ratio of 1.0/0.58mm; Sutter Instrument Co., Novato, CA), using a laser-based pipette puller (P-2000G, Sutter Instrument Co.), as described previously.[13,16,18] The pipettes were filled with aqueous solution from the rear, using a small (10 μL) syringe. A reference electrode was inserted into each pipette from the rear.

The outer glass wall of a pipette was silanized in the vapor of chlorotrimethylsilane to render it hydrophobic, which was done by holding the pipette 1-2 cm above the liquid surface of the reagent for ~30 seconds, while the flow of argon was passed through the pipette from the back. The required silanization time depends on the distance between the chlorotrimethylsilane surface and the pipette, its radius, and room temperature.

Voltammetry of TBA^+ or C_8mim^+ as a common ion was used to characterize silanized and non-silanized nanopipettes, as discussed previously.[18] A pair of pipettes with the same radius was pulled from the same borosilicate capillary to compare the responses of silanized and non-silanized nanopipettes.

Instrumentation. A BAS 100B electrochemical workstation (Bioanalytical Systems, West Lafayette, IN) was employed to record the cyclic voltammograms. An Olympus BH2 optical microscope (x100 to x500 magnification) was used to inspect all prepared pipettes before measurements.

Voltammetric Measurements. Voltammetric experiments were carried out at room temperature (23 ± 2 ºC) in a two-electrode U-tube cell. The voltage was applied between two aqueous reference electrodes. Both of them were 0.25-mm-diameter Ag wires coated with either AgCl or Ag_2SO_4, as follows:

Ag| AgCl| 0.1 M LiCl + 0.1 M HC_4C_4N || c_{IL} mM TBA[$C_4C_4N^-$] || 30 mM $MgSO_4$ + c_w mM TBACl |Ag_2SO_4 |Ag
Aqueous reference [$THTDP^+$][$C_4C_4N^-$] Pipette
(Cell 1)

or

Ag| AgCl| 0.1 M LiCl + 0.1 M HC_4C_4N || c_{IL} mM [C_8mim^+][$C_2C_2N^-$] || 0.1 M LiCl + c_w mM C_8mimCl |AgCl |Ag
Aqueous reference [$THTDP^+$][$C_4C_4N^-$] Pipette
(Cell 2)

or

Ag| AgCl| 0.1 M LiCl + 0.1 M HC_4C_4N || c_{IL} mM TBA[$C_4C_4N^-$] || 0.1 M LiCl + c_w mM $TBAClO_4$ |AgCl |Ag
Aqueous reference [$THTDP^+$][$C_4C_4N^-$] Pipette
(Cell 3)

The current produced by the cation transfer from the outer IL phase to the aqueous filling solution was designated as positive.

2.2.3 Results and Discussion

Silanization of Nanopipettes. A water-filled pipette has to be silanized before it is immersed in an organic solution to eliminate a thin aqueous film that otherwise forms on its hydrophilic outer wall making the true area of the liquid/liquid interface much larger than the geometrical area of the pipette orifice.[26] High-resolution SEM showed that silanization results in a formation of a nm-thick film on the pipette wall.[24] Although such a film does not significantly affect the response of a relatively large (e.g., ≥100 nm) pipette, silanization of smaller pipettes must be done cautiously to avoid the formation of a thicker film, which can partially block the pipette orifice and induce solvent penetration into its narrow shaft. A recently developed protocol for silanizing pipettes in the vapor phase allows one to avoid oversilanization of relatively small (e.g., ≥10 nm radius) pipettes.[24] We used the same approach here and found that proper silanization of borosilicate pipettes for measurements in IL can be achieved with a shorter exposure time of ~30 sec. In this way one can further decrease the chances of oversilanizing relatively small pipettes required for kinetic experiments at the IL/water interface.

The effect of silanization was evaluated by comparing the diffusion limiting current recorded at a silanized and non-silanized pipettes pulled from the same glass capillary. Voltammograms obtained in Cell 1 at a silanized (curve 1) and non-silanized (curve 2) pipettes show TBA^+ egress and ingress waves (Figure 2.2.2A). Both waves are sigmoidal, thereby confirming steady-state diffusion of TBA^+ on both sides of the nanoscale interface. The positive limiting current produced by the ingress of TBA^+ at the non-silanized pipette is ~2.5 times larger than that at the silanized nanopipette; this value is in a good agreement with the theoretically

expected ratio of $3.35\pi/(4 \times 1.16) = 2.3$.[16,26] Unlike i_{ing}, the egress current should not be affected by silanization if the orifice radius does not change;[18] this kind of behavior can be seen in Fig. 2A. Similar effects of silanization on the voltammograms of the transfer of a different, asymmetric C_8mim^+ ion at the water/IL nanointerface (Cell 2) can be seen in Fig. 2.2.2B.

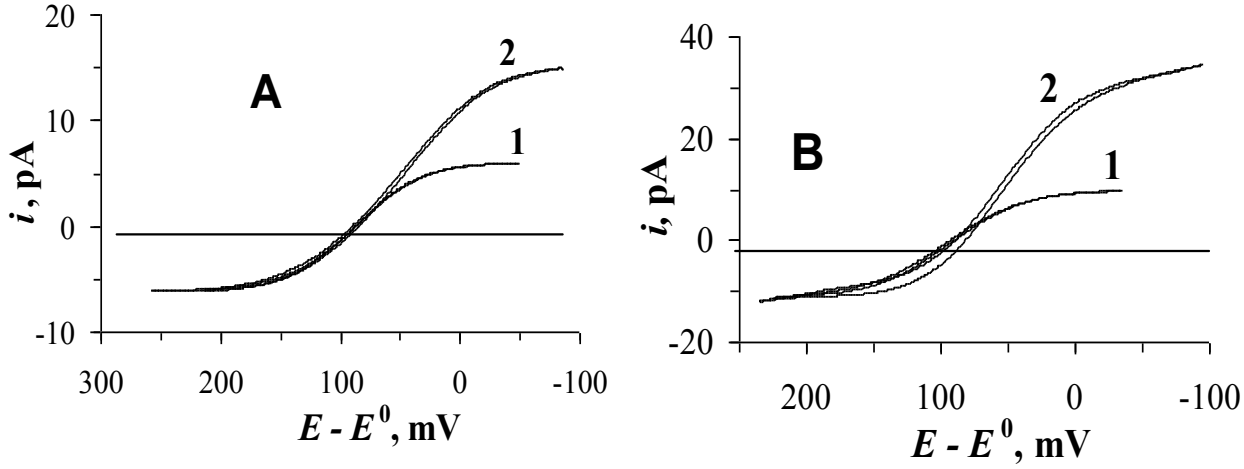

Figure 2.2.2. CVs of TBA^+ (A) and C_8mim^+(B) transfers across the IL/water interfaces obtained with silanized (1) and nonsilanized (2) nanopipettes pulled from the same capillaries. *a*, nm = 82 (A) and 60 (B). The CVs were obtained in cell 1 with c_w = 3.1 mM and c_{IL} = 93 mM (A), and in cell 2 with c_w = 5.0 mM and c_{IL} = 170 mM (B). ν, mV/s = 1 (1) and 10 (2).

To obtain similar i_{eg} and i_{ing} in Fig. 2.2.2, the concentration of the common ion in IL had to be >30 times its value in the filling aqueous solution because of much slower diffusion in IL (see below). Such high concentrations were attainable because of high solubilities of both $TBA[C_4C_4N^-]$ and $[C_8mim^+][C_2C_2N^-]$ in $[THTDP^+][C_4C_4N^-]$; and the contribution of migration to the mass transfer remained negligible because of high ionic concentrations in IL. Another issue related to slow diffusion is the time required to attain a steady-state.[27] Using 1-methyl-3-octylimidazolium-bis(tetrafluoromethylsulfonyl)imide ($C_8mimC_1C_1N$) IL, a steady-state at nanopipette-supported ITIES could be reached on a millisecond timescale.[28] In more viscous $[THTDP^+][C_4C_4N^-]$, the mass transfer is even slower, and retraceable steady-state

voltammograms can be obtained only at a very slow scan rate. For example, voltammograms obtained at the scan rate, ν = 10 mV/s (curves 2 in Fig. 2.2.2) not perfectly retraceable unlike those recorded with ν = 1 mV/s (curves 1 in Fig. 2.2.2). Kinetic measurements at nanopipette-supported ITIES have to be done under steady-state conditions because the detailed picture of the pipette inside geometry required for theoretical treatment of non-steady-state responses is not available.

Diffusion coefficients of ions in IL. The diffusion coefficient of TBA^+ in IL can be determined from the steady-state diffusion limiting current to a nanopipette orifice using Eq. (2.2.1). To minimize the uncertainty associated with the values of x and a for a nanopipette, D_{IL} was determined from the ratio of the diffusion limiting currents measured at the same pipette in IL and in DCE solution. In the latter case, the transferred ion was TEA^+, $z_{DCE} = z_{IL} = 1$, and thus

$$i_{ing,\,IL}/i_{ing,\,DCE} = D_{IL}c_{IL}/D_{DCE}c_{DCE} \qquad (2.2.8)$$

and

$$\frac{D_{IL}}{D_{DCE}} = \frac{i_{ing,IL}}{i_{ing,DCE}}\frac{c_{DCE}}{c_{IL}} \qquad (2.2.9)$$

After measuring $i_{ing,\,IL}$ in Cell 1 with $c_w = 0$ and $c_{IL} = 293$ mM, a silanized pipette was transferred to DCE phase containing $c_{DCE} = 0.4$ mM of TEA^+ to obtain a steady-state voltammogram and determine $i_{ing,\,DCE}$. In this way, the D_{IL}/D_{DCE} ratio was found using several pipettes with different radii (Table 2.2.1). With $D_{DCE,TEA} = 9.8 \times 10^{-6}$ cm^2/s,[16] the data in Table 2.2.1 yields $D_{IL,TBA} = (2.0_3 \pm 0.1_6) \times 10^{-8}$ cm^2/s. This value is ~275 times lower than the coefficient of TBA in water (5.5×10^{-6} cm^2/s[29]).

It was shown recently that diffusivities in IL can be significantly affected by addition of water to it.[30] To eliminate the effect of local changes in water concentration due to its

dissolution at and diffusion from the ITIES into bulk IL, $[THTDP^+][C_4C_4N^-]$ used in our experiments was pre-equilibrated with water. In a similar manner, the diffusion coefficient of C_8mim^+ in IL, was found from the ratio of the i_{ing} values obtained in Cell 2 and Cell 1 with c_w= 0 using differently sized pipettes (from 70 nm to 1 μm radius). The determined value, $D_{IL,C_8mim} = 2.0_5 \times 10^{-8}$ cm^2/s was very similar to that of TBA^+.

Table 2.2.1. Determination of the diffusion coefficient of TBA^+ in IL

a, nm	$D_{IL,TBA}/D_{DCE,TEA}$ x 10^3
190	2.35
140	1.97
60	2.18
30	1.87
25	2.02

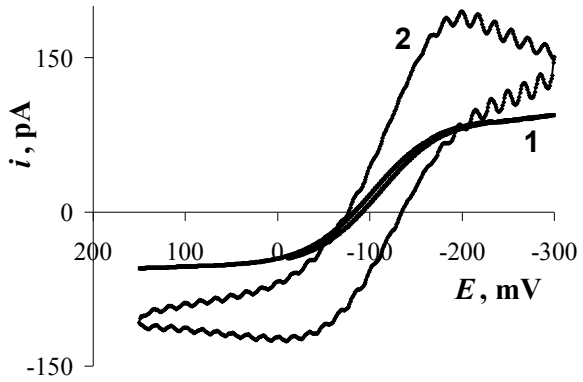

Figure 2.2.3. CVs of TBA^+ ransfer obtained in Cell 1 with different scan rates. ν, mV/s = 1 (1) and 1000 (2). a = 500 nm. c_w = 3.1 mM and c_{IL} = 93 mM.

Much slower diffusivities in IL (as compared to D_w) result in a significantly longer time required for the ingress IT to reach a steady-state. Two CVs in Figure 2.2.3 were obtained at a somewhat larger (500 nm radius) pipette. At ν = 1 mV/s, both egress and ingress ITs is curve 1

attain a steady-state; however, at ν = 1 V/s (curve 2), the egress wave remains essentially sigmoidal, while the ingress wave is peak-shaped. Conversely, conventional voltammograms at micropipettes-supported ITIES exhibit a sigmoidal, steady-state ingress wave and a peak-shaped response due to egress of ions from the pipette.[19-21]

Table 2.2.2. Geometric, Transport, and Kinetic Parameters Determined from Nanopipette Voltammograms of TBA^+ at the IL/Water Interface

concentrations		geometric parameters			transport parameters		kinetic parameters			
No.	c_{IL}:c_w, mM	*a,* nm	$f(\theta)$	$\theta°$	m_{IL}, cm/s	m_w, cm/s	λ_{ing}	λ_{eg}	k^0, cm/s	α
1	93:2.1	140	0.09	6.5	0.002	0.047	48	2.2	0.10	0.57
2	93:3.1	85	0.16	11.5	0.003	0.13	38	1.0	0.13	0.43
3	93:3.1	85	0.10	8.0	0.003	0.08	32	1.4	0.11	0.59
4	93:3.1	69	0.16	11.5	0.004	0.17	19	0.5	0.08	0.52
5	123:4.4	50	0.12	9.0	0.006	0.17	30	1.0	0.18	0.43
6	141:4.6	23	0.09	6.5	0.013	0.28	10	0.5	0.13	0.54
7	93:4.6	21	0.12	9.0	0.014	0.39	6.9	0.2	0.10	0.40

Kinetics of TBA^+ transfer from common ion voltammetry. Kinetic parameters of the TBA^+ transfer (Table 2.2.2) were extracted by fitting common ion voltammograms obtained in Cell 1 to Eq. 2.2.5. Because of a large ratio of diffusion coefficients ($\gamma = D_w/D_{IL}$), the λ_{ing} values in the table are much larger than the corresponding λ_{eg} values; and except for pipette #7, all λ_{ing} values are ≥10. For a water/organic interface, where $\gamma \approx 1$, $\lambda_{ing} \geq 10$ corresponds to an essentially Nernstian IT process whose kinetics is too fast to measure with a given pipette. The use of smaller pipettes to enhance the mass-transfer rate is not an option here because of low diffusion currents in $[THTDP^+][C_4C_4N^-]$. For example, the i_{ing} value obtained for the transfer of 93 mM TBA^+ at a 21-nm pipette (#7 in Table 2) was <2 pA; this is close to the lower limit for i_{ing} at which still one can obtain good quality voltammograms required for kinetic analysis. Moreover, the kinetic parameters obtained with much smaller pipettes may be affected by various

experimental artifacts, strong double layer effects, and deviations from the conventional electrochemical theory.[18,24,31]

Fortunately, at the water/IL interface $\gamma >> 1$, and the reversibility limit is higher. This point is illustrated by Fig. 2.2.4, where the steady-state voltammograms calculated from Eq. 5 for $\lambda_{ing} \geq 10$ and $\gamma = 1$ are essentially reversible (Fig. 2.2.4A); while analogous curves calculated for the IL/water interface (i.e., $\gamma = 275$) are quasi-reversible as long as $\lambda \leq 50$ (Fig. 2.2.4B). Accordingly, all voltammograms summarized in Table 2 are quasi-reversible (Fig. 2.2.4C) except for that obtained at pipette #1 (Fig. 2.2.4D), which is very close to the mass-transfer limit ($\lambda_{ing} = 48$). Unlike conventional IT voltammograms (i.e., those comprised either of an ingress or an egress wave) fitting each common ion voltammogram to the theory yields a single unique combination of k^0 and α.[18,24]

Importantly, there is no correlation between kinetic parameters listed in Table 2.2.2 and the pipette radius that would be indicative of double layer effects and other deviations from conventional theory. The average parameter values are $k^0 = 0.12 \pm 0.02$ cm/s and $\alpha = 0.50 \pm 0.06$. The α value of 0.5 is in agreement with the predictions of IT models either based on a concept of slow diffusion of the transferred species through the mixed interfacial layer[32,33] or assuming the existence of an activation barrier.[34,35] The determined k^0 is markedly lower than the IT rate constants measured at water/organic nanointerfaces.[13-18] For instance, it is ~50 times lower than $k^0 = 6.1$ cm/s reported recently for the transfer of TEA^+ at the water/DCE interface.[18] An obvious difference between these systems is a much higher viscosity of IL, which is likely to result in the higher viscosity of the mixed solvent layer and slower diffusion of the transferable ion through it. According to the slow interfacial diffusion model,[32,33] $k^o = D_i/\Delta x$, where D_i and

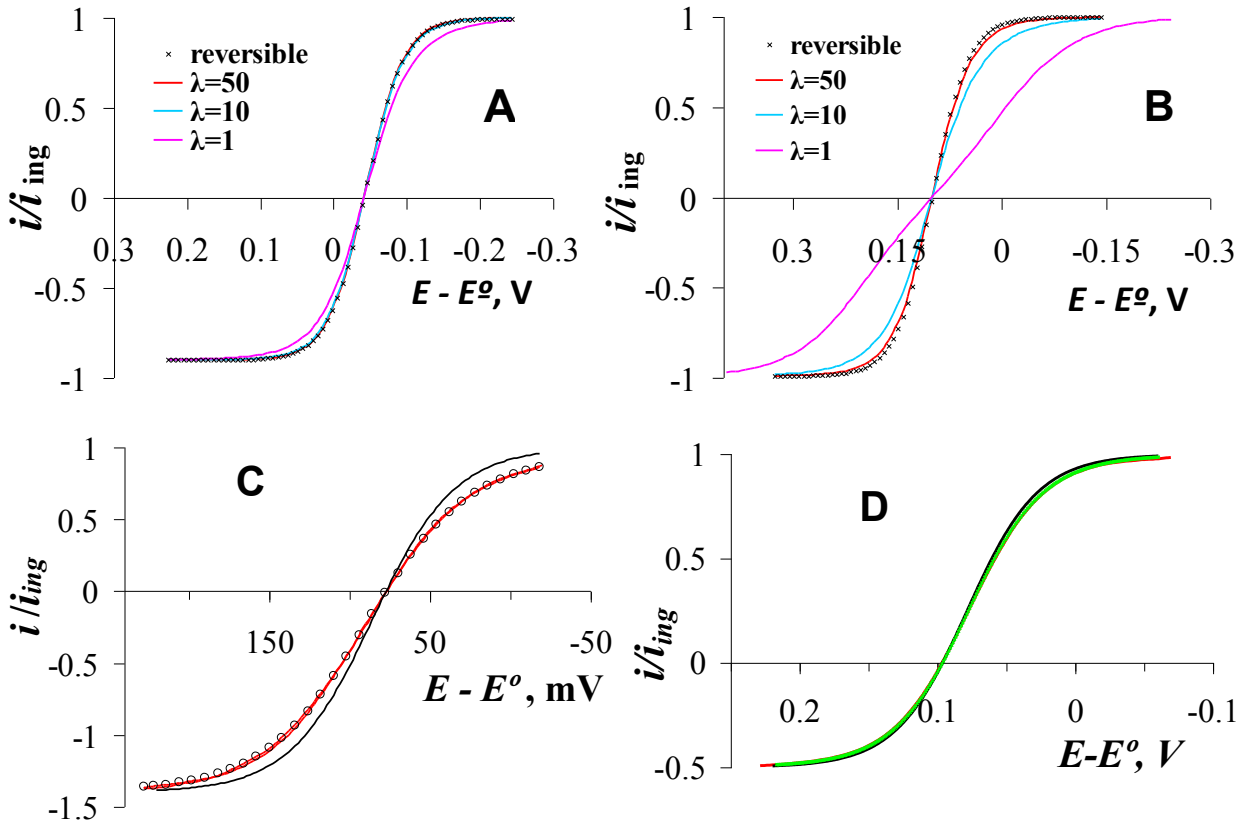

Figure 2.2.4. Kinetic analysis of steady-state common ion CVs of TBA^+ transfer across the IL/water interface. (A) and (B) Reversible (symbols) and quasi-reversible (solid lines) theoretical voltammograms calculated from Eq. 5 for $\gamma = 1$ (A) and 275 (B). $\lambda_{ing} = 1$ (pink), 10 (blue), and 50 (red). $f(\theta) = 0.21$. (C) and (D) Experimental CVs (red curves) fitted to the theory (black circles in C and green circles in D calculated from Eq. 5) with the parameter values listed for pipettes #7 and #1 in Table 2, respectively. Black solid curves represent the theory for reversible IT.

Δx are the diffusion coefficient within the boundary layer and the thickness of that layer, respectively. One can expect D_i (and, consequently, k^o) at the water/IL interface to be significantly lower than at a conventional water/organic interface; however, quantitative comparison is difficult because Δx and other factors may be different in these systems. In contrast, an electron transfer rate constant at the water/IL interface was higher than that measured for the same electron transfer process at the water/DCE interface.[7] One should notice that interfacial electron transfer does not involve crossing of the mixed solvent layer by any ion.

Kinetics of C_8mim^+ transfer at the water/IL interface. Unlike TBA^+, C_8mim^+ is an asymmetric ion, and it is likely to adsorb at the water/IL interface. Because ionic adsorption can affect the IT rate as the ITIES,[36] we measured the kinetics of the C_8mim^+ transfer and compared it to that of TBA^+. Common ion voltammograms of the C_8mim^+ transfer at the water/[$THTDP^+$][$C_4C_4N^-$] interface obtained in Cell 2 (see Fig. 2.2.5) were fitted to Eq. 2.2.5 to obtain kinetic parameter values listed in Table 2.2.3.

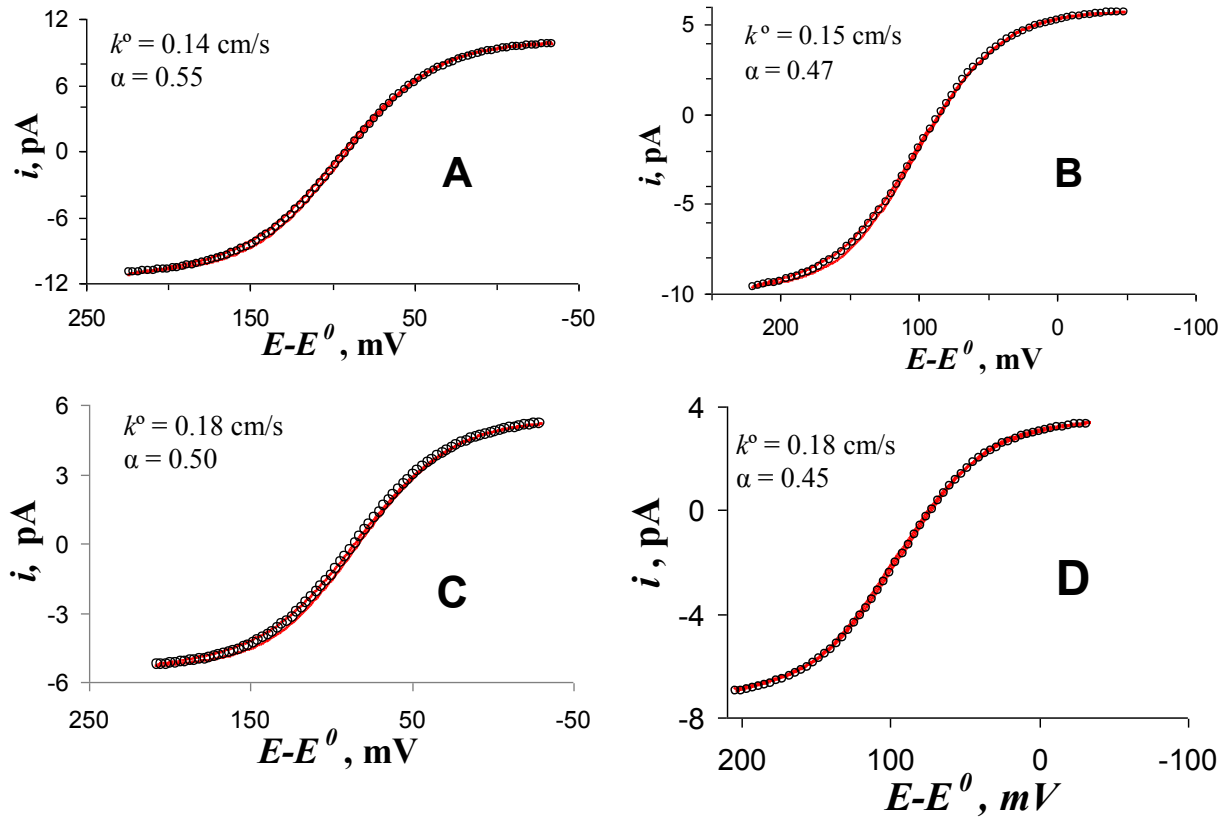

Figure 2.2.5. Steady-state CVs of C_8mim^+ transfer across the nanopipette-supported IL/water interface obtained in cell 2. The best theoretical fit (closed circles) to the experimental curves (red lines) was calculated from Eq. 5 with parameter values listed in Table 3. ν = 1 mV/s.

The mean value of $k^o = 0.16 \pm 0.02$ cm/s is only slightly larger than and $\alpha = 0.49 \pm 0.03$ is not statistically different from that found for TBA^+ transfer. The similarity of the kinetic parameters suggests that asymmetry of C_8mim^+ is not a major factor affecting the IT rate. One

should also notice that the diffusion coefficients of these ions are very similar in both liquid phases.

Table 2.2.3. Geometric, Transport, and Kinetic Parameters Determined from Nanopipette Voltammograms of C_8mim^+ at the IL/Water Interface.

concentrations		geometric parameters			transport parameters		kinetic parameters			
No.	c_{IL}:c_w	a nm	$f(\theta)$	θ^o	m_{IL}, cm/s	m_w cm/s	λ_{IL}	λ_w	k^0 cm/s	α
1	171:5.0	66	0.18	13	0.0045	0.18	31	0.78	0.14	0.55
2	202:7.3	33	0.22	16	0.0090	0.42	17	0.36	0.15	0.47
3	202:7.4	30	0.12	9.0	0.010	0.27	18	0.66	0.18	0.50
4	202:11.6	20	0.15	11	0.015	0.52	12	0.35	0.18	0.45

Effect of ionic charge on mass transfer inside the nanopipette. The rate constants obtained at the nanometer-sized ITIES are consistently higher than those measured for the same IT reactions at larger interfaces.[10] Thus, an important question is whether the IT rates measured at the nano-ITIES, where the diffusion layer thickness is comparable to that of the diffuse double layer, can be altered by double layer effects and other size-related phenomena.[18,24,37] Possible deviations from the conventional electrochemical theory at nano-interfaces, has been discussed in detail for solid nanoelectrodes.[31] Kinetic analysis of nanopipette voltammograms can be further complicated by electrostatic effects produced by the negatively charged inner glass wall.[38] The surface charge can influence ion transport along the wall electrostatically and also affect the IT rate at the edge of the nano-ITIES. Various effects of the surface charge and electrical double layer present at the inner wall including current rectification,[38] accumulation or depletion of ions near the orifice,[39] and electrostatically gated transport[40] have been investigated theoretically and experimentally for nanopipettes and glass nanopore electrodes.

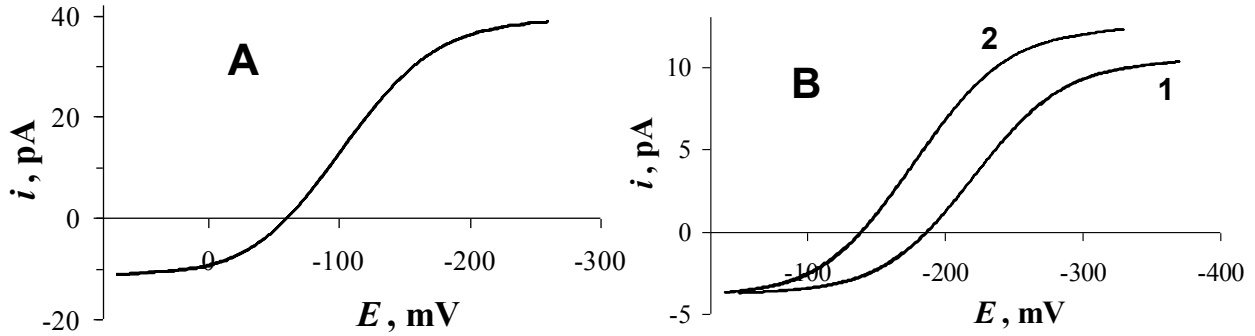

Figure 2.2.6. Steady-state CVs of ClO_4^- and TBA^+ transfers across the water/IL interface obtained in cell 3 with (A) c_w =13 mM, c_{IL}=0; and (B) c_w =10.2 mM, c_{IL}=0 (curve 1) and c_w =10.2 mM, c_{IL}=93 mM (curve 2). ν = 2 mV/s. *a*, nm = 30 (A) and 11 (B).

The absence of correlation between the measured kinetic parameters and the interfacial radius provides evidence against strong double layer effects in our experiments, where the ionic concentration was high in both phases and the pipettes were not very small ($a \geq 20$ nm). To evaluate possible influence of the charged inner wall on ion transport inside the pipette, we compared the ionic currents produced by cationic and anionic species. In Figure 2.2.6A, $TBAClO_4$ was added to the inner aqueous solution, and the IL phase contained no transferable ion (Cell 3). At positive potentials applied to the pipette, TBA^+ was transferred from the filling solution to IL; and at negative potentials, perchlorate was transferred the same way. Therefore, both plateau currents in Fig. 2.2.6A represent i_{eg} of ClO_4^- (positive current) and TBA^+ (negative current). These transfers occur under very similar conditions, i.e., from the same pipette into the same external solution, and with identical bulk concentrations of both ions in the aqueous phase. The differences in their plateau currents can only be attributed to different diffusion coefficients and charges. The ratio of two limiting currents in the absence of electrostatic effects should be equal to $D_{ClO_4^-}/D_{TBA^+}$. With $D_{TBA^+} = 5.5 \times 10^{-6}$ cm^2/s[29] and $D_{ClO_4^-} = 1.8 \times 10^{-5}$ cm^2/s[17], the expected current ratio is $i_{eg,\,ClO_4^-}/i_{eg,\,TBA^+} = 3.3$ regardless of the pipette radius, i.e., pretty close to

the ratio of 3.5 in Fig. 2.2.6A. The values obtained from several other nanopipettes with different radii ranged between 3.0 and 3.6.

For a more complete analysis, after recording a voltammogram of TBA^+ and ClO_4^- transfers (curve 1 in Fig. 2.2.6B), another CV was obtained with the same pipette immersed in IL containing $TBA[C_4C_4N^-]$ (curve 2 in Fig. 2.2.6B). In this case, the positive plateau current was equal to $i_{eg,\ ClO_4^-} + i_{ing,\ TBA^+}$, while the negative plateau current represented $i_{eg,\ TBA^+}$. The difference of positive plateau currents in curves 2 and 1 equals $i_{ing,\ TBA^+}$ = 12.3 pA – 10.3 pA = 2.0 pA. Substituting this value, in Eq. 2.2.1, one finds a = 11 nm. With $i_{eg,\ ClO_4^-}$ = 10.3 pA, Eq. 3 yielded $f(\theta)$ = 0.13; and $i_{eg,\ ClO_4^-}/i_{eg,\ TBA^+}$ = 3.0 was obtained from curve 1. Using nine pipettes with a ranging between 11 nm and 250 nm, the mean value of $i_{ClO_4^-}/i_{TBA^+}$ was found to be 3.4. This finding and the absence of appreciable correlation between the current ratio and a suggest that electrostatic effects do not significantly influence the i_{eg} value. This finding is totally different from the results reported for nanopipettes and glass nanopore electrodes immersed in an aqueous electrolyte solution (i.e., single-phase systems with no liquid/liquid interface).[38-40] One should notice that in IT voltammetry a pA-range current flowing across a nano-ITIES is much lower than that in single-phase experiments. Thus, the potential gradient and the ohmic potential drop inside the pipette are too small for significant electromigration or electroosmotic flow along its charged inner wall.[18,21]

Dynamics of interfacial response. We tried to detect slow relaxation phenomena recently reported at the IL/water interface[9] by investigating the effect of the potential sweep rate on the shape of IT voltammograms (Figure 2.2.7). In ref. 9a, it took >1 min for the interfacial tension and the charging current to reach a steady state after the application of a voltage across the interface between water and trioctylmethylammonium bis(nonafluorobutanesulfonyl)-amide

([$TOMA^+$][$C_4C_4N^-$]) IL; i.e., orders of magnitude longer than the relaxation times observed at the water/organic solvent interfaces. Slow relaxation was attributed to the presence of the layered structure at the surface of IL that has been predicted by molecular dynamics simulations[41] and observed in neutron reflectivity[42] and X-ray reflectivity experiments.[43] The variation of the potential sweep rate between ~1 mV/s and 1 V/s corresponds to the change in the experimental time scale from minutes to <1 s. Such a change should significantly affect the CV shape if the IT response reflects slow interfacial dynamics. The only observable changes in the CV shape in Fig. 2.2.7A caused by the increase in ν from 1 mV/s (green curve) to 2 V/s (brown curve) are a moderately higher charging current (≤10 pA) and more prominent 60 Hz noise due to the decreased filtering (an automatic feature of the BAS potentiostat). The shape of CVs (i.e., the slope, the half-wave potential, and plateau currents after background subtraction) was essentially unaffected by ν, thus showing no effect of slow interfacial relaxation on IT of TBA^+.

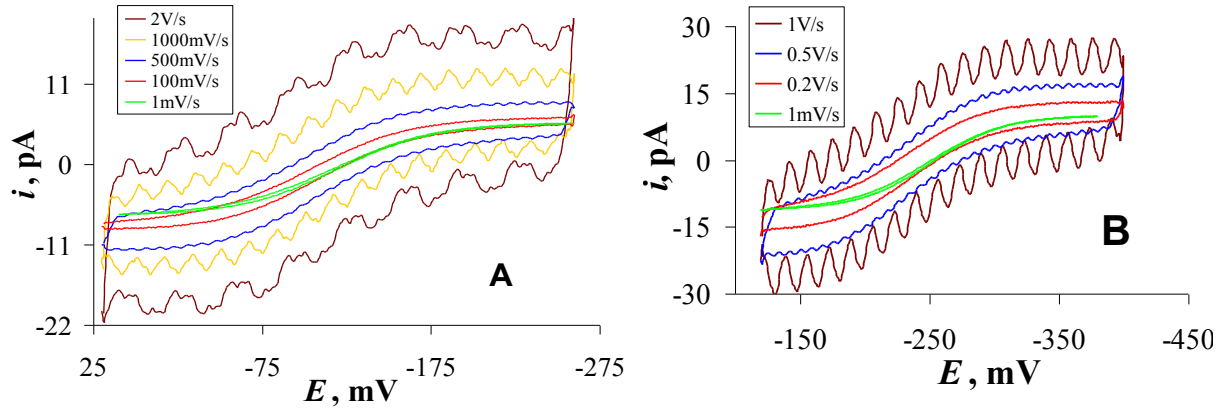

Figure 2.2.7. Effect of the potential sweep rate on CVs of IT at the water/IL interface. (A) Transfer of TBA^+ in Cell 1 with c_w = 3.1 mM and c_{IL} = 93 mM. (B) Transfer of C_8mim^+ in Cell 2 with c_w = 5.0 mM and c_{IL} = 170 mM. ν was varied between 1 mV/s and 2 V/s (A) and between 1 mV/s and 1 V/s (B), as shown in the color legend. a = 60 nm.

This experiment was repeated for IT of asymmetric C_8min^+ ion, which is expected to adsorb at the liquid/liquid interface, and thus it may be a more sensitive probe for slow relaxation phenomena. However, a family of CVs in Fig. 2.2.7B is quite similar to those shown in Fig.

2.2.7A. A CV obtained at ν = 1 V/s shows no shift in the half-wave potential or any other features that could be attributed slow interfacial relaxation. This finding is in agreement with resent results obtained at the interface between water and trioctylmethylammonium bis(nonafluorobutanesulfonyl)-amide IL,[9b] where no slow relaxation features associated with interfacial IT were found in contrast to very slow relaxation of the electrical double layer structure observed at the same interface. This difference can be attributed to fast and slow components of the relaxation dynamics of the electrical double layer on the IL side.[9b]

2.2.4 Conclusions

The use of steady-state common ion voltammetry allowed us to measure IT kinetics at the nanometer-sized water/IL interfaces. These processes are hard to study because of slow mass transfer in the IL phase, which results in a low diffusion current and necessitates the use of small nanopipettes and slow potential sweep rates to attain a steady state. The measured rate constants were more than an order of magnitude lower than those obtained previously for tetraalkylammonium ions at the DCE/water interface. This difference can be attributed to higher viscosity of IL compared that of DCE, which should result in lower diffusivities in the interfacial mixed solvent layer. Very similar IT rate constants determined for TBA^+ and similarly sized but asymmetric C_8mim^+ indicate that ionic adsorption may not be a major rate-determining factor in these systems.

Despite significant differences between ILs and organic solvents, the IT responses at the IL/water interface are not strikingly different from those observed at conventional ITIES. The experimental voltammograms fit very well the theory based on Butler-Volmer model with the transfer coefficient, α very close to 0.5. No unusual features that could be attributed to slow interfacial relaxation have been detected. Similarly, our data does not point to any "non-

classical" effects of the interfacial size on IT kinetics and ion transport. The determined kinetic parameters showed no correlation with the radius of the pipette orifice for $a \geq 20$ nm. The comparison of the diffusion currents produced by the egress of cations and anions from the water-filled nanopipettes ($a \geq 11$ nm) to IL showed that the mass transfer inside the pipette shaft is not significantly affected by migration and other electrostatic effects.

Chapter III

Applications of nanopipettes in SECM

3.1 Nanopipettes in feedback mode of SECM

3.1.1 Introduction

Among several modes of the SECM operation, the feedback mode offers important advantages for topographic and reaction rate imaging.[1] These include high spatial resolution due to the minimal diffusional broadening of the image and high sensitivity to the surface reactivity. Nanopipettes are potentially suitable for the feedback mode imaging. [2a] A pipette can be filled with a solvent immiscible with the outer solution and used as an SECM tip.[2b] The tip current is produced by the transfer of an ion across the liquid/liquid interface [e.g., from water to DCE inside the pipette]. This current is limited by diffusion of the transferable ion in the outer solution. It decreases when the tip is brought close to a solid substrate, which blocks the diffusion to the pipette orifice (negative feedback). The theory developed for the ion-transfer (IT) feedback mode is similar to the conventional SECM feedback theory, and the quantitative agreement between theoretical and experimental current versus distance curves was demonstrated for nanopipette tips.[2c]

Spatial resolution of the SECM and its capacity for investigating small structures and local physicochemical properties are largely determined by the size of the tip and the attainable tip/substrate separation distance.[3] Nanopipettes offer considerable advantages in this area. An extremely small pipette (e.g., ~5 nm[4] or even ~1 nm radius[5]) can be produced instantaneously using a laser pipette puller. Moreover, the thickness of the glass wall is much smaller for pipettes than for metal nanoelectrodes. Typically, the ratio of the outer wall radius (r_g) to the

orifice radius (*a)* is $RG = r_g/a \approx 1.5$; by contrast, the analogous parameter for metal tips is normally ≥5. This should allow one to bring a pipette-based probe extremely close to the substrate surface without touching and potentially damaging the sample. A potential problem here is a roughness of the edge of the pulled glass pipette that can significantly increase the lower limit for the attainable separation distance. So far, only relatively large pipettes ($a > 100$ nm) were employed in quantitative feedback mode SECM experiments at solid substrates.[6]

We have previously developed protocols for polishing nanometer-sized metal electrodes that can greatly facilitate quantitative, reproducible electrochemical experiments.[7] Clearly, surface polishing is not an issue in electrochemistry at the liquid/liquid interface, which is supposed to be smooth and defect-free. However, polishing may reduce the glass roughness, stabilize the IT current, and thus facilitate SECM experiments with extremely small pipette-based probes. The first example of high-resolution topographic imaging based on the negative IT feedback is also presented in this chapter.

3.1.2 Experimental Section

Chemicals. The following chemicals were used as received: LiCl and chlorotrimethylsilane from Aldrich; tetraethylammonium chloride (TEACl) from Sigma; potassium tetrakis(4-chlorophenyl)borate (KTPBCl), tetrabutylammonium chloride (TBACl) from Fluka. DCE from Sigma was distilled once. Tetrabutylammonium tetrakis(4-chlorophenyl)borate (TBATPBCl) was prepared by metathesis of KTPBCl with TBACl, as described previously.[8] All aqueous solutions were prepared from deionized water (Milli-Q, Millipore Corp.).

Nanopipette Preparation. The nanopipettes (with radii from 5 to 100 nm) were made from either 15-cm-long borosilicate capillaries (outer/inner diameter ratio of 1.0/0.58mm; Sutter Instrument Co., Novato, CA) for polishing experiments or 10-cm-long quartz capillaries (outer/inner diameter ratio of 1.0/0.58mm) for imaging IBM wafer, as described previously.[4,6,9]

Polishing was done by using a BV-10 micropipette beveller (Sutter) equipped with a micromanipulator, a long working distance video microscope, and a CCD camera. The micromanipulator was used to move the pipette toward the slowly rotating disk covered with 50 nm lapping tape (Precision Surfaces International, Houston, TX), as described previously for polishing nanoelectrodes.[7] Unlike nanoelectrodes, a pipette should not be polished for more than three minutes to avoid a significant increase in its radius. Because a pipette is more fragile than a metal electrode, its tip can easily be broken. Thus, it must be kept further away from the polishing disk than a nanoelectrode and never touch its surface.

For experiments with the filling DCE solution, the inner wall of the pipette was silanized to prevent penetration of aqueous solution into the pipette. This was done by dipping the pipette tip into chlorotrimethylsilane for ~5-7 s or holding the pipette 1-2 cm above the liquid surface of chlorotrimethylsilane for ~1 minute. In the latter case, the required silanization time depends on the distance between the chlorotrimethylsilane surface and the pipette, its radius, and room temperature, as described before.[9] This was crucial because the external aqueous solution gets drawn inside a pipette if its inner surface is hydrophilic. Before imaging, the pipette radius was evaluated by steady-state voltammetry and the stability of its response was checked by immersing it into a 0.6 mM aqueous solution of TEACl and passing the diffusion-limiting current of TEA^+ transfer. The pipette was deemed suitable for imaging if the current changed by <3% during 20 min.

SEM imaging. A Zeiss Supra 55 VP field-emission SEM was employed to visualize the tips of polished and unpolished nanopipettes. An ~3 nm-thick Au-Pd layer was coated on the otherwise insulating nanotip to be imaged without significant charging. An ~1 cm-long tip was cut from the nanopipette and coated with Au by sputtering while the tapered end was directed vertically toward the target. All images were obtained with an Inlens detector.

SECM Setup. SECM experiments were carried out using a home-built instrument, which was similar to those described previously.[7b] A PI-841 piezoactuator (Physik Instrumente) used for *z*-axis scanning was controlled by a E-500 position controller (Physik Instrumente), which provided the 0.1-nm resolution in a closed-loop mode. All experiments were carried out at room temperature (23±2°C) in a two-electrode cell:

$$\text{Ag/AgTPBCl/ 10 mM TBATPBCl//}c_{\text{w}}\text{ TEACl + 0.2 M LiCl/AgCl/Ag} \qquad \text{(Cell 1)}$$

inner DCE solution outer aqueous solution

The substrate in negative feedback experiments was a clean silanized glass slide. The procedure used for obtaining approach curves with nanopipette tips was essentially the same as described previously for nanoelectrodes tips.[7] Electronic microcircuits (wafers and microchips) were obtained as a gift from Ms. Mary Westermann (IBM Corporation, East Fishkill, NY). A portion of the wafer that contained the area of interest was carefully cut using a glass cutter and glued to a glass microscope slide.

3.1.3 Results and Discussion

SEM of Unpolished and Polished Nanopipettes. To evaluate the effect of polishing on nanopipette geometry, we obtained SEM images of pairs of nanopipettes pulled from the same capillary. Figure 3.1.1 shows images of a pair of ~75 nm pipettes, one of which polished (A) and another one unpolished (B).

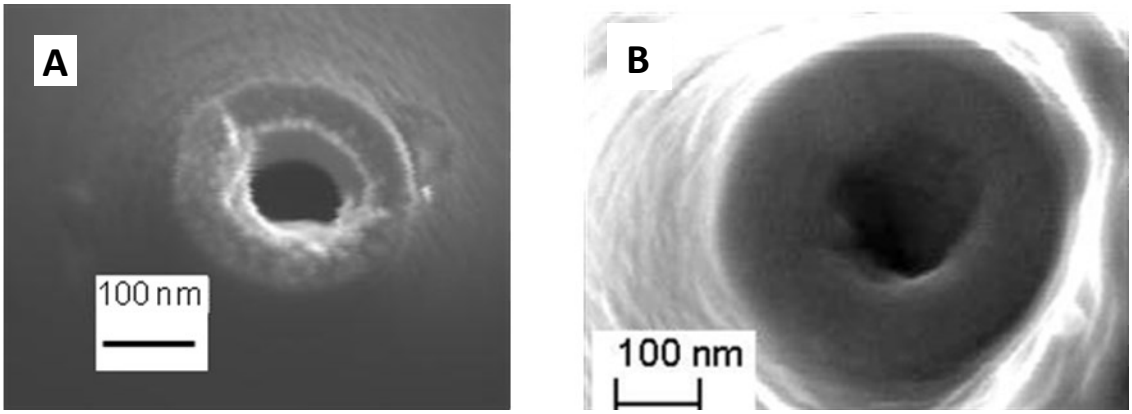

Figure 3.1.1. SEM images of (A) unpolished and (B) polished nanopipettes.

From the top view SEM image of an unpolished nanopipette (Fig. 3.1.1A) one can determine $a \approx 75$ nm and $RG \approx 1.6$, , which is typical for pipettes pulled from capillaries of this type. Considerable roughness of the glass the surface that can be seen clearly in Fig. 3.1.1A is greatly diminished by polishing (Fig. 3.1.1B). Importantly, the pipette radius remained essentially unchanged after polishing, while the *RG* increased to ~2. A significant increase in pipette radius observed in some other experiments points to excessive polishing.

Voltammetry and SECM. If the pipette polishing does not increase the pipette radius, the diffusion limiting currents obtained with unpolished and polished pipettes should be similar. Steady-state voltammograms of this kind (not shown) can be obtained for relatively large pipettes like those in Fig. 3.1.1. For much smaller pipettes (e.g., $a \leq 10$ nm), the length of glass removed by polishing is significant, and therefore *a* is often increased by polishing. The increase in *a* results in a somewhat higher diffusion limiting current after polishing, as illustrated by two steady-state voltammograms of TEA^+ transfer from water to DCE obtained in Cell 1 at an unpolished (1) and polished (2) pipettes (Fig.3.1.2). While the effective radius increased after polishing from 4.0 nm to 6.6 nm, the shape and position of the ion transfer voltammogram have not been significantly affected by polishing.

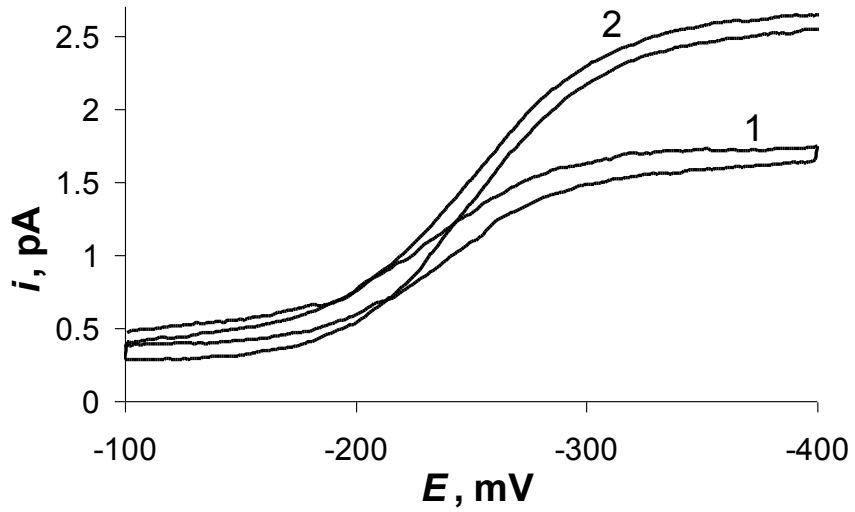

Figure 3.1.2. Voltammograms of TEA^+ transfer obtained in Cell 1 with unpolished (1) and polished (2) nanopipettes pulled from the same glass capillary. c_w = 1 mM. External aqueous solution contained 0.1 M LiCl. Potential sweep rate was 10 mV/s.

To record a good quality approach curve with a pipette tip, the diffusion limiting current in the bulk solution ($i_{T,\infty}$) must be stable on the time scale of minutes, the liquid interface must be flat and stationary, and the glass wall sufficiently smooth for attaining the closest separation distance, $L << 1$. Relatively small unpolished pipettes (e.g., $a < 50$ nm) often do not meet all these requirements; hence a low success rate in imaging and obtaining approach curves. A typical example is shown in Fig. 3.1.3, where approach curve A was obtained with an ~20 nm unpolished pipette tip. As the tip approached the glass substrate, the diffusion of TEA^+ to the pipette orifice was blocked, and the negative feedback was observed. The rough glass wall started to push against the substrate surface at the normalized current, $I_T = i(d)/i_{T,\infty} \approx 0.4$, which corresponds to the separation distance or the order of one pipette radius (the exact coordinate of the substrate surface and therefore absolute d values could not be determined in this case). After this point, the current began to level off instead of approaching zero in accordance to the theory for negative feedback. An approach curve obtained with a polished pipette from the same pair

(curve B in Fig. 3.1.3) does not show this problem. The tip/substrate separation distance of <2 nm was attained with no sign of contact between the pipette and wall and the substrate.

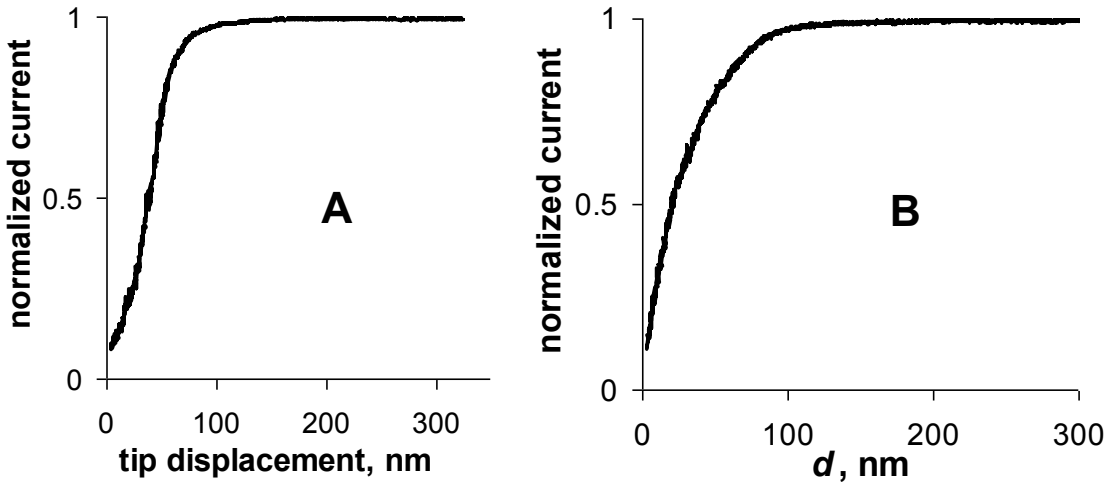

Figure 3.1.3. SECM approach curves obtained with unpolished (A) and polished (B) ~20 nm radius nanopipettes approaching a glass substrate in Cell 1. c_w = 2.5 mM. The current for each pipette was normalized by the corresponding $i_{T,\infty}$ value.

Using polished nanopipettes, it was possible to obtain and quantitatively analyze approach curves with a radius under 10 nm (Figure 3.1.4). With c_w = 0.82 mM, the radius (a) calculated from limiting current of TEA^+ transfer was 8.3 nm. The experimental data (symbols) was fitted to the theoretical equation (1), which is valid for any $RG < 200$[10]

$$I_T = \frac{\frac{2.08}{RG^{0.358}}\left(L - \frac{0.145}{RG}\right) + 1.585}{\frac{2.08}{RG^{0.358}}\left(L + 0.0023RG\right) + 1.57 + \frac{ln\,RG}{L} + \frac{2}{\pi RG} ln\left(1 + \frac{\pi RG}{2L}\right)} \qquad (3.1.1)$$

where I_T is the tip current normalized by the $i_{T,\infty}$ value. The negative feedback approach curve in Figure 3.1.4 (symbols) fits the theoretical curve (black solid line) calculated with RG =1.9 and a = 8.1 nm, which is very close (within ~2%) to the radius calculated from limiting current. Other theoretical curves in Fig. 3.1.4 were calculated for RG = 1.1 (curve 1), 2.5 (curve 3) and 10

(curve 4). Despite very small pipette dimensions, the data quality is sufficiently high to specify the *RG* within a narrow range, i.e., 1.9 ± 0.3. The distance of the closest approach in Fig. 3.1.4 is as small as $L = 0.1$; i.e., $d \approx 0.8$ nm. Such a separation distance could be achieved only with the essentially flat glass surface. Such a short separation distance would be almost impossible to attain with a metal tip whose *RG* is typically much larger than that for a pipette. While electron tunneling between a metal tip and a substrate occurring at separation distances of the order of 1 nm can preclude ultra-high resolution electrochemical imaging of conductive surfaces,[11] the nanopipette-based probes are not affected by this problem.

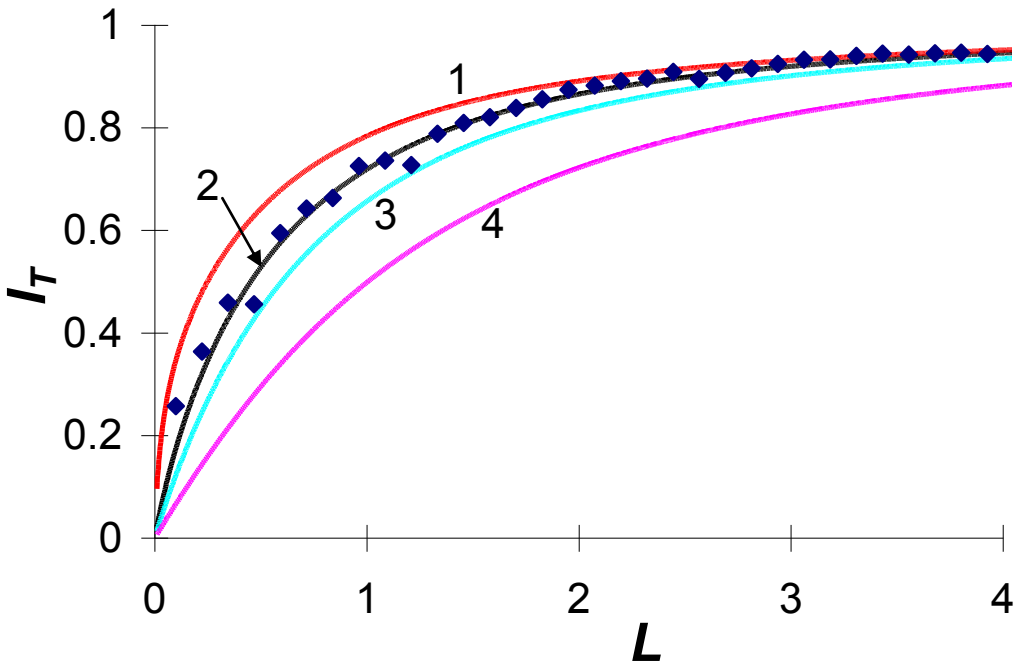

Figure 3.1.4. Experimental (symbols) and theoretical (solid lines) scanning current-distance curves for TEA^+ transfer from water to DCE at the 8 nm pipette approaching a solid substrate. Theoretical curves were calculated for $a = 8.1$ nm, and $RG = 1.1$ (1), 1.9 (2), 2.5 (3), and 10 (4) from Eq. (3.1.1).[10] The approach velocity was 5 nm/s.

Imaging with Nanopipette Tips

Figure 3.1.5 shows a 1.8 μm × 1.8 μm constant-height image of the etched wafer region. This image was obtained using a nanopipette probe filled with DCE solution containing

TBATPBCl electrolyte. The tip current was produced by the transfer of TEA^+ from the external aqueous solution to DCE. The tip potential was held at −400 mV versus aqueous Ag/AgCl reference, at which the TEA^+ transfer occurred at a diffusion-controlled rate. The pipette radius (a = 106 nm) was determined from the steady-state voltammogram assuming RG = 1.5.[2b,2c] The surface pattern in 3.1.5B is in agreement with the optical micrograph 3.1.5A. An advantage of a sharp nanopipette probe over a conventional SECM tip is in very small RG, which makes it easier to image nonflat surface features without crashing the tip. However, the magnitude of the negative IT feedback (i.e., the decrease in the tip current at the given value of the normalized separation distance, d/a) is lower for a pipette than for a conventional probe with a larger RG because of the TEA^+ diffusion from the back of the tip.[2b] Therefore, a pipette has to be brought closer to the substrate surface to attain the same magnitude of the negative feedback.

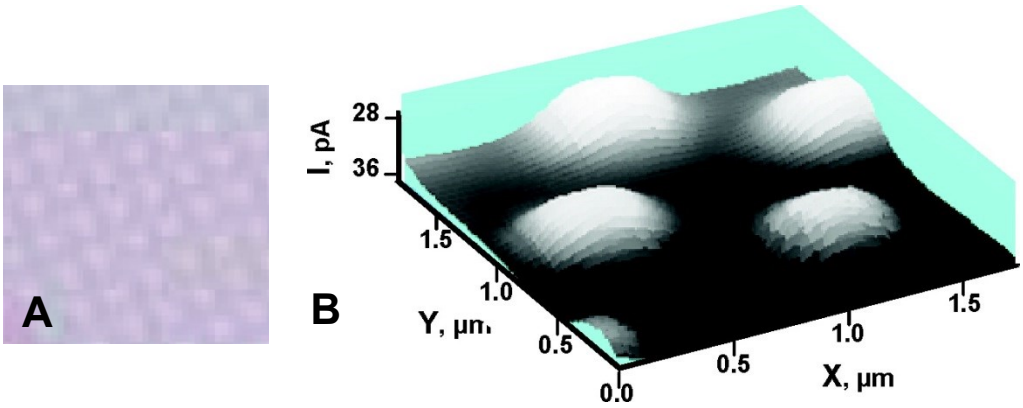

Figure 3.1.5. (A) Optical image of an IBM wafer and (B) Constant-height IT SECM image of the 1.8 µm × 1.8 µm portion of an IBM wafer obtained with a 106 nm radius pipette-based tip in aqueous solution containing 0.6 mM TEACl and 10 mM LiCl. The filling DCE solution contained 10 mM TBATPBCl. ν = 200 nm/s.

It is interesting to compare ion-transfer-based SECM imaging to a somewhat related technique—scanning ion conductance microscopy (SICM)—in which a nanopipette is used as a scanning conductivity probe.[12] In SICM, a significantly higher tip current and the absence of the liquid/liquid interface result in a more robust imaging procedure and slightly higher lateral

resolution (~10−20 nm). The advantage of the IT-based SECM is in its chemical specificity. Since the tip current is produced by the transfer of one specific ion (e.g., TEA^+), SECM can be used for studying IT reactions,[2c] e.g., ion transfers across biological and artificial membranes. Interfacial IT rates can be mapped in addition to topographic imaging discussed in this paper.

3.1.4 Conclusion

The procedures developed previously for glass-sealed metal electrodes have been adapted to the polishing of open nanopipettes. Voltammograms, SEM images and SECM approach curves show that pipettes with a radius as small as <10 nm can be polished without breaking the tip or plugging the orifice with polishing material. A smoother glass surface and a more stable diffusion current produced by polishing made possible quantitative SECM experiments with very small pipette probes and at separation distances of ~1 nm. The possibilities of high resolution SECM imaging and kinetic experiments with polished pipette probes are currently being explored in our laboratory.

3.2 Electron Transfer/Ion Transfer Mode of Scanning Electrochemical Microscopy (SECM): a New Tool for Imaging and Kinetic Studies

3.2.1 Introduction

During the last two decades, scanning electrochemical microscopy (SECM) has evolved as a powerful tool for studying heterogeneous and homogeneous reactions in chemical and biological systems and for high-resolution chemical imaging.[1] The capacity for inducing and monitoring local changes in chemical composition, rates, potentials and conductivity on the nanoscale or submicrometer-scale and the availability of quantitative theory gave SECM a niche

in nanoscience,[2] alternative energy research,[3] and bioelectrochemistry.[4] At the same time, some significant limitations of SECM have become apparent that need to be overcome lest they impede further progress in the field. These include the difficulties in separating the contributions of surface topography and reactivity to the tip current[5] and the detection and analysis of the low-level signals produced by biological specimen and small surface features (e.g., individual catalytic nanoclusters). Both issues are most pronounced in experiments employing nanometer-sized SECM probes.[6]

Several strategies have been developed for micrometer-sized tips to separate the topography and reactivity effects, including various versions of tip position modulation,[7] shear-force based control,[8] AC-SECM,[9] current-independent method based on attenuated total reflection infrared spectroscopy,[10] and intermittent contact SECM.[11] The extension of these methodologies to nanometer scale experiments is not straightforward. Another approach is to employ a dual-probe tip, in which one electrode (or pipette orifice) serves as a distance sensor and another one is used for electrochemical measurements.[12] Different dual-probes geometries have been produced: two channels of a pulled θ-capillary were used a dual-disk probe[12,13] and concentric ring-disk-type tips were prepared by applying a conducting coating to the outer wall of a pulled glass pipette.[14] Despite inherent problems (i.e., a larger size as compared to a single-probe tip, the possibility of a cross-talk, and the discrepancies between two sensors addressing different spots on the substrate surface), smaller dual probes have been used for submicrometer-scale imaging with independent distance control.[13,14] The voltage-switching mode of the SECM operation,[5] requiring two redox mediators (for distance control and electrochemical measurements), is perhaps the best technique for simultaneous topographic and electrochemical imaging reported to date. A new approach introduced in this article enables topography-

independent reaction rate imaging on the nanoscale using a simple open-pipette probe and with no redox mediator present in the bulk solution (this is an advantage in experiments with biological cells and other redox-sensitive specimen[15]).

The difficulties in probing low signal sources (e.g., biological cells or small metal clusters) on the nanoscale stem from fundamental limitations of the SECM feedback and substrate generation/tip collection modes. In a feedback-mode experiment, the tip (either a metal microelectrode or an open pipette containing a liquid phase that is immiscible with the outer solution) is brought to within a few tip radii of the substrate surface. The electrolyte contains one form of electroactive mediator (e.g., reduced) and the tip potential is such that the mediator consumption (e.g., oxidation) occurs at a rate governed by diffusion. If the mediator is regenerated (reduced) at the substrate, the tip current increases at shorter tip-to-sample distances (positive feedback; Figure 3.2.1A). If no mediator regeneration occurs at the sample, the tip current decreases with decreasing d because of hindered diffusion of redox species (negative feedback). The feedback mode allows one to attain fast mass-transfer rate and high spatial resolution. However, it is not suitable for probing low signal sources that produce positive feedback much lower that the magnitude of the tip current in the bulk solution ($i_{T,\infty}$). It was shown that a conductive feature on the insulating planar substrate can only be detected in the feedback mode if its radius is $\geq 0.1a$, where a is the tip radius.[16] Similarly, a kinetically slow mediator regeneration at the substrate may not produce measurable feedback current. This issue is especially important when a nm-size tip is employed because of very high current density at its surface.[6] The substrate generation/tip collection (SG/TC) mode is an alternative to the feedback mode for imaging small surface features and measuring slow kinetics. Because the reactant is generated at the substrate and collected at the tip, the very low $i_{T,\infty}$ in SG/TC mode results in

much higher sensitivity. However, the significant diffusion broadening effect (i.e., the apparent size of an object in the SECM image is larger than its actual dimensions)[17] and elevated background signal due to the continuous generation of the reactant at the substrate[18] limit the applicability of this mode to imaging and quantitative kinetic measurements.

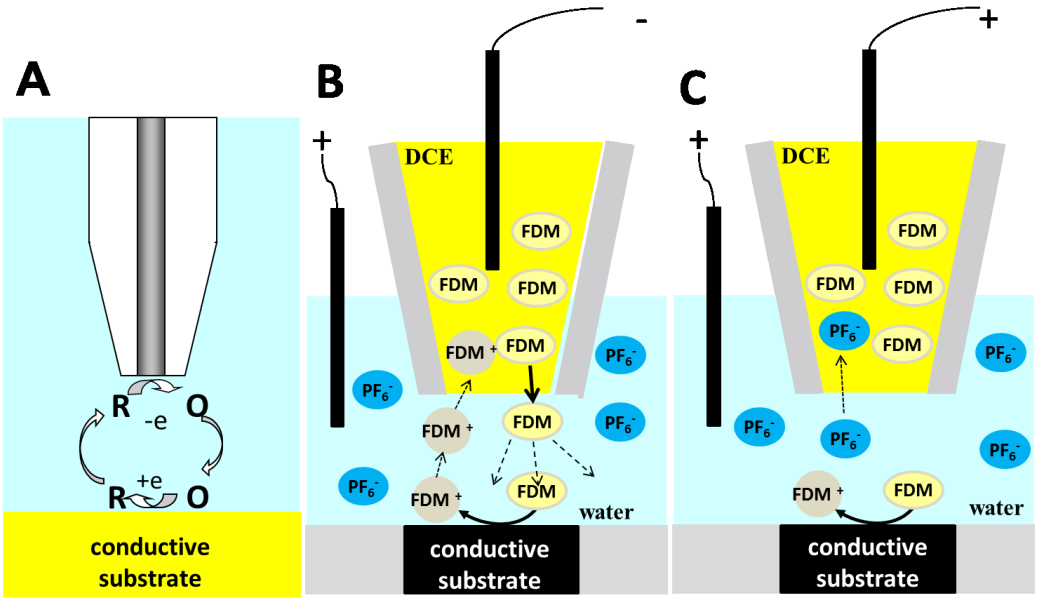

Figure.3.2.1 Schematic representation of conventional feedback mode of the SECM operation (A) and ET/IT mode with positive (B) and negative (C) IT feedback.

Here we introduce a new mode of the SECM operation—electron transfer/ion transfer (ET/IT) mode—which can combine the advantages of the feedback and SG/TC experiments without being plagued by their shortcomings. In an ET/IT experiment, the tip is a nanometer-sized pipette filled with a liquid phase (e.g., DCE) immiscible with the external solution (e.g., aqueous). A neutral redox species (e.g., ferrocenedimethanol; FDM) is initially present only in DCE solution inside the pipette; during the experiment this species partitions from organic to the aqueous phase. When the pipette tip is brought to within a few tip radii of a conductive substrate, FDM can diffuse to its surface and be oxidized or reduced there (Fig. 3.2.1B). The

recorded oxidation current represents the local ET rate at the microscopic portion of the substrate surface facing the tip. In this way, micropipettes have previously been used for reagent delivery[19] and for studying electrocatalytic reactions.[20] In a somewhat similar setup, both inner and outer solutions were aqueous, and a redox mediator diffused out of the pipette, while a Au ring electrode formed around the pipette orifice was used for feedback mode measurements.[21] Reagent delivery from either single[22a,b] or dual[22c,d] nanopipettes has also been employed for surface patterning either in solution[22a,b,d] or in air.[22c] In the conceptually similar scanning micropipette contact method (SMCM), a liquid meniscus is formed between the pipette tip and the sample surface to probe the localized electrochemical activity of heterogeneous substrate surface.[23]

Unlike the experiments reported in refs. 19-23, the product of the substrate reaction (FDM^+) can be transferred into the filling DCE solution by applying negative potential to the electrode inside the pipette, thus producing an IT tip current (Fig. 3.2.1B). This current must increase with the decreasing tip/substrate separation (d) similarly to the conventional feedback (Fig. 3.2.1A). We will call this effect positive IT feedback. Similarly to conventional feedback mode, the FDM^+ diffusion is localized within the narrow tip/substrate gap, providing high spatial resolution; however, with $i_{T,\infty} = 0$, the sensitivity of the ET/IT mode is similar to that of the SG/TC experiments (see below).

In the ET/IT mode with negative IT feedback (Fig. 3.2.1C), the pipette is biased to a positive potential, which prevents the transfer of FDM^+ and instead drives the transfer of anions (e.g., PF_6^-) from the external solution to DCE. The latter process produces negative feedback, i.e., the IT current at the pipette orifice decreases with decreasing d, as discussed previously.[24] The negative feedback response is independent of the surface reactivity and can be used for the

pipette positioning and distance control. The partitioning of neutral FDM species (and, thus, its oxidation at the substrate) is not affected by the change in the tip potential.

3.2.2Theory and Simulations

The diffusion-controlled negative IT feedback current (e.g., the transfer of PF_6^- in Fig. 3.2.1C) is independent of the tip and substrate processes involving the redox mediator (FDM/FDM^+ couple). The previously developed SECM theory for pure negative feedback taking into account small thickness of the pipette wall[24a,25]can be used to calculate current-distance ($i_T/i_{T,\infty}$ vs. d/a) curves for this process.

Partitioning and diffusion flux of neutral species from the pipette. The steady-state diffusion problem for the ET/IT feedback (Fig. 3.2.1B) involving the partitioning of neutral redox species from the pipette to the external solution, diffusion of this species to and their oxidation (or reduction) at the conductive substrate, diffusion of the reaction product to the pipette orifice, and IT at interface between two immiscible electrolyte solutions (ITIES) is formulated in Appendix. Neutral species (e.g., FDM) partitioning across the liquid/liquid interface do not contribute to the tip current, and the diffusion flux of this species independent of the tip potential is:[26]

$$j_{max} = 4f(\theta)Dc^*a \qquad (3.2.1a)$$

To facilitate the discussion of the interplay between the partitioning and diffusion process and the collection efficiency in ET/IT experiments, we will express this flux the units of current

$$i_{max} = j_{max}F = 4f(\theta)FDc^*a \qquad (3.2.1b)$$

where $f(\theta)$ is a factor related to the pipette angle θ (Fig. 3.2.2),[26a] F is the Faraday constant, c^* is the concentration and D is the diffusion coefficient of FDM in DCE, and a is the pipette radius.

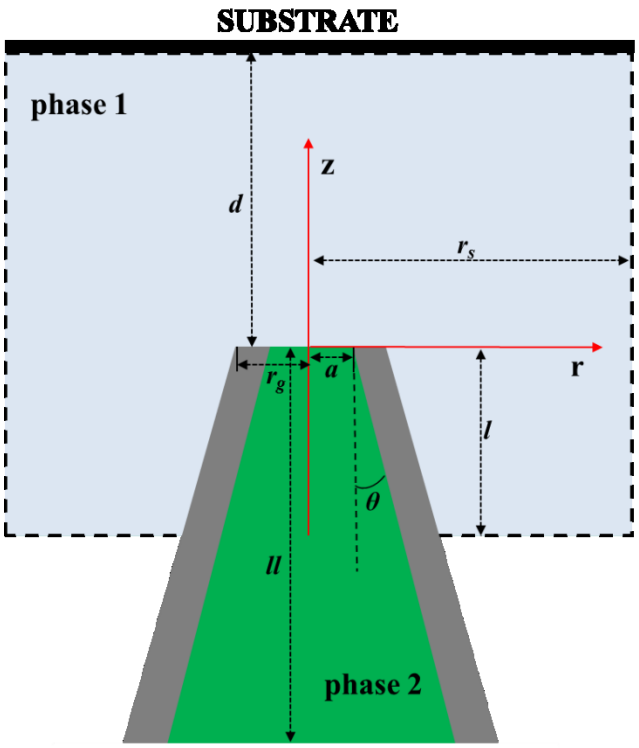

Figure. 3.2.2 Geometry of the simulation space and parameters defining the diffusion problem for the ET/IT mode of the SECM operation with a nanopipette tip.

The diffusion limiting flux (or the maximum diffusion current) in Eq. (3.2.1) corresponds to the infinitely small partition coefficient (K) of the neutral redox species between the external liquid phase and the filling solution (i.e., between water and DCE). In general, the outward flux of neutral species from the pipette depends on K. Fig. 3.2.3 shows this dependence as a family of dimensionless curves ($i_{p,\infty}/i_{max}$ vs. K, where $i_{p,\infty}$ is the partitioning current) simulated for different values of tanθ. The set of θ values in Fig. 3 from ~2.9° (red curve) to ~17° (yellow curve) covers the practically achievable range of quartz pipette angles.[26] The entire family of working curves was fit to the following analytical approximation:

$$\frac{i_{p,\infty}}{i_{max}} = \frac{1}{1 + K\dfrac{tan\theta}{0.1814tan\theta + 1}} \qquad (3.2.2)$$

The maximum relative error of the fit is 1.7% for K ranging from 10^{-4} to 10^{4}.

K = 1 represents a practically interesting case of single-phase diffusion with the same solvent present inside and outside the pipette. Such a system has previously been used for reagent delivery to catalytic surfaces.[21] This model also describes the diffusion of nanoparticles from the pipette into the outer solution with no external voltage applied as long as the particle diameter is much smaller than that of the pipette. Below we present simulations of current-distance curves for two partition coefficient values, K = 2 for relatively hydrophilic FDM, and K = 150 for more hydrophobic ferrocenemethanol (FM).[20]

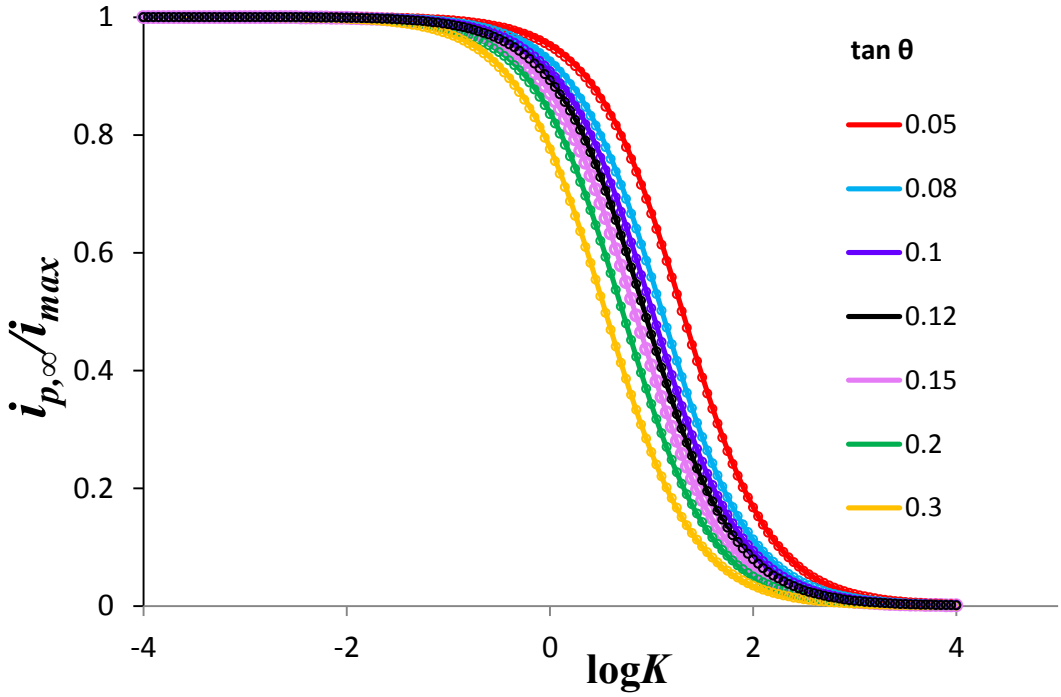

Figure. 3.2.3. Dependences of the normalized current of the neutral species partitioning from the liquid phase inside a nanopipette to the external solution on the partition coefficient calculated for different values of the pipette angle (θ). Solid lines are obtained from Eq. (3.2.2) and circles are simulated data for the values of tanθ shown in the colour legend. The current is normalized by the i_{max} value calculated for the corresponding θ. RG = 1.5.

Current-distance curves and collection efficiencies for the ET/IT mode.

The diffusion problem for the ET/IT mode (Appendix) was solved using COMSOL Multiphysics commercial simulation package. The simulation space included two domains, corresponding to the outer aqueous solution (phase 1) and the inner organic solution (phase 2) in Figure 3.2.2. $C_{R,1}$ and $C_{O,1}$, and $C_{R,2}$ and $C_{O,2}$ are the normalized concentrations of reduced (e.g., FDM) and oxidized (e.g., FDM^+) forms of redox species in domain 1 and domain 2, respectively (see Appendix). Initially, $C_{R,2} = 1$ and all the other concentrations are set at 0. At the ITIES, the boundary conditions (A6.a) - (A6.d), which represent the partion equilibrium for the neutral R species and the Nerstian IT of cationic O species, had to be implemented in the form of kinetic equations because of COMSOL requirements:

$$D_{R,1}\left[\frac{\partial C_{R,1}(R,Z)}{\partial Z}\right] = K_1 C_{R,1}(R,Z) - K_2 C_{R,2}(R,Z)$$

$$0 \le R \le 1,\ Z=0 \qquad (3.2.3a)$$

$$D_{R,2}\left[\frac{\partial C_{R,2}(R,Z)}{\partial Z}\right] = K_1 C_{R,1}(R,Z) - K_2 C_{R,2}(R,Z)$$

$$0 \le R \le 1,\ Z=0 \qquad (3.2.3b)$$

where $K_1/K_2 = K$; and both K_1 and $K_2 \rightarrow \infty$.

$$D_{O,1}\left[\frac{\partial C_{O,1}(R,Z)}{\partial Z}\right] = K_{11} C_{O,1}(R,Z) - K_{22} C_{O,2}(R,Z);$$

$$0 \le R \le 1,\ Z=0 \qquad (3.2.4a)$$

$$D_{O,2}\left[\frac{\partial C_{O,2}(R,Z)}{\partial Z}\right] = K_{11} C_{O,1}(R,Z) - K_{22} C_{O,2}(R,Z);$$

$$0 \le R \le 1,\ Z=0 \qquad (3.2.4b)$$

where $K_{22}/K_{11} = \exp(\frac{zF}{RT}(E_T - E^{\circ\prime}))$; and both K_{11} and $K_{22} \rightarrow \infty$.

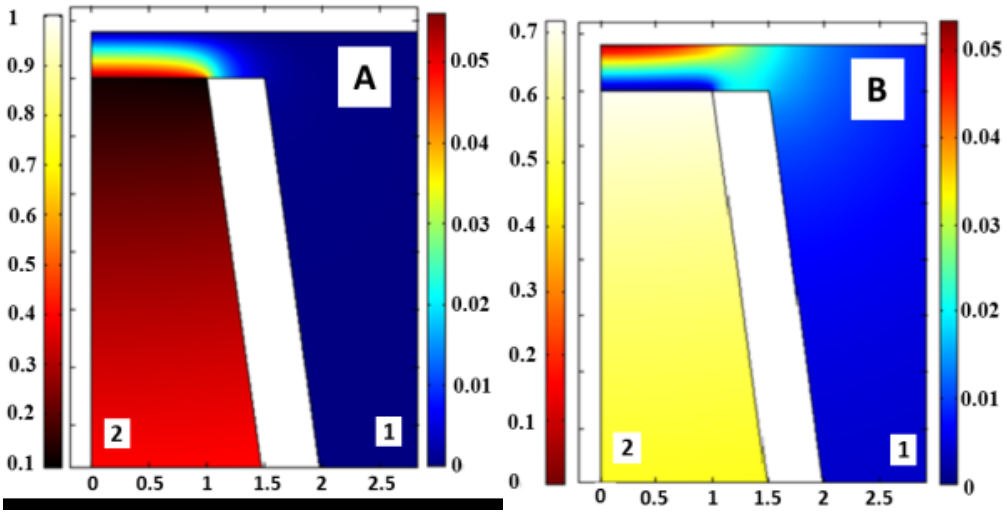

Figure.3.2.4. Simulated concentration profiles of (A) R and (B) O species near the pipette orifice. In both panels, the right color bar is for domain 1, and the left one for domain 2. $L = 0.4$. $\theta = 8°$.

In simulations of approach curves, the normalized tip/substrate distance (L) was varied between 0.001 and 10. An example of computed concentration profiles of O and R in both phases in the proximity of the pipette tip is shown in Figure 4 for $L = 0.4$ and $K = 2$, corresponding to FDM.

From Fig. 3.2.4, one can see that the diffusion fields of both O and R are confined to the narrow gap between the pipette tip and the conductive substrate surface. Thus, the spatial resolution of the ET/IT mode is determined by the pipette radius similarly to the feedback mode SECM experiments. However, unlike the feedback (and SG/TC) mode, the pipette is the sole source of the mediator species, whose concentration in the external bulk solution, outside the tip/substrate gap is negligibly low.

It is interesting to notice that the flux of partitioning neutral species from the pipette to external solution depends on the tip/substrate separation distance. Such dependences are shown in Figure 3.2.5 for three different K values, i.e., 150 (red curve), 2 (green) and 0.001 (black). At the "infinite" separation distance (i.e., $L = d/a >> 1$), the normalized partitioning current

(i_p/i_{max}) equals the $i_{p,\infty}/i_{max}$ value that can be calculated from Eq. (3.2.2) for specific K and θ. When $K \to 0$, $i_p/i_{max} = 1$, regardless of L. However, at higher K, $i_{p,\infty}/i_{max} < 1$, and i_p increases with distance between the tip and conductive substrate. The pipette angle, θ = 8° decreasing L because the substrate reaction shifts the partitioning equilibrium. The larger the K the sharper the increase in i_p near the conductive surface (cf. red and green curves in Fig. 3.2.5) is. At $L \to 0$, $i_p = i_{max}$ for any K. With $K >> 1$, very little R can be delivered to the external solution until $L <$ ~0.5 (red curve), while with K =2 (green curve), $i_p \approx 0.8 i_{max}$ at L = 10. Those curves shown in Fig. 5 were simulated with the θ = 8° typical of quartz pipettes. The shape of the i_p vs. L curve depends slightly on the pipette angle. Such curves cannot be recorded directly because partitioning of neutral species does not produce electric current.

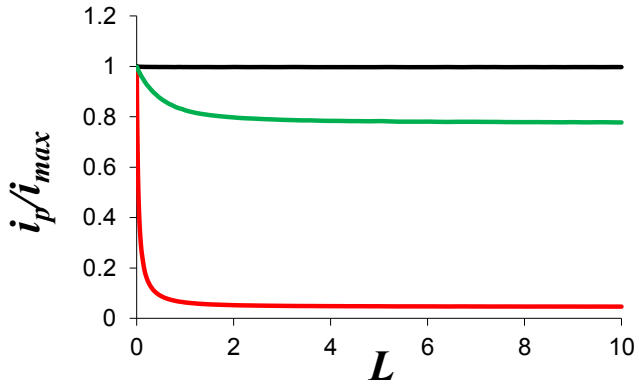

Fig.3.2.5 Normalized flux of neutral redox species with K = 0.001 (black), K = 2 (green), and K = 150 (red), partitioning from the pipette to the external solution, as a function of the separation

Figure 3.2.6 shows the dependence of the substrate current (A) and substrate collection efficiency (B) on the separation distance. In SECM experiments with a conventional metal tip (i.e., with $RG \approx 10$), the collection efficiency at an "infinitely large" substrate is >99% at $d \leq 2$.[27] With $RG \approx 1.5$ typical of nanopipettes, the collection efficiency is only slightly lower (Fig.

3.2.6B). Accordingly, the diffusion-controlled normalized substrate current (i_S/i_{max}) for a strongly hydrophilic mediator (black curve in Fig. 3.2.6A) increases only by ~20% with decreasing separation distance over the range $0 < L < 10$. The current change is somewhat larger for $K = 2$ corresponding to FDM (green curve). In contrast, for more hydrophobic FM ($K = 150$; red curve), i_S/i_{max} is very low until the tip is brought within the distance of ~0.5a from the substrate, and the approach curve is very steep. This trend is similar to that in Fig. 3.2.5. The substrate collection efficiency (i_S/i_p) is largely determined by the L value and independent of K (Fig. 3.2.6B). Both substrate current and collection efficiency plots vary slightly with θ.

The cationic product of substrate reaction (e.g., FM^+ or FDM^+) can diffuse to the tip and transfer across the ITIES, thus producing the IT current. This process is somewhat similar to the SG/TC mode, where the collection current is low when $L >> 1$ (Fig. 3.2.7A). The approach curve is especially steep when the transferred ion is hydrophobic (red curve in Fig. 3.2.7A). In ET/IT experiments with such species (e.g., FM) very close separation distances have to be attained.

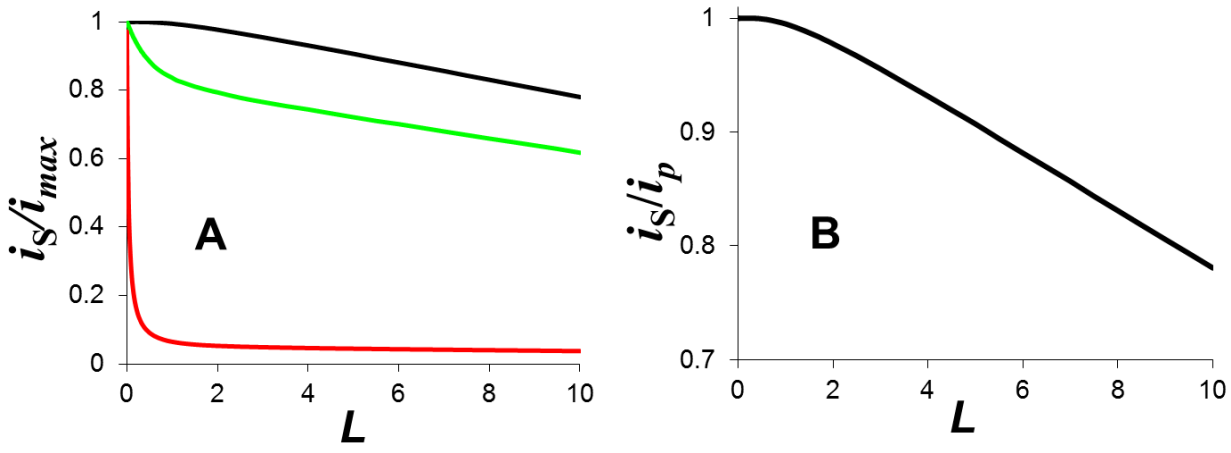

Figure. 3.2.6. (A) Normalized substrate current produced by the oxidation of species with K= 0.001 (black), 2 (green), and 150 (red) as a function of the normalized separation distance; and (B) substrate collection efficiency dependence on L.

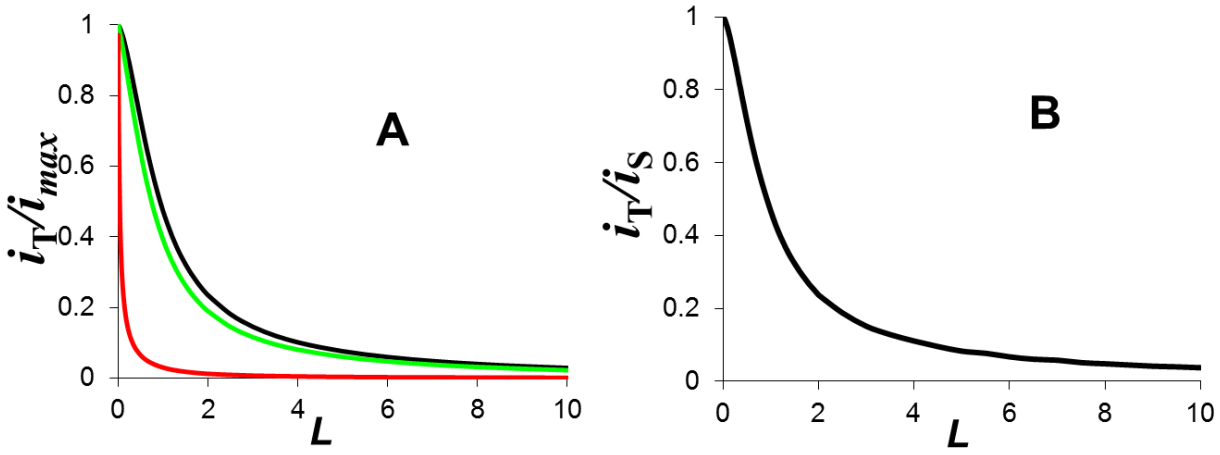

Figure. 3.2.7. (A) Normalized IT tip current produced by the substrate-generated ionic species with K= 0.001 (black), 2 (green), and 150 (red) as a function of the normalized separation distance; and (B) tip collection efficiency dependence on L.

Unlike the SG/TC mode, in ET/IT mode the cationic species are produced only at the portion of large substrate surface facing the pipette tip (see Fig. 3.2.4B), and $i_S \rightarrow 0$ at $L \rightarrow \infty$. Therefore, the tip collection efficiency in the ET/IT mode is larger than in the SG/TC mode, and $i_T/i_S = 1$ at $L = 0$ (Fig. 3.2.7B). The tip collection efficiency is determined by geometry of the of the pipette/substrate gap: it does not depend on K, but varies slightly with θ.

3.2.3 Results and Discussion

ET/IT approach curves and voltammograms Figure 3.2.8 shows cyclic voltammograms of FDM oxidation obtained at different distances between the 12.5-μm radius platinum substrate electrode and a 230 nm-radius pipette containing 36 mM FCM in DCE. As expected, no faradaic current was detected at the "infinite" (>1 mm) separation distance (black curve). Because the substrate radius is much larger than that of the tip, the FDM oxidation current could be detected when the separation distance was as long as 100 μm (blue curve), and it increased slowly as the tip approached the surface (red curve). A voltammogram in Fig. 3.2.8B shows two IT processes:

the transfer of ClO_4^- that can be observed at a positively biased pipette and the transfer of FM^+ (produced by oxidation of FM at the substrate) to DCE at negative tip potentials.

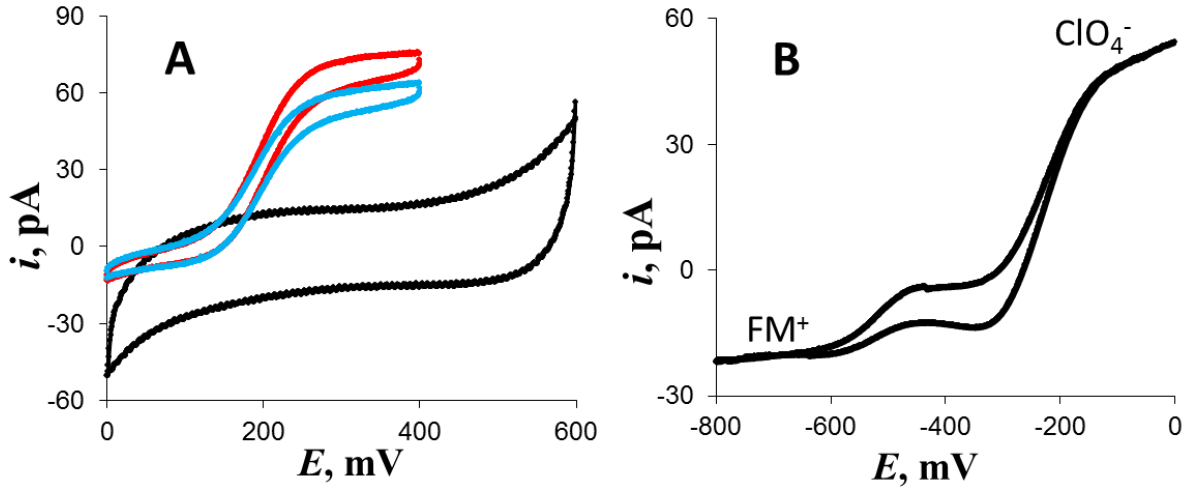

Figure. 3.2.8. ET and IT voltammograms. (A) Cyclic voltammograms of oxidation of FDM at the 12.5-μm Pt substrate at different separation distances, >1 mm (black), 100 μm (blue), and 5 μm (red). The potential sweep rate, *v*, mV/s = 50 (black) and 10 (blue and red). (B) IT voltammogram showing the transfers of ClO_4^- at positive and FM^+ at negative potentials. The 150 nm pipette was positioned near the Pt substrate. E_S = 400 mV.

The approach curve in Fig. 3.2.9A was obtained by measuring the current of the PF_6^- transfer from external solution to DCE inside the pipette at a sufficiently positive potential (E_T = 100 mV). The tip/substrate distance scale can be established and the pipette radius evaluated by fitting such a curve the negative feedback theory.[24] To obtain the ET/IT approach curves with the FDM/FDM^+ mediator, the substrate was biased at +400 mV vs. Ag/AgCl at which FDM was oxidized at the diffusion-controlled rate, the pipette was biased negatively (e.g., E_T = -600 mV) to induce FDM^+ transfer to DCE, and both the substrate and tip approach curves were recorded simultaneously (Fig. 3.2.9B). The IT current-distance curves in Fig. 3.2.9C were obtained using FDM^+ (curve 1) and more hydrophobic FM^+ (curve 2). As discussed above, the latter curve is much steeper, and a significant increase in the tip current could be observed only at very short

separation distances. Thus, the highest current value measured with FM is much lower than that obtained with FDM mediator even though the minimum L value in curve 2 is significantly smaller than that in curve 1. Another typical problem in experiments with hydrophobic mediators is the salt precipitation on the outer pipette wall that may result in partial blockage of its orifice. This problem is more pronounced at higher concentrations of the redox species in the organic filling solution.

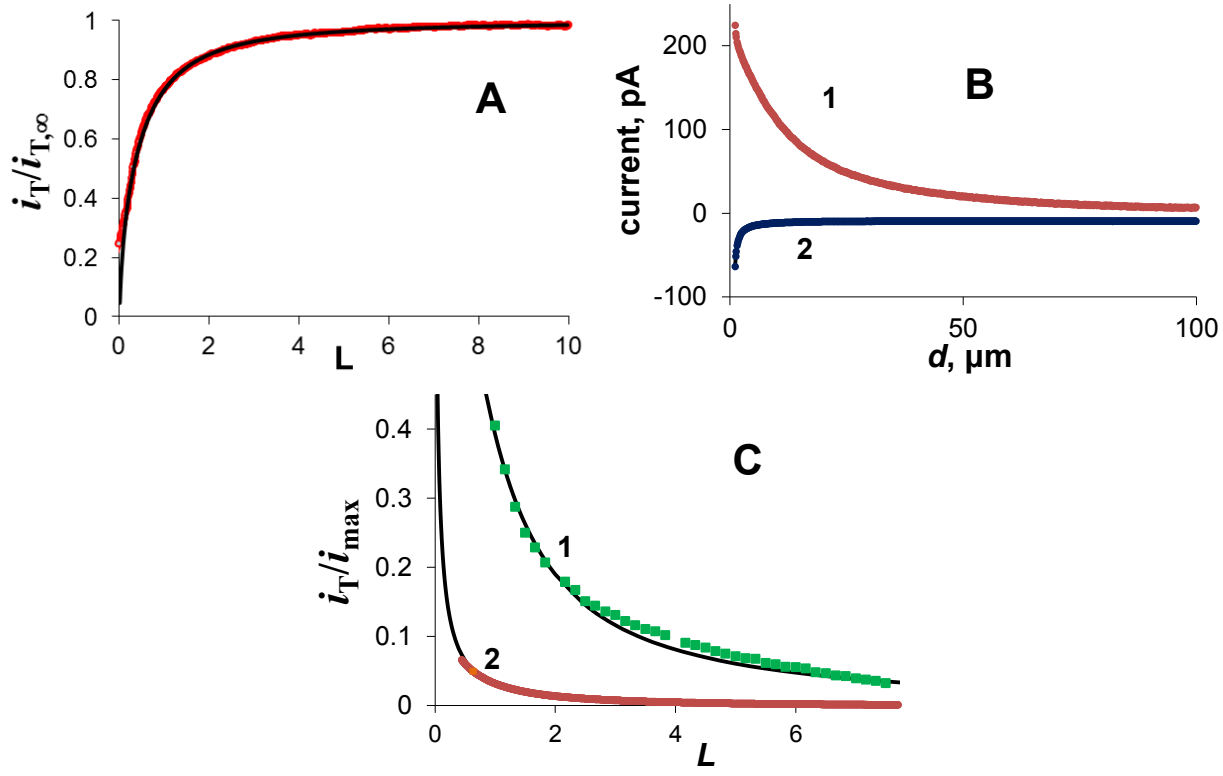

Figure. 3.2.9. Experimental (symbols) and theoretical (lines) IT and ET current-distance curves obtained with pipette probes approaching a 12.5-μm-radius Pt substrate. (A) Negative feedback based on the PF_6^- transfer. $c_{PF_6^-}$ = 0.46 mM. a = 108 nm. E_T = 100 mV. Theoretical curve for RG = 1.3 is from ref. 25b. (B) ET and IT current-distance curves produced by oxidation of FDM at the substrate (1) and transfer of FDM^+ to DCE at the tip (2). a = 375 nm. E_T = -600 mV; E_S = 400 mV. (C) IT approach curves for FDM^+ (curve 1) and FM^+ (curve 2) mediator. c^*_{FDM} in DCE was 15.6 mM (1) and 200 mM (2). a, nm = 135 (1) and 205 nm (2). Theoretical curves are simulated by COMSOL Multiphysics.

Constant-height imaging of substrate topography and reactivity A 90-nm-radius

pipette containing 26 mM FDM in DCE was scanned in a horizontal plane above the Pt disk substrate to obtain constant-height topography (Fig. 3.2.10A) and reactivity (Fig. 3.2.10B) images. Except for a small defect in the lower right corner, prominent topographic features. The negative feedback current of the PF_6^- transfer was the same over the conductive metal surface and the surrounding insulator, and therefore no boundary between Pt and glass can be detected in Fig. 3.2.10A. This boundary is apparent in the reactivity image (Fig. 3.2.10B) because substrate current due to the FDM oxidation was flowing only when the tip was over the Pt surface. The surface topography did not significantly affect the reactivity map in Fig. 3.2.10B because the substrate is essentially flat and smooth. The topographic image (e.g., the one in Fig. 10A) can be used to eliminate the topography effects from and reactivity map of the same substrate area; however, this can be done easier using constant current imaging discussed below. Spatial resolution of both IT- and ET-based images in Fig. 3.2.10 is determined by the pipette radius and is similar to that expected in feedback mode SECM images obtained with a similar size tip and no significant diffusion broadening typical of the SG/TC mode imaging.

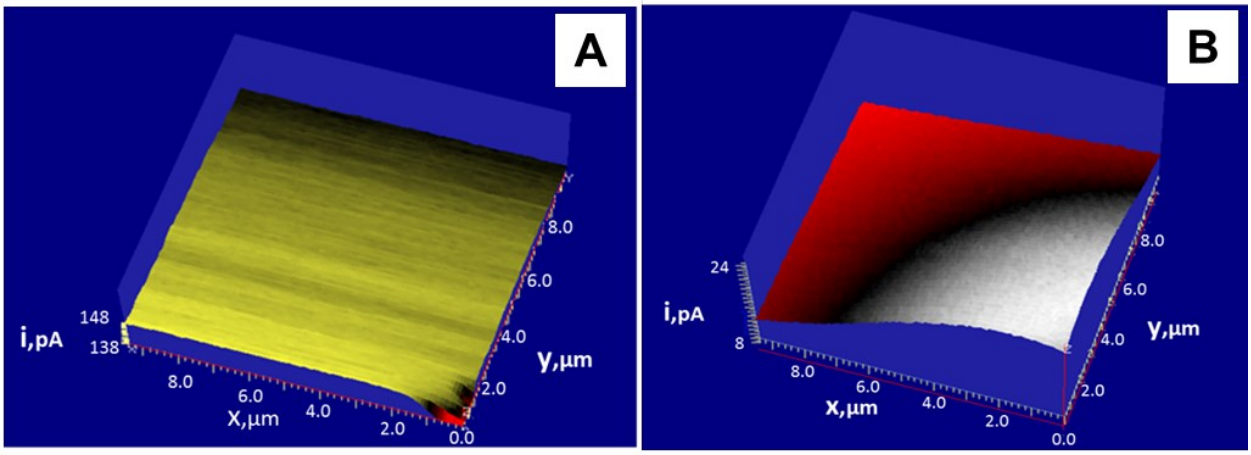

Figure. 3.2.10. Constant-height SECM images of a 10 µm x 10 µm portion of the 12.5 nm-radius Pt disk embedded in glass obtained with a 90 nm-radius pipette tip. (A) Topography image produced by negative IT current of PF_6^- transfer. (B) Substrate reactivity map produced by oxidation current of FDM partitioning from 26 mM DCE filling solution. External aqueous solution contained 1 mM $LiPF_6$. E_S = 300 mV; E_T = 0 mV. The scan rate was 1 µm/s.

A 1 μm x 1 μm IT image of a commercial SEM test specimen, consisting of 30 nm to 500 nm Au particles attached to the carbon substrate, was obtained with a 93-nm pipette tip (Fig. 3.2.11C). An approach curve for the PF_6^- transfer (Fig. 3.2.11A) is in good agreement with the theory. From the AFM image (Fig. 3.2.11B), the dimensions of Au particles are comparable to the pipette radius. The needle-like shape of the pipette probe with a very small *RG* (~1.5) was essential for SECM imaging of such a rough sample without breaking the tip.

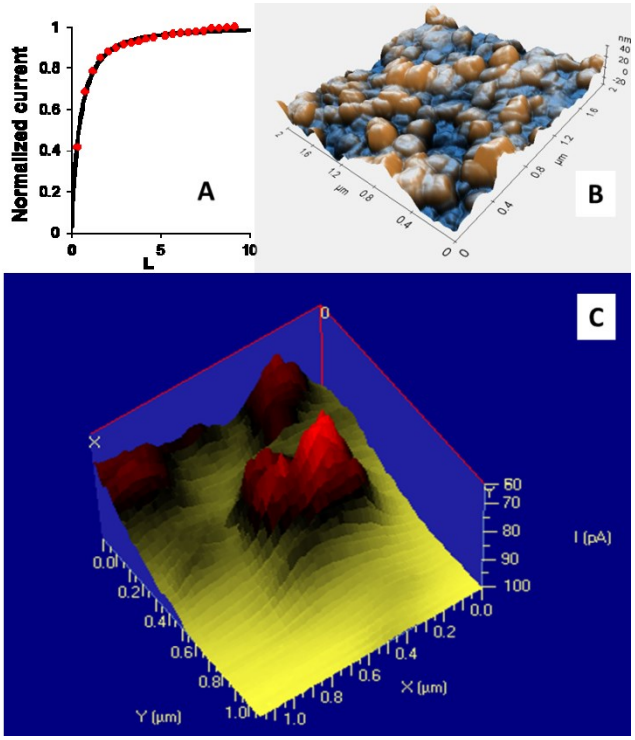

Figure. 3.2.11. Theoretical (solid line) and experimental (symbols) IT SECM approach curves (A) and AFM (B) and SECM (C) topographic images of polydisperse gold nanoparticles attached to the carbon substrate. The approach curves in (A) and the image in (C) are based on the negative feedback current of the PF_6^- transfer. a = 93 nm.

In Figs. 3.2.10 and 3.2.11, the pipette was biased at a positive potential to transfer PF_6^-. Simultaneous ET and IT mapping of substrate reactivity can be carried out by applying

sufficiently negative potential to the pipette by monitoring the transfer of the oxidized mediator species to DCE (Fig. 3.2.12). The contrast between Pt and glass reactivities is apparent in both the ET current map (Fig. 3.2.12A), a the FDM^+ flux distribution (Fig. 3.2.12B) recorded over the same area of substrate surface. The "dips" (lower current areas) in Fig. 12B are more prominent than the corresponding dark spots in Fig. 3.2.12A. These features correspond to the areas of lower activity due to dust particles or other impurities on the substrate surface. Clearly, the IT tip current is much more sensitive to reactivity variations than the ET current at a much larger substrate. By carefully adjusting the substrate potential, it was possible to attain a stable pA-range background current at the micrometer-sized substrate. With a macroscopic substrate, the background current and noise should impair reactivity imaging based on the recording of substrate current, but the tip current-based imaging is feasible regardless of the substrate size.

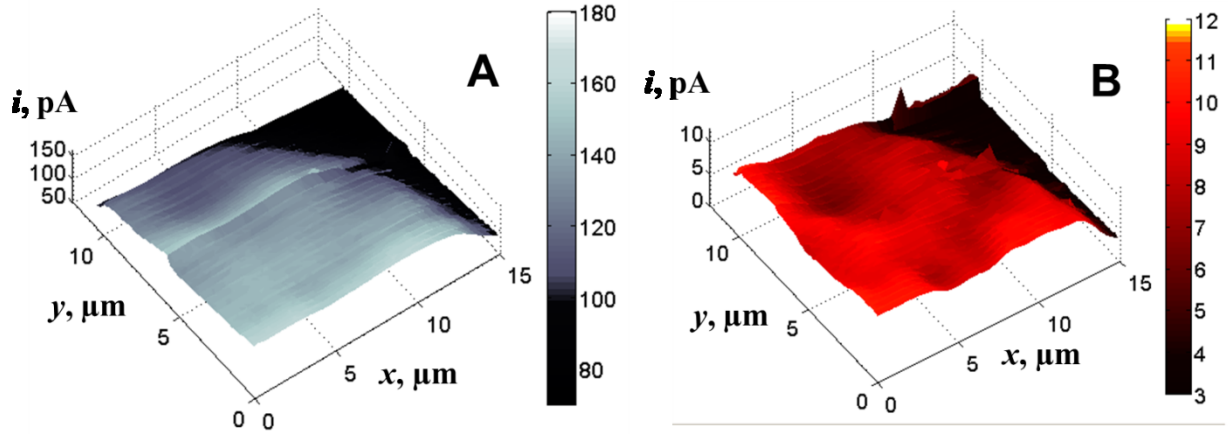

Figure.3.2.12. ET substrate current (A) and IT tip current maps of FDM oxidation at the 12.5 µm-radius Pt substrate obtained with a 375 nm-radius pipette tip. Pipette contained 36 mM FDM in DCE. Aqueous solution contained 100 mM KCl and 0.46 mM $LiPF_6$. E_S = 400 mV; E_T = -550 mV.

Constant-current imaging The implementation of constant-current imaging in the ET/IT mode of the SECM operation is straightforward. The topographic image based on the PF_6^- transfer (Fig. 3.2.13A) was recorded simultaneously with the substrate reactivity map (Fig.

3.2.13b). The well-polished substrate appears flat, and the Pt/glass boundary cannot be detected in the topographic image (Fig. 3.2.13A). A minor tilt due to the imperfect tip/substrate alignment resulted in ~100 nm variation in z between the lower left and the upper right corner (~20 μm distance). The IT tip current was kept constant by means of a digital PID loop controller, using i_T as input signal and tip position (z) as output signal to control the separation distance. Since both Pt and glass are impermeable to PF_6^- ions, the SECM feedback was negative over the entire substrate surface, and d remained essentially constant for the entire image.[1,7a,29] The reactivity image (Fig. 3.2.13B) is not affected by substrate topography or by small surface tilt that can be seen in Fig. 3.2.13A. It represents very well the geometry of the Pt/glass boundary, including small protrusions of Pt into glass that can also be seen in the optical micrograph (the insert in Fig. 3.2.13B).

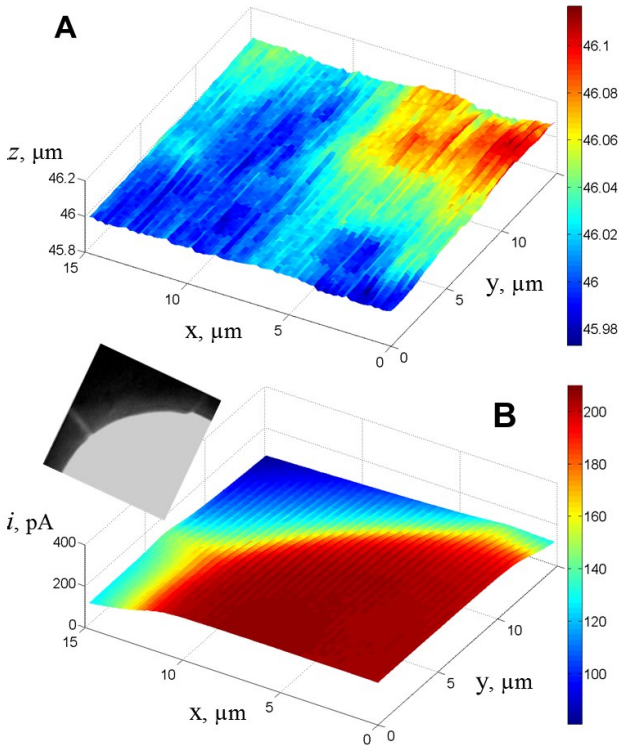

Figure. 3.2.13. Constant-current SECM images of substrate topography (A) and reactivity (B) obtained with a 270-nm pipette tip. The scan rate was 500 nm/s. External aqueous solution contained 0.46 mM $LiPF_6$. E_S = 400 mV; E_T = 200 mV. For other parameters, see Fig. 10. The insert in B is an optical micrograph of the same portion of substrate.

Unlike previously reported versions of dual-probe constant-distance SECM[12] and

SECM/SICM[13,14] imaging, the nanopipette orifice is the only sensing element in an ET/IT probe. Thus, both ET and IT signals originate from the same portion of the substrate facing the pipette orifice, and the physical size of the tip (including glass) can be very small.

3.2.4 Experimental Setup

Chemicals and Materials The following chemicals were used as received: FDM, FM, $LiPF_6$, N, N-dimetyltrimetylsilylamine, KCl, and DCE from Sigma; sodium tetraphenylborate (NaTPB), $LiClO_4$, and tetrahexylammonium chloride (THACl) from Fluka. Tetrahexylammonium tetraphenylborate (THATPB) was prepared by metathesis of NaTPB with THACl in water, and the precipitate was recrystallized twice from acetone. All aqueous solutions were prepared from deionized water (Milli-Q, Millipore Corp.).

Preparation of pipette probes and substrates

The nanopipettes were fabricated from 15 cm long borosilicate capillaries (o.d./i.d. of 1.0/0.58 mm, no filament; Sutter Instrument Co., Novato, CA), using a laser-based pipette puller (P-2000G, Sutter Instrument Co.), as described previously.[24] Representative pulling parameters are HEAT = 420, FILAMENT = 4, VELOCITY = 13, DELAY = 130, PULL = 120. To render the inner glass wall of a pipette hydrophobic, it was silanized by the N, N-dimetyltrimetylsilylamine vapour, using a slightly modified version of the procedure described by the Amemiya group.[28] Briefly, the pipettes were fixed in a mini-vacuum desiccator (Scienceware, Sigma-Aldrich), which was connected to a Thermocouple Gauge Controller (KJLC 205 Series, Kurt J. Lesker Co.) and a pump (RV8, Edwards Co.). The desiccator was first evacuated by the pump (Fig. 3.2.14A), and then the silane vapor was delivered from the flask to the desiccator (Fig. 3.2.14B), where the pipettes were exposed to it for about 15 minutes. The system was evacuated again to remove the silane vapor before taking out the pipettes. The

silanized pipettes were filled with an organic solution from the rear, using a small (10 μL) syringe, and a wire was inserted into each pipette from the rear. The approach curves and some images were obtained with a 12.5-µm-radius glass-sealed, polished Pt disk electrode used as a substrate. Another substrate employed in imaging experiments was an SEM low voltage resolution test specimen purchased from Ted Pella, Inc, which was a carbon disk coated with 30 nm to 500 nm Au particles.

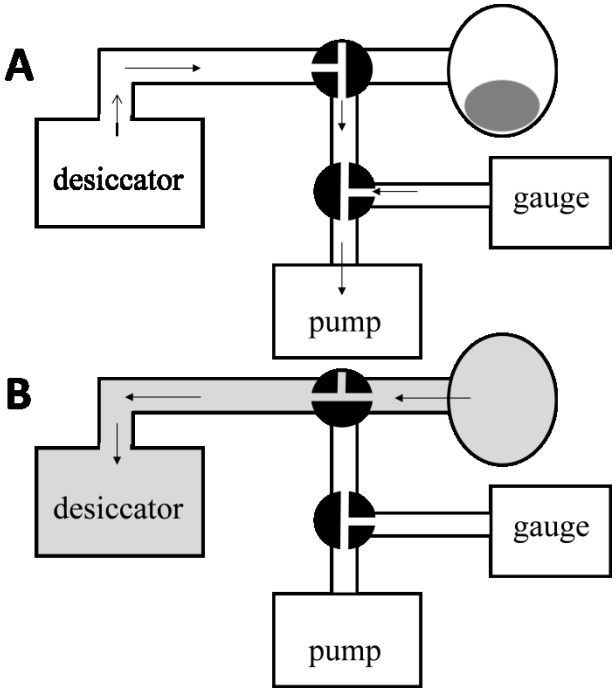

Figure. 3.2.14. Schematics of the silanization process. (A) Evacuation of the desiccator, and (B) delivery of silane vapour to the desiccator.

Electrochemical and SECM measurements Either two or three electrode cell was used, including the pipette probe filled with 10 mM THATPB and either FDM or FM solution in DCE; Ag|AgCl external reference; and either biased or unbiased substrate. The pipette was immersed in external 100 mM KCl aqueous solution to which $LiPF_6$ was added in some experiments. The

voltammograms were recorded with a BAS 100B/W electrochemical workstation (Bioanalytical Systems, West Lafayette, IN.).

The diffusion coefficients of FDM in DCE and in water (1.1×10^{-5} cm^2/s and 7.8×10^{-6} cm^2/s respectively) were determined by steady-state voltammetry at the 12.5-μm-radius Pt disk electrode. The partition coefficient of FDM (K = 2.0) was found by equilibrating DCE solution (10 mL) containing 10 mM THATPB and 26.1 mM FDM with aqueous solution (15 mL) containing 100 mM KCl for ten days and determining concentrations of FDM in both phases by steady-state voltammetry at a 12.5-μm-radius polished Pt disk electrode.

A home-made SECM instrument used to obtain approach curves and images was similar to the one described in ref. 29. In the present instrument, home-written LabView software was used to control a EI-400 four-electrode potentiostat (Cypress Systems) and the tip positioning system. The Thorlabs 2-axis manual translation stage (x-y) and motorized stage (z-axis) were used for coarse tip positioning. Actuation for imaging and fine positioning was through a P-622 NanoCube XYZ piezo stage (Physik Instrumente) driven by an E-621.CR piezo controller (Physik Instrumente). A home-built digital proportional-integral-derivative (PID) loop controller using tip current as input signal and tip position as output signal was constructed to control the vertical position of the tip during constant current imaging.[29] To obtain an SECM approach curve, the pipette was first positioned a few hundred micrometers above the substrate surface using positioning stages. To avoid crashing, this process was monitored with long-distance video microscope. Then, the pipette was moved closer to the substrate in the automated "surface hunter" mode until the tip current produced by the transfer of PF_6^- decreased by ~10%. Both the substrate current and tip currents were collected during the subsequent fine approach.

3.2.5 Conclusions

We developed the theory and carried out proof-of-concept experiments for the ET/IT mode of the SECM operation. It combines the advantages of the reagent delivery from a nanopipette with those of feedback and SG/TC modes. These include high spatial resolution typical of feedback mode imaging and high sensitivity that can enable the detection of low signals produced by small objects (e.g., surface-bound nanoparticles) and slow heterogeneous processes. The ET/IT SECM measurements are not affected by diffusional broadening and elevated background signal that plague SG/TC mode experiments. The careful choice of the redox couple is essential for ET/IT experiments: one form has to be neutral and sufficiently soluble in both water and organic solvent, and the second—ionic form—must be readily transferable across the ITIES. Besides several ferrocene (and other metallocene) derivatives, potentially suitable redox couples include I_2/I^-, Br_2/Br^-, $TMPD^{0/+}$, and possibly H_2/H^+.

Two independent signals (i.e., ET and IT currents) provide for straightforward distance control and separation of surface topography and reactivity features with no need for a dual-probe tip, the second redox mediator, or additional hardware components previously employed for constant-distance imaging.[5,7,8-14]

Although the focus of this article was on diffusion-controlled processes, the ET/IT mode is potentially useful for reaction rate imaging and quantitative kinetic measurements in chemical and biological systems. The absence of redox mediator species in bulk solution can be advantageous for such studies.

3.2.6 Appendix

Steady-state diffusion problem for the ET/IT mode

The steady-state diffusion problem for the ET/IT mode of the SECM operation is formulated for neutral, reduced species (R) and cationic species (O) in two liquid phases—the external solution (phase 1) and the filling solution inside the pipette (phase 2), as shown in Fig. 2. With supporting electrolyte present in both phases, the corresponding differential equations s in cylindrical coordinates are:

$$\frac{\partial^2 c_{R,i}}{\partial r^2} + \frac{1}{r}\frac{\partial c_{R,i}}{\partial r} + \frac{\partial^2 c_{R,i}}{\partial z^2} = 0 \qquad \text{(A1)}$$

$$\frac{\partial^2 c_{O,i}}{\partial r^2} + \frac{1}{r}\frac{\partial c_{O,i}}{\partial r} + \frac{\partial^2 c_{O,i}}{\partial z^2} = 0 \qquad \text{(A2)}$$

where r and z are the coordinates in directions parallel and normal to the substrate base plane, respectively, and $c_{R,i}(r,z)$ and $c_{O,i}(r,z)$ are the concentrations of R and O species, respectively; and i = 1 and 2 correspond to phase 1 and phase 2. The normalized dimensionless variables can be introduced as follows:

$$R = r/a \qquad \text{(A3. a)}$$

$$Z = z/a \qquad \text{(A3. b)}$$

$$C = c/c^* \qquad \text{(A3. c)}$$

$$L = d/a \qquad \text{(A3. d)}$$

$$RG = r_g/a \qquad \text{(A3. e)}$$

$$RS = r_s/a \qquad \text{(A3. f)}$$

$$D = l/a \qquad \text{(A3. g)}$$

$$DD = ll/a \qquad \text{(A3. h)}$$

where c^* is the bulk concentration of R in the filling solution, r_g is the insulator radius, d is the

tip/substrate separation distance, r_s is the simulation space limit in the radial direction, and *l* and *ll* are the z coordinates of the simulation limit behind the pipette orifice in phase 1 and phase 2, respectively. The flux of R at the pipette orifice, the oxidation current at the substrate and the IT current of O at the pipette orifice were calculated by solving the following diffusion problem in the dimensionless form:

$$\frac{\partial^2 C_{R,1}}{\partial R^2} + \frac{1}{R}\frac{\partial C_{R,1}}{\partial R} + \frac{\partial^2 C_{R,1}}{\partial Z^2} = 0; \qquad 0 \le \mathrm{R} < \mathrm{RS}, \quad -\mathrm{D} < \mathrm{Z} < \mathrm{L} \qquad \text{(A4.a)}$$

$$\frac{\partial^2 C_{R,2}}{\partial R^2} + \frac{1}{R}\frac{\partial C_{R,2}}{\partial R} + \frac{\partial^2 C_{R,2}}{\partial Z^2} = 0;$$

$$0 \le R < 1 - Z\tan\theta, -DD < Z < 0 \qquad \text{(A4.b)}$$

$$\frac{\partial^2 C_{O,1}}{\partial R^2} + \frac{1}{R}\frac{\partial C_{O,1}}{\partial R} + \frac{\partial^2 C_{O,1}}{\partial Z^2} = 0; \qquad 0 \le R < RS, \quad -D < Z < L \qquad \text{(A4.c)}$$

$$\frac{\partial^2 C_{O,2}}{\partial R^2} + \frac{1}{R}\frac{\partial C_{O,2}}{\partial R} + \frac{\partial^2 C_{O,2}}{\partial Z^2} = 0;$$

$$0 \le R < 1 - Z\tan\theta, -DD < Z < 0 \qquad \text{(A4.d)}$$

$$C_{R,1}(R,Z) = 0; \quad 0 \le R \le RS, \; Z=L \quad \text{(substrate surface)} \qquad \text{(A5.a)}$$

$$D_{R,1}\left[\frac{\partial C_{R,1}(R,Z)}{\partial Z}\right] = -D_{O,1}\left[\frac{\partial C_{O,1}(R,Z)}{\partial Z}\right]$$

$$0 \le R \le RS, \; Z=L \quad \text{(substrate surface)} \qquad \text{(A5.b)}$$

$$\frac{C_{R,2}(R,Z)}{C_{R,1}(R,Z)} = K; \qquad 0 \le R \le 1, \, Z=0 \quad \text{(pipette orifice)} \qquad \text{(A6.a)}$$

$$D_{R,1}\left[\frac{\partial C_{R,1}(R,Z)}{\partial Z}\right] = D_{R,2}\left[\frac{\partial C_{R,2}(R,Z)}{\partial Z}\right]$$

$$0 \le R \le 1, \, Z=0 \qquad \text{(pipette orifice)} \qquad \text{(A6.b)}$$

$$D_{O,1}\left[\frac{\partial C_{O,1}(R,Z)}{\partial Z}\right] = D_{O,2}\left[\frac{\partial C_{O,2}(R,Z)}{\partial Z}\right]$$

$$0 \le R \le 1, \, Z=0 \qquad \text{(pipette orifice)} \qquad \text{(A6.c)}$$

$$\frac{C_{O,1}(R,Z)}{C_{O,2}(R,Z)} = \exp(\frac{zF}{RT}(E_T - E^{\circ\prime}))$$

$0 \le R \le 1, Z = 0$ (pipette orifice) (A6.d)

where E_T is the applied interfacial voltage and z and $E^{\circ\prime}$ are the ionic charge and formal IT potential of species O, respectively.

$$\frac{\partial C_{R,1}(R,Z)}{\partial n} = 0, \qquad \frac{\partial C_{O,1}(R,Z)}{\partial n} = 0$$

$-D \le Z \le 0$, $R = RG - Z\tan\theta$ and $Z=0$, $1 \le R \le RG$ (outer pipette wall) (A7.a)

$$\frac{\partial C_{R,2}(R,Z)}{\partial n} = 0\,, \qquad \frac{\partial C_{O,2}(R,Z)}{\partial n} = 0$$

$-DD \le Z \le 0$, $R = 1 - Z\tan\theta$ (inner pipette wall) (A7.b)

where $\partial C(R,Z)/\partial n$ is the normal derivative on the surface of the insulating glass.

$$C_{R,2}(R,Z) = 1, C_{O,2}(R,Z) = 0$$

$0 \le R < 1 + DD\tan\theta$, $Z = -DD$ (simulation space limit) (A8.a)

$$C_{R,1}(R,Z) = C_{O,1}(R,Z) = 0$$

$1 + D\tan\theta < R \le RS$, $Z = -D$ and $-D < Z < L$, $R = RS$ (simulation space limit) (A8.B)

$$\frac{\partial C_{R,i}(R,Z)}{\partial R} = \frac{\partial C_{O,i}(R,Z)}{\partial R} = 0$$

$R = 0$, $-DD \le Z \le L$ (axis of symmetry) (A9)

Chapter IV

Resistive Pulse Measurements with Nanopipettes: Detection of Au Nanoparticles and Nanoparticle-Bound Anti-peanut IgY

4.1 Introduction

A family of sensing devices based on measurement of the ion current flowing through a microscopic aperture includes solid-state nanopores,[1] artificial ion channels,[2] and carbon nanotubes.[3] The ability to detect single particles that can enter a microscopic pore and partially block the current is common to all these devices, known as resistive-pulse sensors. A number of sensing schemes employing these devices have been developed and used for DNA detection and sequencing,[4] studies of transport processes at the level of single molecules,[5] ion-selective sensing,[6] detecting single molecules,[1c,7] biosensing,[1a,3b,8] and, single ion-channel recording.[9] Various types of nanopores have been employed for resistive-pulse sensing,[10] which is conceptually similar to the classical Coulter counter. The advantages of resistive-pulse biosensing are widely recognized. The recorded current pulses are single-molecule (or single-particle) events; hence the possibility of the ultralow detection limit.[3,7,11]

In this article, we develop a new methodology for quantitative resistive-pulse sensing with nanopipettes and demonstrate the use of nanopipette-based sensors for selective detection of antibodies to peanut allergens (IgY).[12] Peanut and tree nut allergy related symptoms affect ~1 % of all Americans.[13] Peanut allergens are glycoproteins that elicit immune responses elevating IgE antibody levels in the human body. Arachis hypogaea glycoprotein peanut allergens Ara h1, Ara h2, and Ara h3 are the major glycoprotein allergens that elicit specific IgE response (sIgE) due to epitopes of protein in allergic patients.[14a] Peptide sequence of Ara h1 induces specific IgE levels that can be measured in serum and that may aid in detecting the likelihood of severe allergy episodes. Ara h2 is an abundant glycoprotein present in nuts, and is considered the most potent

peanut allergen that is most frequently recognized by specific IgE from allergic individuals.[14] Here, we used the Ara h 2-2 peptide sequence for detection of anti-peanut chicken IgY, a model antibody for human IgEs with a similar 3-D structure.[15] Ara h 2-2 peptide-modified gold nanoparticles were employed to capture IgY offline from solution for detection using a nanopipette-based sensor.

In resistive-pulse sensing,[10] a detectable particle—or a biomolecule—must be sufficiently small to pass through the pore orifice, but at the same time large enough to cause a measurable change in the recorded ion current, Δi. In most cases, $\Delta i < 0$; however, increases in apparent conductivity of the pore during the translocation event have also been reported[16]. Individual blocking events on the millisecond or sub-millisecond time scale can be recorded using a patch clamp amplifier or a similar device.

Nanopipettes are similar to nanopores in having a nanometer-sized orifice that can sense the analyte species entering and partially blocking the aperture.[17] The ion current (i_0) is driven by voltage applied between two reference electrodes placed inside and outside of the nanopipette (Fig. 4.1A). A nanopipette offers several important advantages including the ease of fabrication, small physical size (the outer diameter of the pipette tip can be as small as ≤10 nm)[18], and the needle-like geometry, which makes it suitable as a probe for scanning probe microscopies.[17,19-21] Few applications of nanopipettes to resistive-pulse sensing have been reported,[11,22,23] and methodology for characterizing the inside geometry of a pipette, which is essential for such measurements, has yet to be developed. The two main geometric parameters are the pipette radius (a) and the pipette angle (θ; Fig. 4.1B), which define the shape of the narrow tapered shaft adjacent to its tip and therefore largely determine the ion current and the pipette resistance. Here we show that pipette geometry can be characterized by combining resistive-pulse

experiments with steady-state voltammetry of ion transfer across the interface between two immiscible electrolyte solutions (ITIES). Then, we use a model system of gold nanoparticles (AuNP), AuNP-peptide allergen and AuNP-peptide allergen particles that have bound IgYs to demonstrate the use of nanopipettes for label-free detection of antibodies.

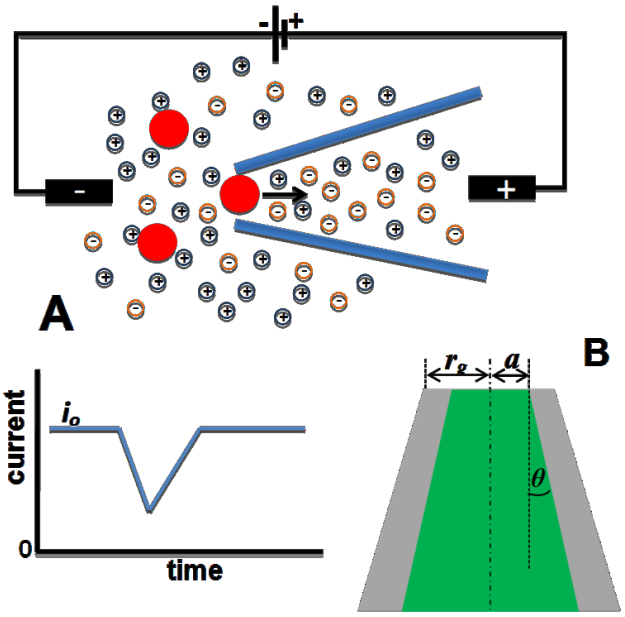

Figure 4.1. (A) Simplified schematic representation of resistive-pulse sensing with a nanopipette. In the presence of nanoparticles, blockage events can be seen in the current vs. time curve. (B) Parameters defining the nanopipette geometry.

4.2 Results and Discussion

Size distribution and zeta (ζ)-potentials of particles. TEM images of different particles used in our experiments are shown in Fig. 4.2, and related size distributions are given in Fig. 4.3. After drying on TEM grids, the particles showed considerable aggregation. To determine the size, we focused on individually isolated particles. The image of commercial citrate-stabilized AuNP (Fig. 4.2A) and the corresponding size distribution (Fig. 4.3A) show an

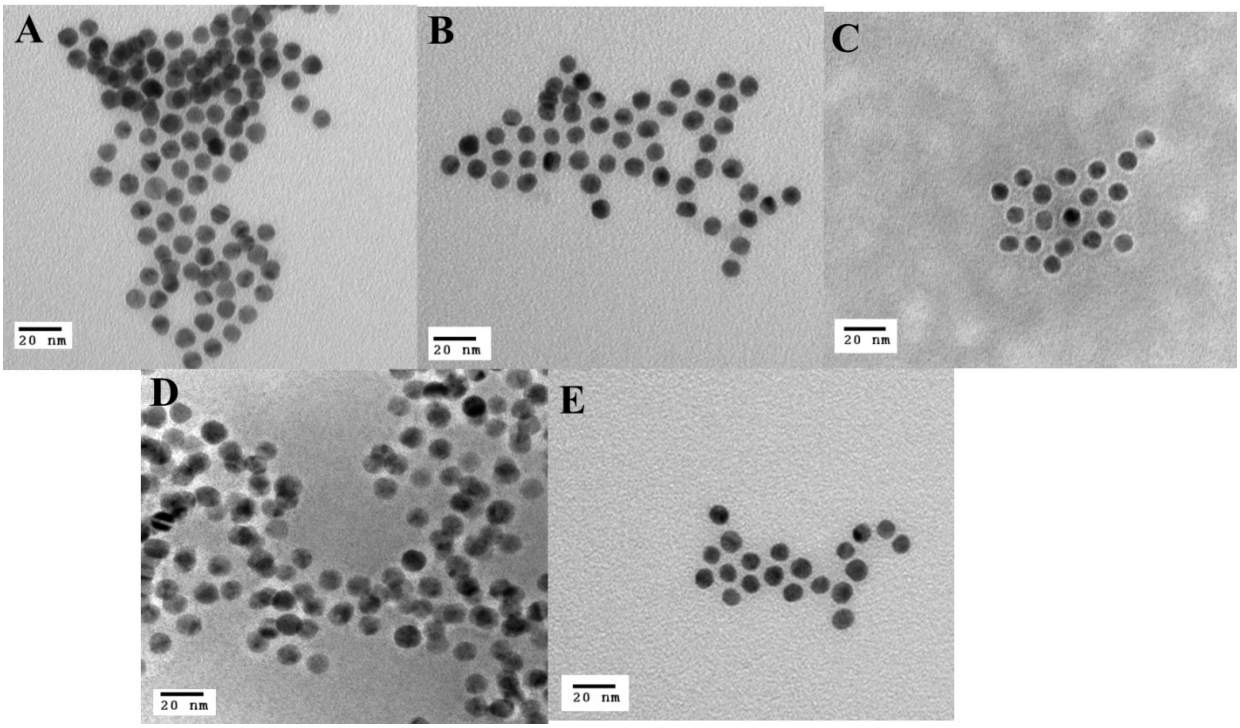

Figure 4.2. TEM images of different nanoparticles: (A) commercial AuNPs, (B) AuNP-MHDA, (C) AuNP-peptide stained by phosphotungstic acid, and (D) Au-peptide-IgY stained by phosphotungstic acid. (E) Control particles: commercial AuNPs stained by phosphotungstic acid.

average diameter of 9.5 ± 0.3 nm in a good agreement with the 10 nm nominal particle size given by the manufacturer. In solution, these particles also tend to aggregate, as confirmed by preliminary light scattering experiments. After modification of AuNP with mercaptohexadecanoic acid (MHDA), the average particle diameter (9.6 ± 0.3 nm) remained nearly the same (Figs. 4.2B and 4.3B) which is consistent since the organic layer is not visible in TEM. AuNP-peptide and AuNP-peptide-IgY were stained with 0.5% phosphotungstic acid so that their surface layers could be visualized. Here, particles with no aggregation and a larger diameter than the AuNP-peptide were specifically sought out for imaging so that we could characterize the sizes of particles assumed to be AuNP-peptide-IgY. Significant aggregation on the TEM grids did not allow counting of different particle types. The somewhat larger diameter of AuNP-peptide particles (13.9±0.8 nm; Figs. 4.2C and 4.3C) corresponds to the thickness of a

peptide monolayer (~4.5 nm). The peptide film appears as a white halo around each particle in Fig 4.2C. The halos around AuNP-peptide-IgY in Fig 4.2D are thicker and less uniform in agreement with the larger average diameter (15.1±1.4 nm) and higher polydispersity (Figs. 4.2D and 4.3D) of these particles. (Control experiments confirmed that the halos were not produced by phosphotungstic acid itself. TEM images of Au nanoparticles pretreated with PTA with neither peptide nor antibodies attached to them exhibited no halo (Fig. 4.2E)).

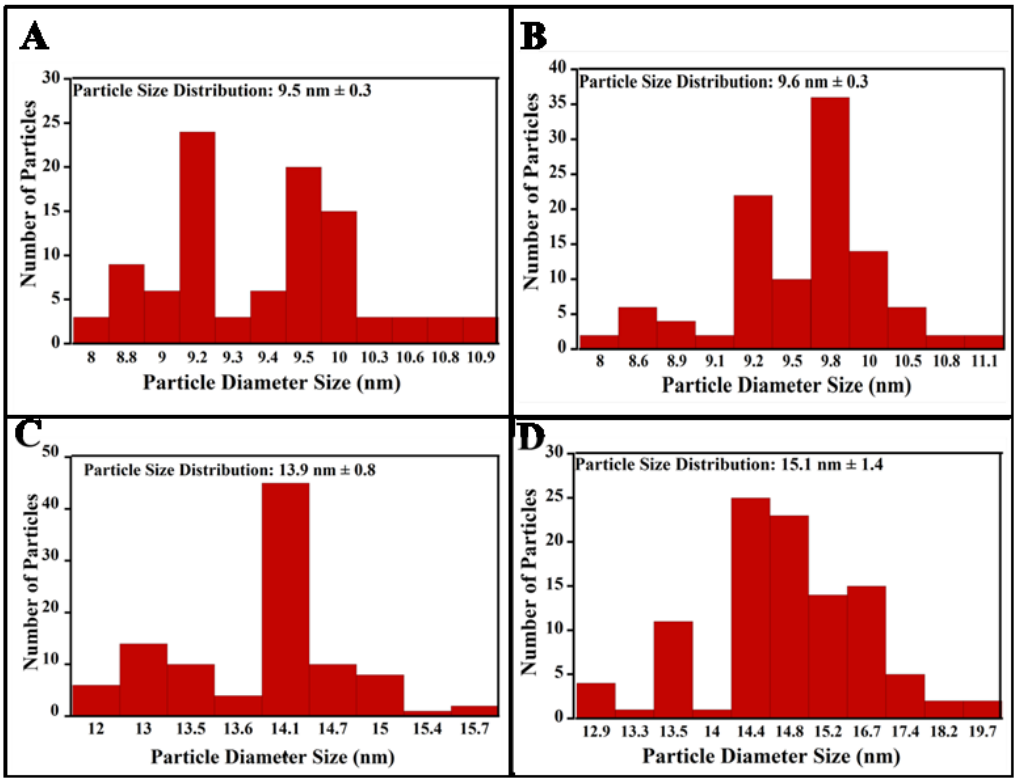

Figure 4.3. Particle size distribution of 110 nanoparticles for (A) commercial AuNPs, (B) AuNP-MHDA, (C) AuNP-peptide, and (D) Au-peptide-IgY.

Zeta potentials were measured for the same four types of particles (Table 4.1). The highest negative value (-52 mV) was obtained for citrate- stabilized AuNPs, while AuNP-MHDA in the presence of Tween-20 exhibited a very small value -4.9 mV. Without Tween-20, the ζ-potential of AuNP-MHDA was somewhat higher (-18 mV), but the surfactant had to be

added to avoid aggregation of these particles. The ζ-potential of AuNP-peptide-IgY was slightly less negative than that of AuNP-peptide.

Table 4.1 ζ-potentials of different nanoparticles

Particle	ζ-potential	Solution
citrate-stabilized AuNP	-52mV	10mM PB (pH 7.0) + 15mM NaCl
AuNP-MHDA	-4.9±2.9 mV	10 mM PB (pH7.0) + Tween-20
AuNP-peptide	-32.3±1.1 mV	10 mM PB (pH 7)
AuNP-peptide-IgY	-25.4±0.4 mV	10 mM PB (pH 7)

Characterization of nanopipettes. The pipette radius was determined from voltammetry at the ITIES performed in the following cell:

Ag|10 mM THATPB + 1mM $TBAClO_4$||15 mM NaCl |AgCl|Ag (1)

DCE *pipette*

Fig. 4.4 shows a typical voltammogram for perchlorate transfer across a water/1,2-dichloroethane (DCE) interface formed at the tip of a quartz nanopipette. With a non-silanized pipette, the diffusion limiting current follows Eq (4.2):[24]

$$i_d = 3.35\pi zFDac \qquad (4.1)$$

where F is the Faraday constant, c, D and z are the concentration, diffusion coefficient, and charge of the transferred ion, respectively, and a is the pipette radius. With $D = 8\times10^{-6}$ cm^2/s measured for ClO_4^- in DCE using larger (i.e., micrometer-sized) pipettes, a = 19 nm was calculated from Fig. 4.4 using Eq. (4.1).

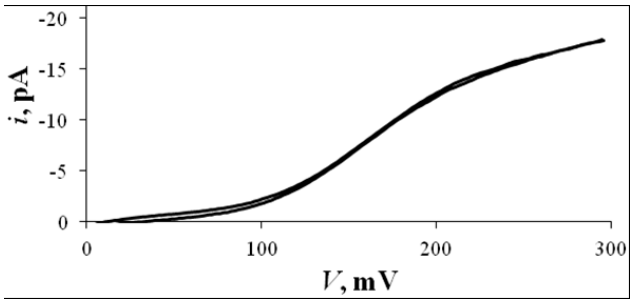

Figure 4.4. Steady-state voltammogram of ClO_4^- transfer across the DCE/water interface obtained with a 19 nm-radius pipette in cell 1 with the potential sweep rate of 50 mV/s.

The pipette angle, θ can be determined in two different ways—from resistance measurements[25a] and by common ion voltammetry.[25b,c] The pipette resistance was found from the current-voltage (*i*-*V*) curves recorded in aqueous solution containing 15 mM NaCl and 10 mM PB (the same solution was used in our resistive-pulse experiments). With a relatively large nanopipette (e.g., a > ~100 nm; Fig. 4.5A), the *i*-*V* curves were essentially linear, and the total resistance, R, could be extracted from the slope. *i*-*V* curves obtained with smaller pipettes were non-linear because of current rectification (Fig. 4.5B);[26] whereas an essentially linear part of such a curve recorded at low applied voltages (e.g., ±20 mV; the inset in Fig. 4.5B) was used for determining R. The total pipette resistance comprises two components, $R = R_{int} + R_{ext}$, i.e., the resistances of the inner and outer solutions. Assuming that the pipette orifice is disk-shaped, R_{ext} is entirely determined by its radius and solution conductivity (κ), $R_{ext} = 1/(4\kappa a)$.[27] θ was evaluated from the internal pipette resistance ($R_{int} = R - R_{ext}$) using a simple analytical approximation[25a]

$$R_{int} = 1/\kappa\pi a \tan\theta \qquad (4.2)$$

The conductivity of 0.1M KCl is 1.29 $\Omega^{-1}m^{-1}$, while that of the buffer solution (15 mM NaCl + 10 mM PB) is 0.294 $\Omega^{-1}m^{-1}$, which was measured by comparing the resistance of these two solutions obtained with the same large pipettes (3 to 20 μm radius). The geometric parameters

and resistances found for several pipettes are summarized in Table 4.2.

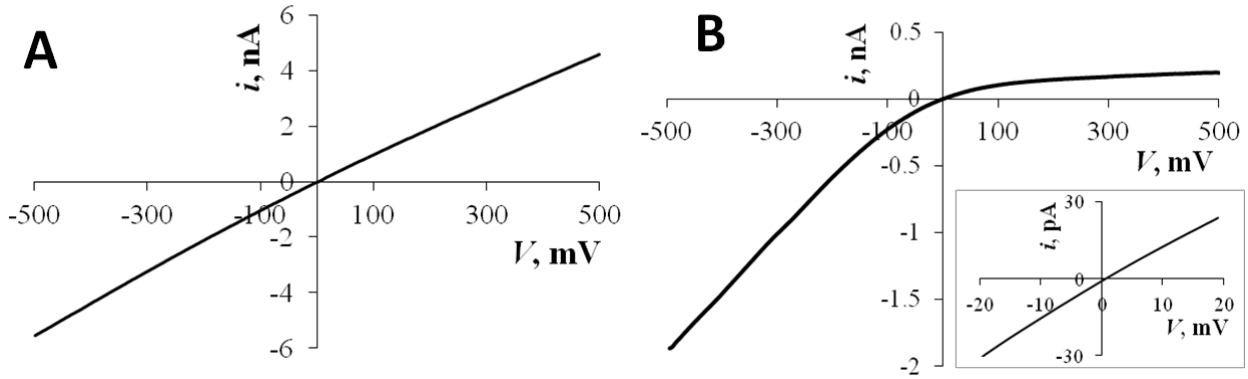

Figure 4.5. *i-V* curves obtained for nanopipettes in 15 mM NaCl + 10 mM PBS (pH 7) *a,* nm = 103 (A) and 12 (B). The inset in B shows the linear part of the *i-V* curve.

Table 4.2 Geometric parameters and resistances of pipettes used in resistive-pulse experiments.

a, nm	R,GΩ	θ, ˚
11	1.05	5.8
12	0.80	7.1
14	0.60	8.2
17	0.55	7.3
54	0.027	11.0

These geometric parameters were used to evaluate the suitability of a given pipette for detecting particles with a specific radius, r_p. The question here is what relative change in ion current ($\Delta i/i_0$) and translocation time (τ, i.e., the width at half pulse height) can be expected when such a particle enters a pipette with the radius *a* and angle θ? To our knowledge, no theory is available in the literature for particle translocation through the pipette tip. Comprehensive numerical modeling of the translocation of spherical particles through conical-shaped nanopores was reported recently.[28] However, the model in ref. 28 did not include electroosmosis, which

was found to be insignificant because of high particle mobility. In our case, the effect of electroosmosis may be more important (see below) and especially difficult to model exactly. Instead, we modified the approximate analytical model previously developed for a spherical particle translocation through a conical nanopore[7] and its slightly refined version,[29] in which the shape of the current pulse was calculated. Unlike the treatments in refs. 7 and 29, we used the measurable θ value instead of the radius of the larger pore orifice, which is not available for a nanopipette. Another important difference is that we determined a independently from ITIES voltammetry rather than calculated from pipette resistance. Although this simplified model does not take into account electroosmosis and double-layer effects, it is suitable for predicting the magnitude of a current pulse and for semi-quantitative analysis of its shape and duration.

The current-time pulses were calculated for the translocation of nanoparticles through pipettes with different a and θ values as shown in Fig. 4.6. Although, the radius of the transferrable particle has to be smaller than that of the pipette, the larger the r_p/a the larger the change in pipette resistance and hence $\Delta i/i_0$ (Fig. 4.6A). For a given r_p/a, the larger the θ the larger the resistive-pulse signal, as shown in Fig. 4.6B. Using 15 mM NaCl + 10 mM PB solution, the range of i_0 in our experiments (below) typically was 100 pA < i_0 < 1 nA, depending on a and the applied voltage. With a typical level of noise in our experiments of ~1 pA and the required signal/noise ratio of ≥3, the smallest detectible $\Delta i_{max}/i_0$ is on the order of 0.01. From Fig. 4.6A, one can see that a pipette with the radius a and a typical θ value of 10° must be suitable for the detection of particles with $a/2 \leq r_p < a$. Particles with $a/4 < r_p < a/2$ may be harder to detect (this depends on the i_0 value); and particles with $r_p \leq a/4$ are almost certainly undetectable. The lower limit for r_p/a is significantly higher with $\theta = 5^\circ$, and lower with $\theta = 15^\circ$ (Fig. 4.6B). By adjusting the pulling program, the pipettes with suitable geometry were

fabricated and characterized before resistive-pulse experiments.

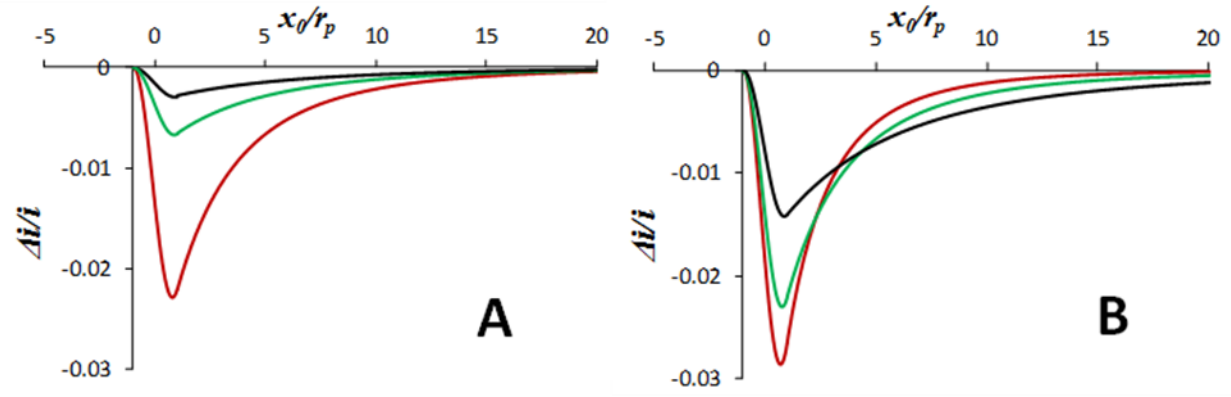

Figure 4.6. Calculated change of current over normalized transferred distance for (A) different r_p/a values: 1/2 (red), 1/3 (green), and 1/4 (black), and θ=10°; and (B) different θ: 5° (black), 10° (green), 15° (red), and r_p/a = 1/2.

Translocation of citrate-stabilized Au nanoparticles (AuNP). The translocation of citrate-stabilized AuNP was used as a model system to explore basic features of current pulses obtained with nanopipettes. Fig. 4.7A shows a typical current-time recording for the translocation of 10 nm AuNPs through a 28-nm-diameter pipette. Unlike a background trace I obtained with no nanoparticles added to the external solution, a number of pulses with the current changes much larger than the noise level can be seen in trace II. With the r_p/a value close to 1/3, $\Delta i/i_0$ is expected to be ~0.01. Thus, smaller current blockages correspond to the translocation of individual AuNPs, while larger spikes are likely to be produced by the particle dimers, which are sufficiently small to penetrate through the 28 nm pipette orifice.

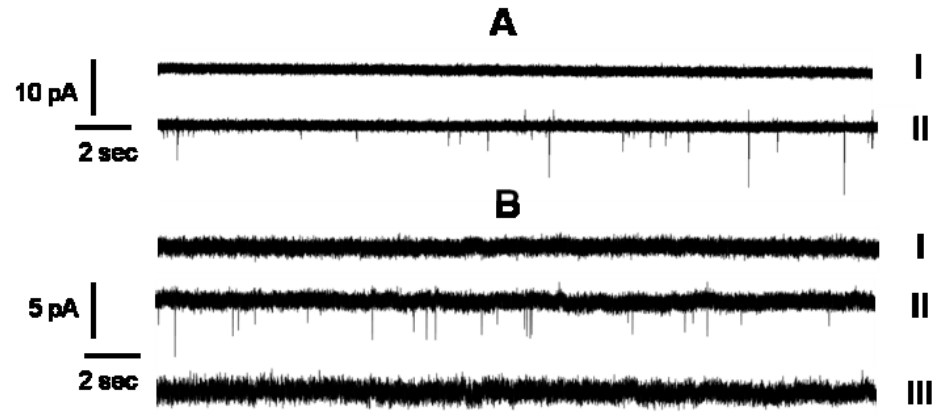

Figure 4.7. Current-time recordings obtained with a (A) 28 nm-diameter and (B) 32 nm-diameter pipette in a 15 mM NaCl + 10 mM PB (pH7). (A) Solution contained: 0 (trace I) and 2 nM (trace II) of 10-nm-diameter AuNP; V = 150 mV. i_0 = 156 pA (I) and 134 pA (II). (B) Solution contained: 0 (I) and 1.8 nM (II, III) of AuNP-peptide. V = 100 mV (I, II) and -100mV (III). i_0 = 222 pA (I) , 233 pA (II) and -363 pA (III).

Trace II in Fig. 4.7A is a part of a series of recordings (the total recording time was 12 min) from which the average spike density was found to be ~0.5 events/s. The comparison of this number to the diffusional flux of AuNPs to the pipette orifice can provide information about the rate-determining step of the overall translocation process. The consecutive steps of this process are the transport of particles to the pipette orifice in the external solution, the ingress of particles into the pipette, and the transport inside the narrow shaft of the pipette. The diffusional flux of electrically neutral particles to the pipette orifice is given by Eq. (4.3)

$$\text{flux} = xD_pc_pa \tag{4.3}$$

where x is a function of r_g/a (r_g is the outer wall radius in Fig.1B; $r_g/a \approx 1.5$ for a typical glass or quartz pipette,[20] corresponding to $x \approx 5$); D_p and c_p are the diffusion coefficient and concentration of AuNPs, respectively. Although AuNPs are negatively charged, the contribution of migration to their flux in the external solution should be small because of a high concentration of

supporting electrolyte in solution and a nm-range pipette radius,[30] and the flux of charged particles can still be evaluated from Eq. (4.3). In Fig. 4.7A, c_p =1.2x10^{12} particles/cm^3, a = 14 nm, and $D_p \approx 2\text{x}10^{-7}$ cm^2/s can be estimated for a 10-nm-diameter particle from the Stokes–Einstein equation at 20 °C. The resulting flux is ~2 particles/s, which is consistent with the 0.5 events/s extracted from the experimental data. Better agreement can be achieved if one takes into account the finite size of a AuNP, which is comparable to the radius of the pipette aperture. Unlike an ion or a small molecule, which can enter the much larger pipette anywhere within its orifice, a nanoparticle has to come in sufficiently close to the pipette center to avoid the collision with the outer wall. For example, in Fig. 4.7A (trace II), a 10-nm-diameter spherical AuNP could enter the 28 nm pipette only if the radial distance between the particle center and the pipette center was ≤9 nm (otherwise, the particle would hit the pipette wall instead of getting inside). Therefore, the apparent orifice radius available for the particle ingress is only 9 nm, and this value (rather than a = 14 nm) should be substituted in Eq. 4.3, yielding the flux value of ~1 particle/s. (Although this number is reasonably close to the experimentally found frequency of blockages, the presented analysis is not strictly quantitative because of the size polydispersity of AuNPs; cf. Fig. 4.3). In contrast, the average pulse duration in the same set of data was ~1 ms, suggesting that ~1000 particles per second could translocate through the pipette if their transport inside the pipette rather than diffusion in the external solution were the rate limiting step (see SI for the discussion of the blockage duration).

It is important to note that current blockages by AuNPs were observed only when a positive potential (e.g., +150 mV in Fig. 4.7A) was applied to the reference electrode inside the pipette with respect to the external reference. This indicates that the translocation of negatively charged AuNP is driven by electrophoresis rather than simple diffusion of particles through the pipette

narrow shaft or electroosmosis. Moreover, the direction of the electroosmotic flow in this case was opposite to that of the electrophoresis.

Translocation of peptide-modified gold nanoparticles. The nanopipette methodology was used to develop a resistive-pulse sensing platform for the detection of antipeanut allergen antibodies. To attain selective detection of IgY, peptide modified 10 nm gold nanoparticles (AuNP-peptide) were prepared using a two-step process, as described in the experimental section. Trace II in Fig. 4.7B shows an example of a current-time recording obtained with AuNP-peptide. The frequency of spikes was 1.2 events/s for 1.8 nM AuNP-peptide, that is of the same order of magnitude as ~ 4.1 particles/s value estimated from diffusion flux [Eq. (4.3)]. As discussed above, a better agreement can be achieved by correcting for the finite particle size. The spikes in Fig. 4.7B are more uniform that those in Fig. 4.7A because Au-peptide dimer particles are too large to penetrate a 32 nm pipette orifice. Similarly to bare AuNP, the translocation of AuNP-peptide is driven by electrophoresis. Trace III in Fig. 4.7B was recorded at V = -100mV. No current pulses were found, indicating that no AuNP-peptide particle transfer at a negative potential.

Pipettes with different diameters were used to detect the polydispersity of Au-peptide particles due to their crosslinking by peptide molecules. Fig. 4.8 shows scatter plots of AuNP-peptide translocation experiments with three different pipettes (rows 1, 3 and 5 in Table 4.2). As discussed above, only single Au-peptide particles (rather than dimers or other aggregates) can enter either 22-nm or 28-nm-diameter pipette. The $\Delta i_{max}/i_0$ for a given pipette is largely determined by the r_p/a value (see SI for more details). Since both pipettes probed the same collection of Au-peptide particles (with the size distribution given by Fig. 4.3C), it is intuitive that the extent of blockage should be larger for a smaller pipette. Accordingly, $\Delta i_{max}/i_0$ values

ranged from 0.023 to 0.156 for the 22 nm pipette (circles) and from 0.006 to 0.045 for the 28 nm pipette (diamonds). The possibility of sizing nanoparticles by resistive-pulse measurements with nanopores based on the relationship between the blockage magnitude and particle size was shown recently.[31] Here, the particle diameter ranges extracted from the recordings obtained with two pipettes are somewhat different, i.e., from 9.4 nm to 17.9 nm (28 nm pipette; mean NP diameter, 13.8 nm) and 12.4 nm to 19.7 nm (22 nm pipette，mean NP diameter, 16.1 nm). By comparing with the particle size shown in Fig.3, those particles could be bare Au (9.5 nm), Au-MHDA (9.6 nm) or Au-peptide (13.9 nm) or Au dimers (19.0 nm). The average pulse width was longer for the 22-nm pipette (1.06 ms) than for the 28-nm pipette (0.82 ms) because of the smaller applied voltage (200 mV vs. 300 mV) and larger r_p/a; the latter factor was especially significant for particle diameters larger than ~15 nm.

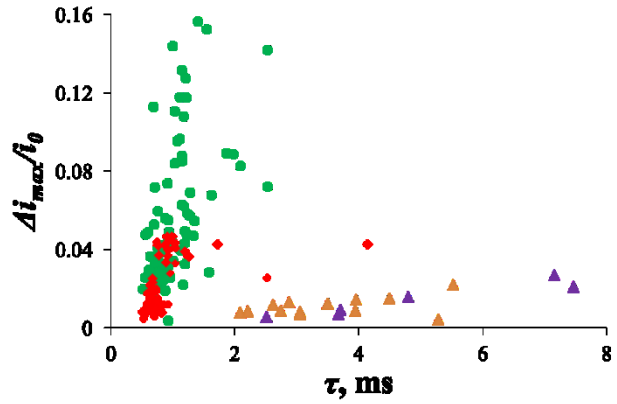

Figure 4.8. Scatter plots of the normalized maximum current change versus peak width for AuNP-peptide translocation experiments with three different pipettes. Pipette diameter (nm): 108 (triangles) 28 (diamonds), and 22 (circles). The applied voltage (mV) was: 200 (green; total recording time 24.3 min), 300 (red; 40 s), 800 (purple; 8 min) and 900 (orange; 15.3 min). For other parameters, see Fig. 4.7.

Two scatter plots obtained with a much larger pipette (108 nm-diameter; triangles) are totally different from other data in Fig. 4.8. This pipette was too large to detect single AuNP-

peptide species, so the recorded pulses must be due to dimers and other aggregates. The $\Delta i_{max}/i_0$ values range from 0.004 to 0.027, which correspond to the particle diameters between 29.6 nm and 56.0 nm, according to the developed theory (SI and Fig. 4.6). As expected, there is no significant difference between the average magnitude of current blockages in the recordings obtained with this pipette at 800 mV (purple) and 900 mV (orange); however the mean pulse width is larger at a lower applied voltage (4.9 ms vs. 3.5 ms), further indicating that the translocation was driven by electrophoresis. Despite higher applied voltage, the translocation of particle aggregates was slower than that of single AuNP-peptide monitored by smaller pipettes.

Translocation of AuNP-peptide-IgY. The current-time recordings for AuNP-peptide-IgY translocations (Fig. 4.9) are completely different from the aforementioned data. In contrast to the current blockages observed at positive potentials in Figs. 4.7A and 4.7B, with AuNP-peptide-IgY the current pulses were found only at negative potentials applied to the inner reference electrode (e.g., -200 mV in Fig. 4.9B), and the direction of the pulse was reversed from that of the other particles. We observed this behavior using several pipettes of different diameters, AuNP-peptide-IgY from two different batches, and different pH values (7.0 and 9.5; data for pH 9.5 not shown). Since the ζ-potential of AuNP-peptide-IgY is negative, the translocation of these particles at negative voltages indicates that electroosmosis dominates over electrophoresis, and the translocation direction is electroosmotic. One reason for this difference is a less negative ζ-potential of AuNP-peptide-IgY as compared to AuNP-peptide and AuNP (Table 4.1). Even with bare AuNPs, the electroosmosis significantly affected the particle transport inside the pipette, resulting in a lower effective mobility. As demonstrated by Firnkes *et al.*[32], the translocation direction of protein molecules through nanopores is determined by the difference of ζ-potentials, $\Delta\zeta = \zeta_{particle} - \zeta_{pore}$, which in ref. 32 was ~10 mV. The change in the voltage sign between AuNP-

peptide-IgY and AuNP-peptide (ζ_{pore} was the same for both particles, and the $\zeta_{particle}$ of AuNP-peptide-IgY is 7 mV less negative) is qualitatively in line with the results in ref. 32. Quantitative analysis of this phenomenon is difficult because of the complicated structure of AuNP-peptide-IgY, and additional factors (e.g., nonuniform charge distribution on the particle) should also contribute to it along with the ζ-potential value.

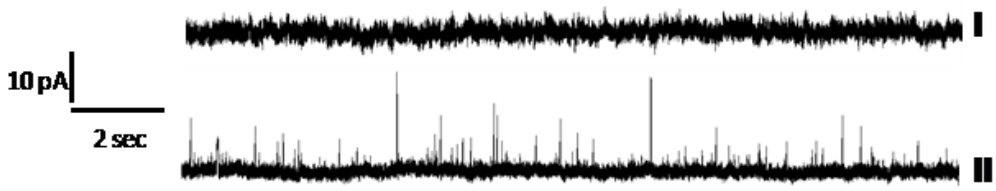

Figure 4.9. Current-time recordings for a 28-nm-diameter pipette in a 15 mM NaCl + 10 mM PB (pH7) solution containing (I) 0 and (II) 1 nM of Au-peptide-IgY particles. V = -200 mV. i_0 = -655 pA (I) and -545 pA (II).

The resistive pulses produced by AuNP-peptide-IgY translocation that reflect increases in the absolute value of the ion current is a striking feature, as opposed to the current decrease in Figs. 4.7A and 4.7B. Positive Δ*i* have previously been observed in resistive-pulse experiments, and the increase in current during the translocation event was attributed to the charge on the particle itself[16a] and the motion of the counterions.[16b] In the present case of antibody detection, the change in direction of the current pulse and the change in voltage sign when antibody is bound to the particle is an analytical advantage, and the AuNPs with bound IgY should be readily distinguishable from those without IgY. These major differences between current pulses produced by antibody-conjugated particles and either bare Au or Au-peptide nanoparticles confirmed the feasibility of selective resistive-pulse sensing of antibodies with nanopipettes. Importantly, the recordings obtained with AuNP-peptide showed no current pulses at negative

applied voltages (trace III in Fig. 4.7B), indicating that the spikes in Fig. 4.9 can only be attributed to AuNP-peptide-IgY.

Shapes of current pulses. Representative current pulses obtained with different types of particles are shown in Fig. 4.10. Asymmetrical spikes with the sharp initial decrease in current followed by a slow relaxation ("tail") were most often observed with both AuNP-peptide (Fig. 4.10A) and Au-MHDA (Fig. 4.10B). The pipette resistance, which is largely determined by that of its tapered narrow shaft, increases sharply when the particle enters the pipette and then decreases slowly. This kind of pulses were previously shown to give good fits to simulated data[28] and approximate theory developed for electrophoretic transport in the nanopores.[29] Using an approximate model for a nanopipette (see section 4.5 model), a good fit between the theory and the experimental pulses was obtained in Fig. 4.10B with a single adjustable parameter, effective mobility (μ). Notice however that $\mu = 1.8\times10^{-10}\ m^2V^{-1}s^{-1}$ obtained from the fit is at least an order of magnitude lower than the electrophoretic mobilities measured previously for similarly sized particles. This would be consistent with an extremely low value of ζ-potential (<1 mV). This finding points to the significant effect of the electroosmotic flow, whose direction is opposite to that of the electrophoresis, resulting in the diminished value of the effective mobility.[32]

Bipolar pulses with a larger magnitude negative peak ($\Delta i < 0$) and a small positive spike (Fig. 4.10C) were also observed with both AuNP and AuNP-peptide. Such pulses previously reported in the literature, have been recently simulated for the nanopore translocation.[33] The peak width of positive ($\Delta i > 0$) pulses obtained with AuNP-peptide-IgY varied from relatively short (~1 ms) to quite long (~10 ms; Fig. 4.10D), which may be due to the combination of the slow electroosmotic flow and stronger interactions of IgY-modified particles with the pipette

wall. Our understanding of the conductivity enhancement mechanism is incomplete because of the complicated structure of AuNP-peptide-IgY and difficulties in describing its interactions with the nanopipette surface. A more sophisticated model is needed for quantitative analysis of the pulse shape in this case.

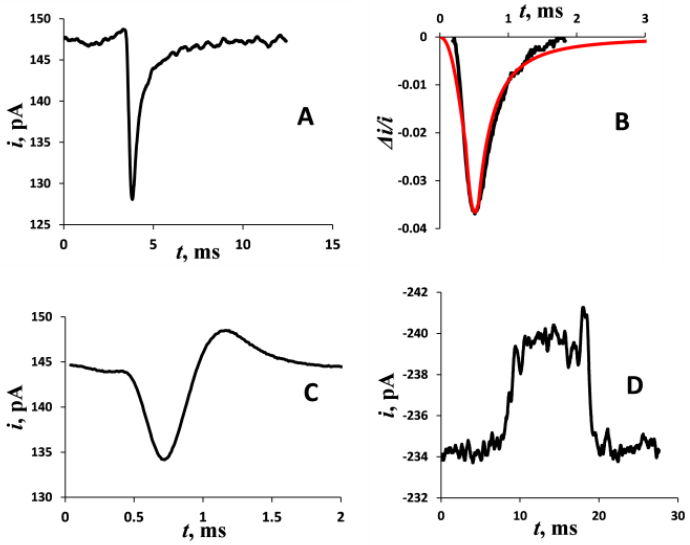

Figure 4.10. Current pulses obtained in solutions containing (A,C) AuNP-peptide, (B) Au-MHDA, and (D) AuNP-peptide-IgY. (B) Experimental (black) and theoretical (red) current-time pulses for the translocation of a Au-MHDA through a 34-nm-diameter pipette.

4.3. Experimental

Chemicals and Materials. The following chemicals were used as received: sodium chloride, 1,2-dichloroethane (DCE), N-hydroxysuccinimide (NHS), mercaptohexadecanoic acid (16-MHDA), 1-(3-(dimethylamino)-propyl)-3-ethylcarbodiimide hydrochloride (EDC), and sodium tetraphenylborate (NaTPB) from Sigma-Aldrich; monosodium phosphate and disodium phosphate from J.T. Baker Chemical; tetrahexylammonium chloride (THACl) and tetrabutylammonium perchlorate ($TBAClO_4$) from Fluka. Tetrahexylammonium tetraphenylborate (THATPB) was prepared by metathesis of NaTPB with THACl and

recrystallized from acetone. Aqueous solutions were prepared from deionized water (Milli-Q, Millipore Co.). 10 mM sodium phosphate buffer (PB) solution at pH 7.0 either with or without 1.8 mg/mL Tween-20 was prepared and used for surface modification of gold colloids.

Citrate-stabilized, 10-nm diameter (as specified by the vendor) Au nanoparticles (5.7×10^{12} particles/mL, i.e., ~9.5 nM) were purchased from Ted-Pella Inc. The stock solution was diluted to the desired concentration in 15 mM NaCl + 10 mM PB. Affinity-purified chicken antipeanut antibodies (IgY) were from Immunology Consultants Laboratory Inc. Peptide fragment of Ara h 2-2 (H_2N-QSPSYPDREYSDEDRQIKQMLHQECPRL-$CONH_2$) was synthesized by Anaspec Inc.

Preparation of gold AuNPs modified with 16-MHDA (AuNP-MHDA). Gold colloids were modified with 16-MHDA according to previously reported procedures.[35] Briefly, 1400 μL of 10 nM gold colloid (Ted-Pella Inc) was centrifuged at 13000 rpm for 90 min. The resultant gold colloid pellet was then reconstituted in 400 μL of deionized water. Equal volume of 10 mM pH 7.0 PB with Tween-20 (PB-T) was added to the AuNP solution and allowed to incubate for 30 min. Then, 400 μL of degassed 0.5 mM ethanol solution of 16-MHDA was added and allowed to incubate for 3 hrs. Next, the nanoparticle solution was centrifuged for 2 hrs at 13000 rpm. The resultant pellet was then washed with PB-T four times, reconstituted in 400 μL of PB-T, and stored at 4 ºC. The prepared stock solution concentration was 22 nM, as determined by UV-Vis spectroscopy (not shown).

Surface conjugation of Ara h 2-2 peptide to AuNP-MHDA. A peptide sequence with active amine functional group was conjugated to carboxylated gold nanoparticles by EDC/NHS amine coupling.[36] Briefly, 200 μL of AuNP-MHDA solution was centrifuged at 13000 rpm for 25 min, the resultant nanoparticle pellet was reacted with 100 mM and 50 mM EDC/NHS in 10

mM pH 7.0 PB for 10 min to activate carboxyl groups on AuNPs. After the activation, the particles were washed with PB twice, and 360 μL of PB and 40 μL of 0.5 mg/mL Arah 2-2 peptide was added to the washed pellet and incubated for 30 min. Centrifugation and washing steps were performed thrice to remove any unbound peptide, and AuNP-peptide conjugate was subsequently reconstituted in 200 μL of PB. The stock solution produced in this way contained 22 nM AuNP-peptide.

IgY capture by AuNP-peptide. Different concentrations of IgY were allowed to react with AuNP-peptide conjugate to form AuNP-peptide-IgY. Typically, 200 μL of AuNP-peptide in 520 μL of PB was allowed to react with 80 μL of 1 ng/mL IgY in PB for 60 min in a small centrifuge tube using a mixer. For TEM, 100 ng/mL IgY was used. The obtained AuNP-peptide-IgY were then separated by centrifugation at 13000 rpm for 2 min and washed with PB.

Characterization of Transferrable Particles. Transmission electron microscopy (TEM) was used to characterize the size distribution of particles. TEM was performed with Tecnai TEM at 80 kV accelerating voltage (340,000× magnification). The TEM grids were glow discharged in plasma cleaner (model PDC-32G, from Harrick Plasma) prior to mounting samples on the carbon type-A grid (Ted Pella, Inc). Glow discharge treatment of TEM grids with air removes adsorbed hydrocarbons and makes a TEM grid carbon film surface negatively charged (hydrophilic), which allows aqueous solutions to spread easily. Samples (3 μL) were placed on carbon grids and dried under air for a 30 min. The samples were Au colloids (2x diluted, pH 7.0), MHDH AuNP (10x diluted, pH 7), Au –Peptide (3.5x diluted, borate buffer pH 9.5), Au-Peptide-IGY (100 ng/mL) (borate buffer pH 9.5). The sample grids were washed several times with deionized water to wash off the buffer. To negatively stain peptides and proteins, 0.5%

phosphotungstic acid was added on the Au-peptide and Au-Peptide-IGY sample grids and allowed to adsorb for 1 min., followed by several washings to wash off unadsorbed stain.

The stability and modification of gold nanoparticles were monitored using zeta potential analysis. Zeta potential measurements of modified Au nanoparticles were performed using ZetaPlus Zeta potential analyzer (Brookhaven Instruments Corporation, Holtsville, NY). The reported zeta potential values were obtained by averaging 5 readings.

Nanopipette Preparation and Voltammetry at the ITIES. Borosilicate or quartz capillaries (o.d./i.d. ratio of 1.0/0.58 and 1.0/0.70, respectively; Sutter Instrument Co., Novato, CA) were cleaned in piranha solution (3:1 H_2SO_4/H_2O_2, v/v; CAUTION! THIS SOLUTION IS A VERY STRONG OXIDIZING AGENT AND VERY DANGEROUS TO HANDLE IN THE LABORATORY. PROTECTIVE EQUIPMENT INCLUDING GLOVES, GOGGLES, AND FACE SHIELDS SHOUD BE USED AT ALL TIMES), rinsed with copious amount of deionized water and kept in furnace overnight. Nanopipettes were fabricated by pulling cleaned capillaries with a laser-based pipette puller (P-2000, Sutter Instrument Co.).[18a,20] Representative pulling parameters for pulling quartz capillaries are HEAT = 760, FILAMENT = 4, VELOCITY = 29, DELAY = 140, PULL = 168.

The pulled pipettes were backfilled with aqueous solution containing 10 mM PB and 15 mM NaCl using a 10 μL syringe and immersed in 1,2-dichloroethane (DCE) solution containing 1 mM $TBAClO_4$. A 0.25 mm silver wire coated with AgCl was inserted into each pipette from the back. A two-electrode setup was employed with another 0.25 mm Ag wire serving as an organic reference electrode. Steady-state voltammograms were obtained using a BAS 100B/W electrochemical workstation (Bioanalytical Systems, West Lafayette, IN).

Resistive-pulse experiments. The pipette filled with 15 mM NaCl and 10 mM PB was dipped into the same aqueous solution containing nanoparticles of interest. A Multiclamp 700B amplifier (Molecular Devices Corporation, CA) was used in the voltage-clamp mode to apply voltage between the Ag/AgCl reference electrode inside the nanopipette and the external Ag/AgCl reference facing the pipette orifice and to measure the resulting current. The signal was digitized using a Digidata 1440A analog-to-digital converter (Molecular Devices) at a sampling frequency of 100 kHz. A low pass filter with 1 - 10 kHz bandwidth was used. The recordings with higher filter frequency, e.g., 20 kHz, as well as with no filtering were obtained in control experiments to verify that shorter current pulses have not been missed or filtered out. The data were recorded and analyzed using pClamp 10 (Molecular Devices).

4.4 Conclusions

We developed nanometer-sized pipettes as a platform for resistive-pulse sensing. Thorough characterization of the pipette size and geometry helps establish the relationship between the particle size and the expected pulse magnitude for a given pipette. The correspondence between frequency of the recorded single particle events and the diffusion current of particles to the orifice suggests the possibility of quantitative determination of analyte species in solution.

The new nanopipette-based approach was used for label-free detection of peptide-modified particles and antibodies attached to them. The possibility of probing mixtures of differently sized analytes was also revealed. The current pulses produced by antibody-conjugated particles and either bare Au or Au-peptide nanoparticles occurred at different translocation voltages (positive for AuNP and AuNP-peptide vs. negative for AuNP-peptide-IgY) and exhibited opposite signs of Δi. These major differences are essential for selective resistive-pulse sensing of antibodies with nanopipettes. If this behavior is common to other protein-modified

nanoparticles, the developed sensing platform can be useful for detecting other types of antibodies and protein biomarkers.

In most reported resistive-pulse experiments, selective detection of biomolecules was achieved by functionalizing the nanopore (e.g., by immobilizing antibodies on its surface[23]). In our study, the analyte (IgY) was selectively captured offline using peptide modified gold nanoparticles. After the analyte capture, the particles can be washed to remove potential interferences and avoid complex mixtures.[34] In this way, selective resistive-pulse sensing of biomolecules can be attained using simple glass or quartz pipettes without laborious surface modification procedures. This approach can also help to avoid other experimental issues that hinder resistive-pulse sensing in biological media, such as clogging and non-specific adsorption of proteins.

4.5 Model

A model originally developed for conically shaped synthetic nanopores[37] was modified to calculate the change in resistance during the translocation of a particle through a nanopipette orifice.

Calculation of effective length of a nanopipette

For a nanopore, the radii of the two openings have been used to define the geometry, while for a nanopipette, the angle θ is observable rather than the second radius, as shown in Fig. 4.11.

The total resistance of the inner solution can be evaluated for the total length L (the distance between the pipette opening and the reference electrode inserted into the pipette), $L>>a$:

$$R_{\text{int}} = \int_0^L \frac{1}{\kappa} \frac{dx}{\pi(a + x\tan\theta)^2} = \frac{L}{\pi\kappa a(a + L\tan\theta)} \approx \frac{1}{\pi\kappa a \tan\theta} \tag{4.4}$$

The solution resistance within the length l from the orifice can also be evaluated as

$$R_l = \frac{l}{\pi\kappa a\left(a + l\tan\theta\right)} \tag{4.5}$$

or in the dimensionless form

$$\frac{R_l}{R_{\text{int}}} = \frac{\frac{l}{a}\tan\theta}{1 + \frac{l}{a}\tan\theta} \tag{4.6}$$

The plot of R_l/R_{int} versus normalized length (l/a) is shown in Fig.4.12. The effective length l_{eff} of a nanopipette can be defined as the length of its tapered shaft adjacent to the tip that produces most (e.g., 90%) of the resistance. It shows that l_{eff} depends strongly on pipette angle.

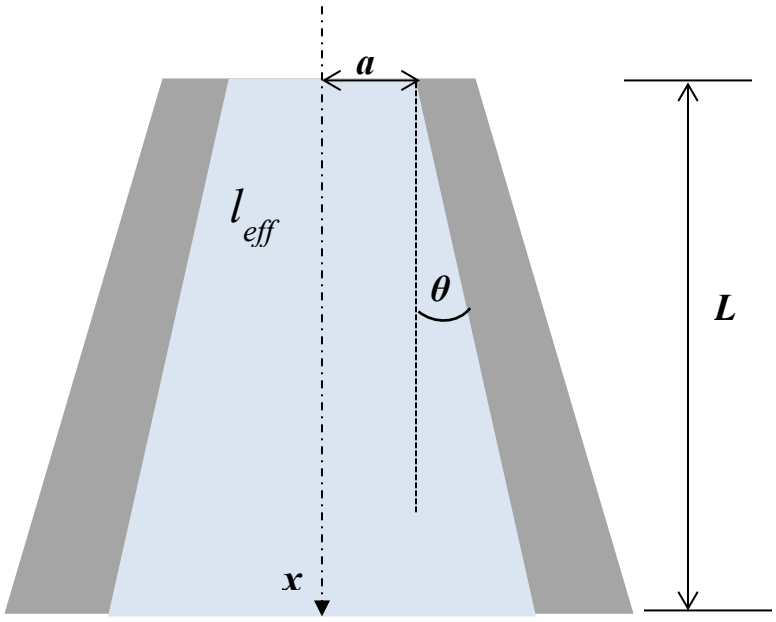

Figure 4.11. Schematic representation of a nanopipette.

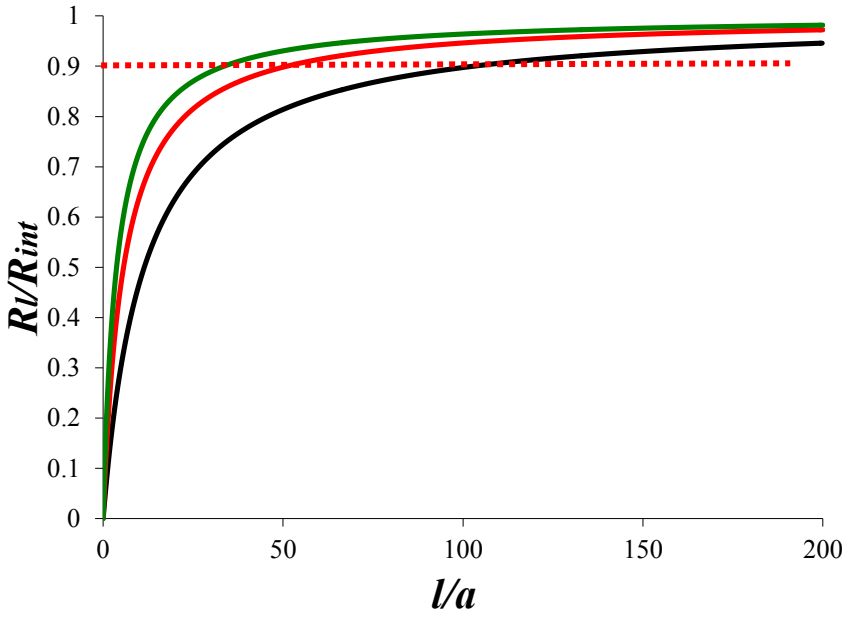

Figure 4.12. Resistance profile inside a solution-filled conical pipette as a function of pipette angle. θ = 15° (green), 10° (red), and 5° (black).

Calculating the current change caused by the translocation of a spherical particle through the pipette tip. The total pipette resistance comprises two components, i.e., the resistances of the internal and external solutions:

$$R = R_{\text{int}} + R_{ext} \tag{4.7}$$

The resistance of external solution is[38]

$$R_{ext} = \frac{1}{4\kappa a} \tag{4.8}$$

As a particle enters the pipette, the displacement of the electrolyte solution from the narrow shaft results in the increase in resistance of inner solution (the effect on resistance of outer solution is negligible). Two stages of the translocation process are shown in Fig.4.13. The change in resistance occurs within the layer of solution containing the particle (or its part that has

already entered the pipette). The resistance of this layer, R_{par}, can be calculated and then compared to its original resistance, R_{ori}, to find the change caused by the particle penetration.

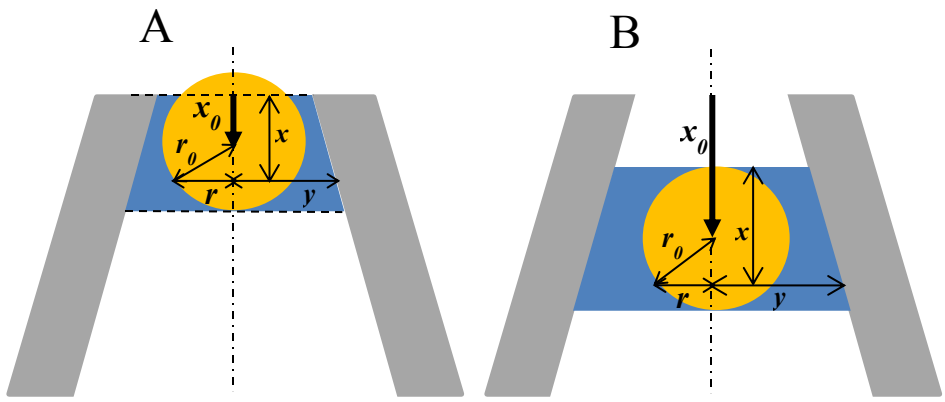

Figure 4.13. Schematics of the translocation process. (A) The particle is entering the pipette. The penetration depth, x_0 (i.e., the coordinate of the center of the particle with respect to the orifice) is within the range $-r_0 \le x_0 \le r_0$, where r_0 is the particle radius. (B) The particle is entirely inside the pipette;

$$x_0 \ge r_0$$

To calculate R_{par} for the first stage (partial penetration; Fig. S3A), consider a donut-shaped layer of the thickness *dx* at a distance *x* from the orifice, $0 \le x \le x_0 + r_0$. The outer radius of the donut, *y* is:

$$y = a + x\tan\theta \tag{4.9}$$

The resistance of the layer of solution containing the particle (blue layer in Fig. 4.13) is

$$R_{par} = \int_0^{x_0+r_0} \frac{1}{\kappa}\frac{dx}{\pi\left(y^2 - r^2\right)} \tag{4.10}$$

where *r* is the inner radius of the donut defined as

$$r^2 = r_0^2 - \left(x - x_0\right)^2 \tag{4.11}$$

After the integration, Eq. 4.10 yields

$$R_{par} = \frac{1}{\kappa\pi}\frac{2}{\sqrt{4AC-B^2}}\left\{\arctan\left[\frac{2A(x_0+r_0)+B}{\sqrt{4AC-B^2}}\right]-\arctan\left(\frac{B}{\sqrt{4AC-B^2}}\right)\right\} \tag{4.12}$$

where

$$A = \tan^2\theta + 1 \tag{4.13}$$

$$B = 2(a\tan\theta - x_0) \tag{4.14}$$

$$C = a^2 + x_0^2 - r_0^2 \tag{4.15}$$

The resistance of the same layer without a particle was:

$$R_{ori} = \frac{x_0 + r_0}{\pi\kappa a[a + (x_0 + r_0)\tan\theta]} \tag{4.16}$$

and the change in resistance is:

$$\Delta R = R_{par} - R_{ori} \tag{4.17}$$

For the complete particle penetration (Fig. 4.13B), $0 \le x \le 2r_0$ and other variables are

$$y = a + (x_0 - r_0 + x)\tan\theta \tag{4.18}$$

$$r^2 = r_0^2 - (r_0 - x)^2 \tag{4.19}$$

$$R_{par} = \int_0^{2r_0}\frac{1}{\kappa}\frac{dx}{\pi(y^2 - r^2)}$$

$$= \frac{1}{\kappa\pi}\frac{2}{\sqrt{4AC-B^2}}\left[\arctan\left(\frac{4Ar_0+B}{\sqrt{4AC-B^2}}\right)-\arctan\left(\frac{B}{\sqrt{4AC-B^2}}\right)\right] \tag{4.20}$$

$$A = \tan^2\theta + 1 \tag{4.21}$$

$$B = 2[\tan^2\theta(x_0 - r_0) + a\tan\theta - r_0] \tag{4.22}$$

$$C = [a + \tan\theta(x_0 - r_0)]^2 \tag{4.23}$$

The original resistance of the layer, which now contains the particle, was:

$$R_{ori} = \frac{2r_0}{\pi\kappa\left[a + (x_0 - r_0)\tan\theta\right]\left[a + (x_0 + r_0)\tan\theta\right]} \tag{4.24}$$

For both steps, the current change can be calculated as

$$\Delta i / i = \left[1/R - 1/(R + \Delta R)\right]/(1/R) = \Delta R/(R + \Delta R) \tag{4.25}$$

Eq. 4.25 was used to calculate the effects of the pipette radius and angle (Fig. 4.6A and 4.6B in the main text).

Fitting experimental current pulses to the theory Consider a one-dimensional motion (along the *x* axis) of a particle entering the pipette so that the particle center moves through the center of the orifice. We calculate a theoretical *i* vs *t* curve assuming that the transport inside the pipette is dominated by electrophoresis. The steady-state electrophoretic velocity of a particle in the electric field *E* is:[39]

$$u = \mu E \tag{4.26}$$

where μ is the mobility of the particle. The field, *E*, can be evaluated from the potential profile near the pipette orifice. If V_0 is the voltage applied between the internal and external reference electrodes, the potential at a certain point outside the pipette ($x_0 < 0$; $x_0 = 0$ corresponds to the orifice) can be calculated by Newman's model as following:[40]

$$V_{ext} = V_0 \times \frac{R_{ext}}{R} \times \left[1 - \frac{2}{\pi}\tan^{-1}\left(\frac{-x_0}{a}\right)\right] \tag{4.27}$$

Eq. (4.27) is an approximation because in Newman's model the potential is uniform over the disk surface (i.e., the pipette orifice in our model). However, the differences between the results obtained using Eq. (4.27) and those simulated using COMSOL Multiphysics were relatively small.

For a point inside the pipette ($x_0 > 0$), the voltage drop can be evaluated as

$$V_{\text{int}} = V_0 \times \frac{R_{ext} + R_{x_0}}{R} \tag{4.28}$$

where R_{x_0} is the resistance of the electrolyte solution between the orifice and the point x_0, R is the total resistance from Eq. 4.7 and R_{ext} is the external resistance from Eq. 4.8.

$$R_{x_0} = \frac{x_0}{\pi\kappa a\left(a + x_0 \tan\theta\right)} \tag{4.29}$$

Combining Eq. 4.28 with Eqs. 4.4, 4.7, 4.8 and 4.29, one obtains:

$$V_{\text{int}} = V_0 \times \frac{\frac{\pi}{4} + \frac{x_0}{a + x_0 \tan\theta}}{\frac{1}{\tan\theta} + \frac{\pi}{4}} \tag{4.30}$$

The local electric field is:

$$E_{ext} = \frac{dV_{ext}}{dx_0} = \frac{V_0}{\frac{1}{\tan\theta} + \frac{\pi}{4}} \times \frac{1}{2a\left[1 + \left(x_0 / a\right)^2\right]} \tag{4.31}$$

or

$$E_{\text{int}} = \frac{dV_{\text{int}}}{dx_0} = \frac{V_0}{\frac{1}{\tan\theta} + \frac{\pi}{4}} \times \frac{1}{a\left[1 + \left(x_0 / a\right)\tan\theta\right]^2} \tag{4.32}$$

Therefore, the local velocity is

$$u_{ext} = \mu \times \frac{V_0}{\frac{1}{\tan\theta} + \frac{\pi}{4}} \times \frac{1}{2a\left[1 + \left(x_0 / a\right)^2\right]} \tag{4.33}$$

or

$$u_{\text{int}} = \mu \times \frac{V_0}{\frac{1}{\tan\theta} + \frac{\pi}{4}} \times \frac{1}{a\left[1 + \left(x_0 / a\right)\tan\theta\right]^2} \tag{4.34}$$

The time, t, required for the travel between the point $-r_0$ (where the front edge of the particle touches the pipette orifice) and a point x_0 in the external solution is

$$t_{ext} = \int_{-r_0}^{x_0} \frac{dx_0}{u_{ext}} = \frac{1}{\mu} \frac{\frac{1}{\tan\theta} + \frac{\pi}{4}}{V_0} \times 2a^2 \left\{ \frac{x_0}{a} + \frac{r_0}{a} + \frac{1}{3}\left[(\frac{x_0}{a})^3 + (\frac{r_0}{a})^3 \right] \right\} \tag{4.35}$$

If the point x_0 is inside the pipette, the corresponding time is

$$t_{\text{int}} = t_0 + \int_0^{x_0} \frac{dx_0}{u_{\text{int}}} = t_0 + \frac{1}{\mu} \frac{\frac{1}{\tan\theta} + \frac{\pi}{4}}{V_0} \times \frac{(a + x_0 \tan\theta)^3 - a^3}{3a \tan\theta} \tag{4.36}$$

while t_0 is the time spent between $-r_0$ to 0.

Using Eqs. 4.35 and 4.36, the current vs. position plots (e.g., Figs 4.6A and 4.6B) can be converted to the current vs time dependence. An example of fitting an experimental pulse to the theoretical i vs. t curve is shown in Fig. 4.10B. If the electroosmotic flow is significant and opposite to the electrophoretic direction, the effective mobility value extracted from the fit should be approximately equal to the difference of the electrophoretic and electroosmotic mobilities.[41]

Chapter V

Nanoelectrodes for Determination of Reactive Oxygen and Nitrogen Species inside Murine Macrophages

5.1 Introduction

Macrophage cells are essential for the performance of the immune system. Their activation, either under normal biological conditions or by specific biochemical activators *in vitro*, results in the production of reactive oxygen and nitrogen species (ROS and RNS) and creation of a large number of vacuoles (phagosomes and phagolysosomes, see Fig. 5.1).[1-3] These vacuoles play an important role in phagocytosis—a mechanism used by the immune system to remove pathogens and cell debris. A cell (or debris) is engulfed into a vacuole and subjected to an intense oxidative burst,[2] and the indigestible debris and excess ROS and RNS are subsequently evacuated from the macrophage (Fig. 5.1B).

The changes in oxygen and hydrogen peroxide concentrations during the oxidative burst of a stimulated macrophage cell were detected previously using the scanning electrochemical microscope.[4] Extensive studies with amperometric microelectrodes positioned in the cell proximity showed that the basal release is due to a cocktail composed of several ROS and RNS evolving from the primary production of $O_2^{\bullet-}$ and NO.[5-8] However, the concept that ROS and RNS released inside phagolysosomes may diffuse across the vacuole membrane and leak in the cell cytoplasm remains controversial.[9-12] In fact, NO and the trans-isomer of protonated peroxynitrite ion are capable of crossing biological membranes due to their lipoliphicity.[13,14] This underscores the importance of probing for the intracellular presence of ROS and RNS in activated macrophages.

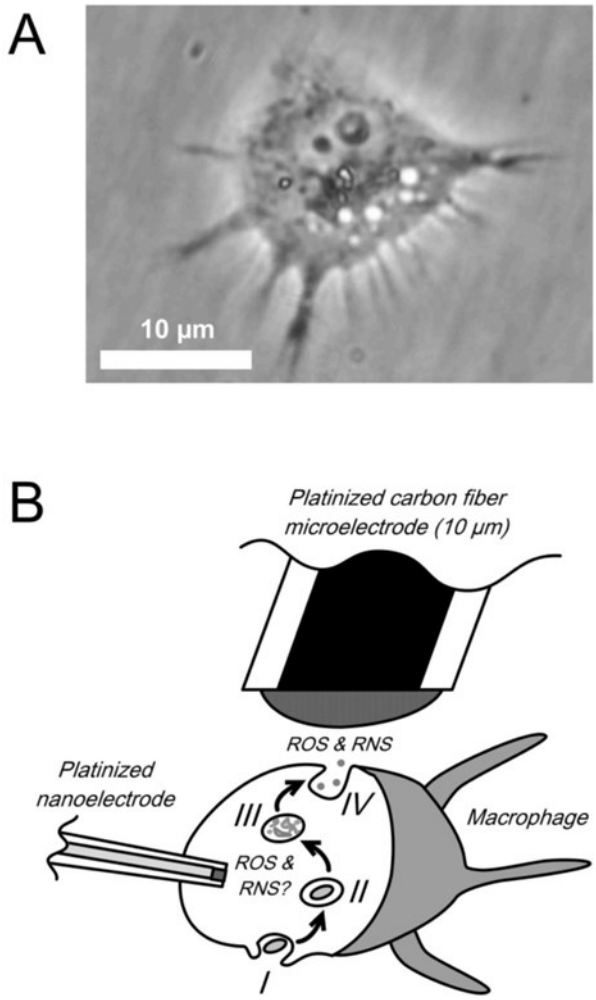

Figure 5.1. Optical micrograph of a macrophage RAW 264.7 activated by interferon-γ and LPS evidencing the presence of phagolysosomes (white spots) (A) and schematic representation of an activated macrophage undergoing phagocytosis (B). I: capture of a cell or debris; II: internalization within phagosome; III: digestion by ROS/RNS within phagolysosomes; IV: expulsion of indigestible material and excess of ROS/RNS. Also shown in B are two configurations used for the detection of ROS/RNS by either a platinized nanoelectrode inside or a microelectrode outside the cell, as discussed in the text.

For electrochemical measurements inside an activated macrophage one needs nanometer-sized electrodes that can be inserted into a living cell without causing irreparable damage to its membrane. Also, the cell membrane must seal around the nanoelectrode to preserve as much as possible the integrity of intracellular mechanisms and prevent any direct liquid junction between extra- and intracellular compartments. Previously, quantitative electrochemical experiments were performed by inserting glass-sealed, polished Pt nanoelectrodes into cultured human breast cells.[15] The cell membrane formed a tight seal around the penetrating nanotip that prevented the external solution from leaking inside the cell. This allowed the cell to remain alive for the entire time of experiment (>10 min) with a nanoelectrode inside it. However, a polished Pt nanoelectrode is not suitable for the detection of ROS and RNS, which passivate its small surface and diminish the signal. Even micrometer-sized probes used for extracellular measurements of

ROS and RNS had to be coated with Pt black to improve the stability of the response.[16] Several approaches to fabricating micrometer and submicrometer-sized Pt electrodes with high surface area are available in the literature.[16-19] For quantitative intracellular measurements, platinized probes have to be smaller (<1 μm total diameter, including glass sheath), with porous Pt surface flush with the surrounding insulator.

The methodology for fabricating nanoelectrodes by electrodeposition of metals was reported recently.[20] The electrodes were produced by electrodepositing metal into a nanocavity, which was formed by etching away a nm-thick layer of Pt from the glass-sealed, polished Pt nanoelectrode.[21] The amount of deposited metal was controlled by monitoring the charge, and its excess was removed by polishing to yield a flat electrode. This strategy cannot be used to prepare platinized nanoelectrodes because the current efficiency in deposition of Pt black is relatively low and polishing was shown to diminish the electrode response. To overcome these problems, we developed new methodology for fabricating platinized nanoelectrodes under AFM control.

5.2 Results and Discussion

Fabrication of the platinized nanoelectrodes. An early attempt to produce a platinized nanoelectrode by electrodeposition is shown in Fig. 5.2. The black curve in Fig. 5.2A is a voltammogram of ferrocenemethanol (FcMeOH) at a polished Pt electrode with the radius, a = 60 nm calculated from the diffusion limiting current. After etching, the diffusion current decreased to ~50% of the original value (red curve in Fig. 5.2A), which corresponds to the formation of a ~40-nm-deep cavity, according to the available theory.[21] After the platinization, the FcMeOH current increased almost ten times (green curve) indicating that the nanopore was significantly overfilled with Pt black. Most excess Pt black was removed by polishing, after

which the limiting current (blue curve in Fig. 5.2A) was only slightly higher than that obtained at the original polished electrode (black curve) in accordance with an SEM image (Fig. 5.2B) showing the electrode radius of ~80 nm.

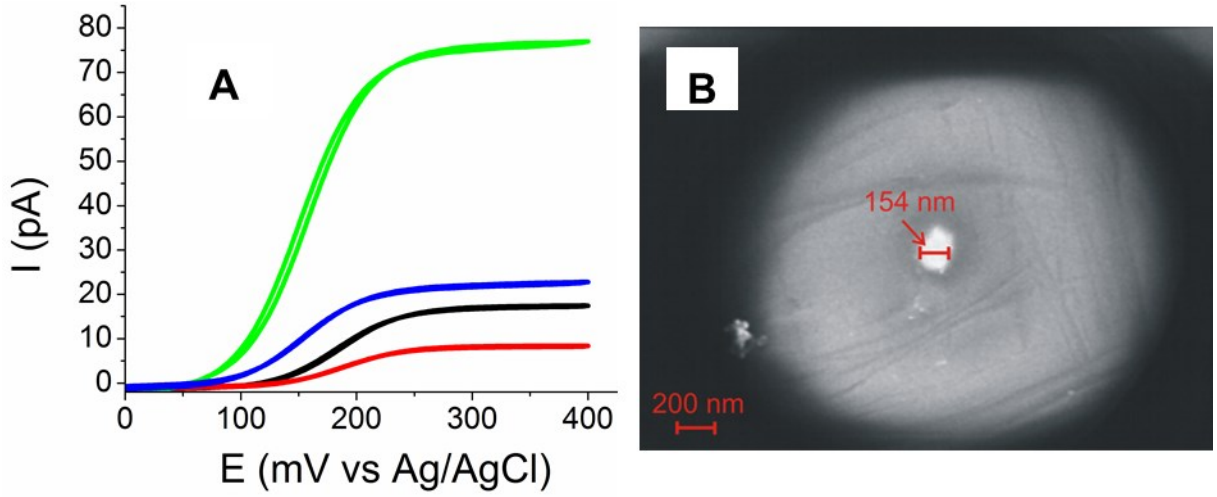

Figure 5.2. (A) Cyclic voltammograms of 1 mM FcMeOH in 0.1 M KCl obtained at a 60-nm-radius polished Pt electrode before etching (black), after etching (red), after platinization at -100 mV vs. Ag/AgCl (green), and after removing excess Pt black by polishing (blue). (B) SEM image of the same electrode after platinization and polishing.

While seemingly successful, the above example shows major difficulties in platinization of nanoelectrodes. With no efficient control, large excess of Pt black was deposited. Although it could be removed, as shown in Fig. 5.2, polished platinized electrodes typically exhibit very low responses to ROS/RNS. Finally, SEM imaging is not a convenient technique for monitoring the fabrication. It cannot be done *in-situ*; has low z-axis resolution, which does not allow one to see whether the Pt electrode is recessed, flat, or protruding; and the imaged electrodes are no longer suitable for electrochemical experiments.

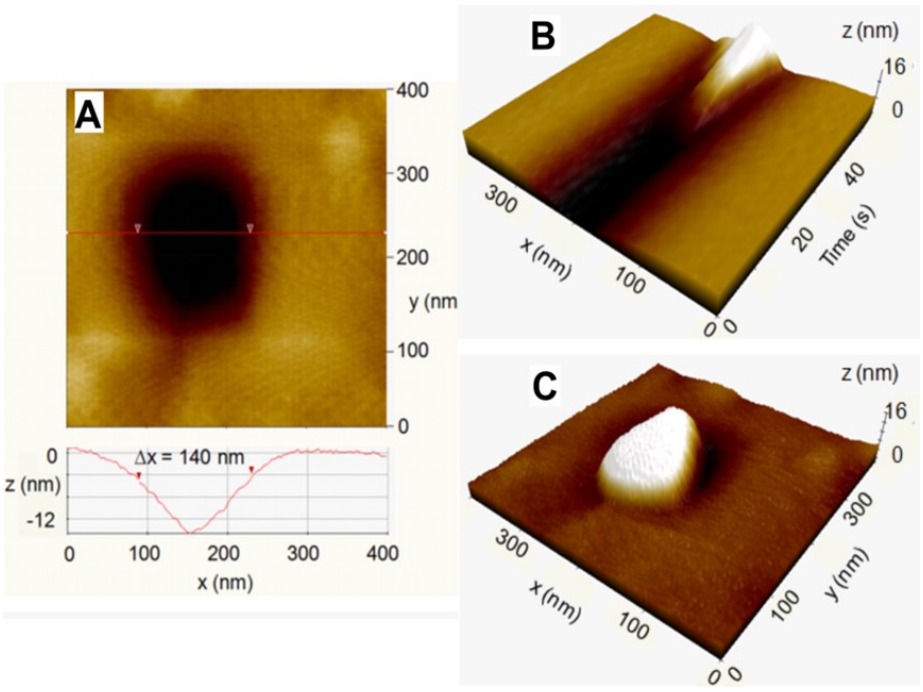

Figure 5.3. Non-contact topographic images of an etched Pt nanoelectrode in solution before (A) and after (C) the deposition of Pt black, and time evolution of a line scan during the electrodeposition process (B). The red line in A corresponds to the shown cross-section. (B) The tip was scanned along the x-axis with the scan rate of 1 Hz. The position of the line scan approximately corresponded to the red line in A.

An alternative approach—electrodeposition of Pt black under the AFM control—is illustrated in Fig. 5.3. A non-contact topographic image of an etched Pt electrode (Fig. 5.3A) in solution before the platinization shows the effective radius, $a \approx 70$ nm and the cavity depth of ≥20 nm (The triangular shape of the cross-section in Fig. 5.3A suggests that the tip did not reach the bottom of the cavity, and the actual depth could be larger). The deposition of Pt black was done by stepping the electrode potential to -100 mV versus Ag/AgCl, while the AFM tip, immersed in the platinization solution, was scanned in x-direction above the electrode surface. Fig. 5.3B shows a stack of 60 consecutive topographic 1D scans obtained over a 60 s period. Initially, the deposition process was slow, and its rate increased with time, as the cavity depth decreased. The deposition was stopped by stepping the electrode potential to 0 mV after Pt black

completely filled the cavity and slightly protruded (by ~15 nm) from the glass sheath, as can be seen from the image of the same electrode obtained after the platinization (Fig. 5.3C). In another deposition experiment (Fig. 5.4), the initial depth of the nanocavity was only ~2 nm and the protrusion height after the deposition of Pt black was ~3 nm.

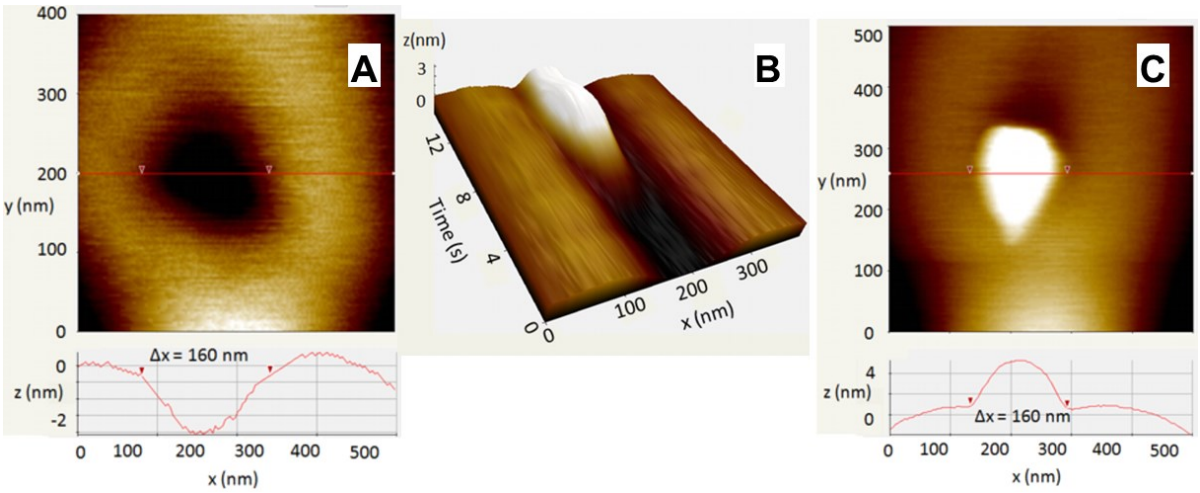

Figure 5.4 Non-contact topographic images of a slightly recessed Pt nanoelectrode in solution before (A) and after (C) the deposition of Pt black, and time evolution of a line scan during the electrodeposition process (B). The red lines in A and C correspond to the shown cross-sections. (B) The tip was scanned along the x-axis with the scan rate of 1 Hz. The position of the line scan approximately corresponded to the red line in A.

The above methodology for fabricating Pt black nanoelectrodes, although powerful and reliable, is laborious and requires AFM instrumentation. A simpler approach to platinization makes use of the characteristic shape of the current transient. As noted above, the rate of the deposition process increases greatly when the cavity gets completely filled with metal. The corresponding sharp increase in current can be used to detect the completion of the platinization (Fig. 5.5). The etched electrode (Fig. 5.5A) was imaged in air, and then a current transient (Fig. 5.5B) was obtained in the platinization solution during the Pt black deposition into its cavity. The

sharp increase in the slope of the current-time curve indicated that the nanocavity was filled, as can be seen in the image of the platinized electrode (Fig. 5.5C).

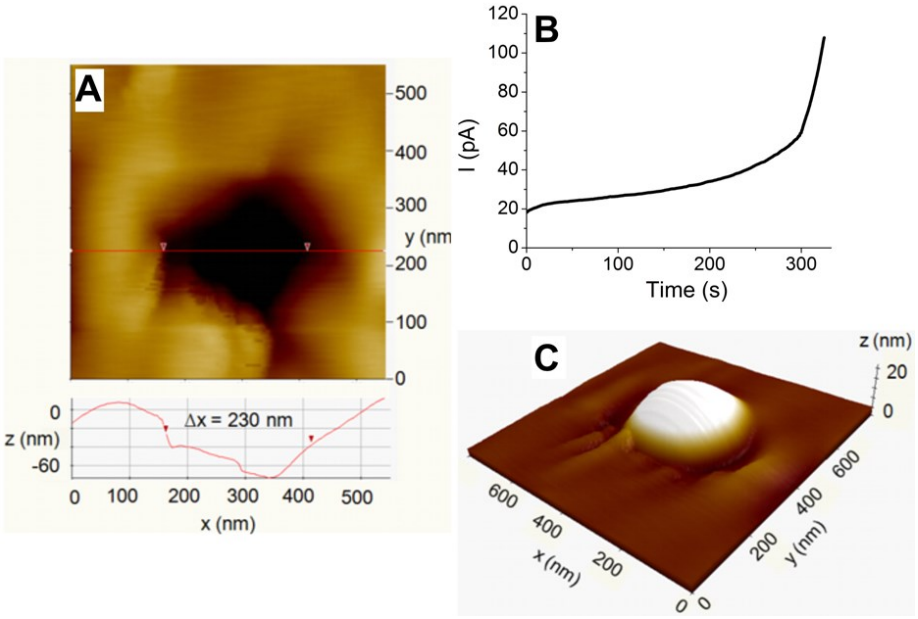

Figure 5.5**.** A non-contact AFM image of a 115-nm-radius etched electrode in air (A), a current transient of the Pt black deposition (B), and a topographic image of the same electrode after platinization (C).

In Vitro Detection of ROS/RNS. The capacity of platinized nanoelectrodes for detecting *in vivo* the four typical electroactive ROS/RNS released by macrophages during oxidative bursts has been evaluated *in vitro* using aerated PBS solutions of hydrogen peroxide (H_2O_2), peroxynitrite anion ($ONOO^-$), nitric oxide (NO) and nitrite anion (NO_2^-) (Fig. 5.6A). NO_2^- and H_2O_2 species are stable at biological pH (7.4). Their voltammograms (red and black curves in Fig. 5.6A) are qualitatively similar to those recorded previously with micrometer-sized electrodes,[6,7] and the calibration curves obtained from the families of such voltammograms (Fig. 5.6B) are linear (Figs. 5.6C and 5.6D). Conversely, $ONOO^-$ is not stable at pH 7.4, and its voltammogram (blue curve in Fig. 5.6A) was obtained at pH 10.[22] Similarly, due to its rapid reaction with O_2, NO was generated in situ by controlled decomposition of DEANONOate (see

experimental section).[23] The instability of these species was not, however, an issue for *in-vivo* experiments where ROS/RNS are produced and detected on a much shorter experimental time scale (seconds).[6-8]

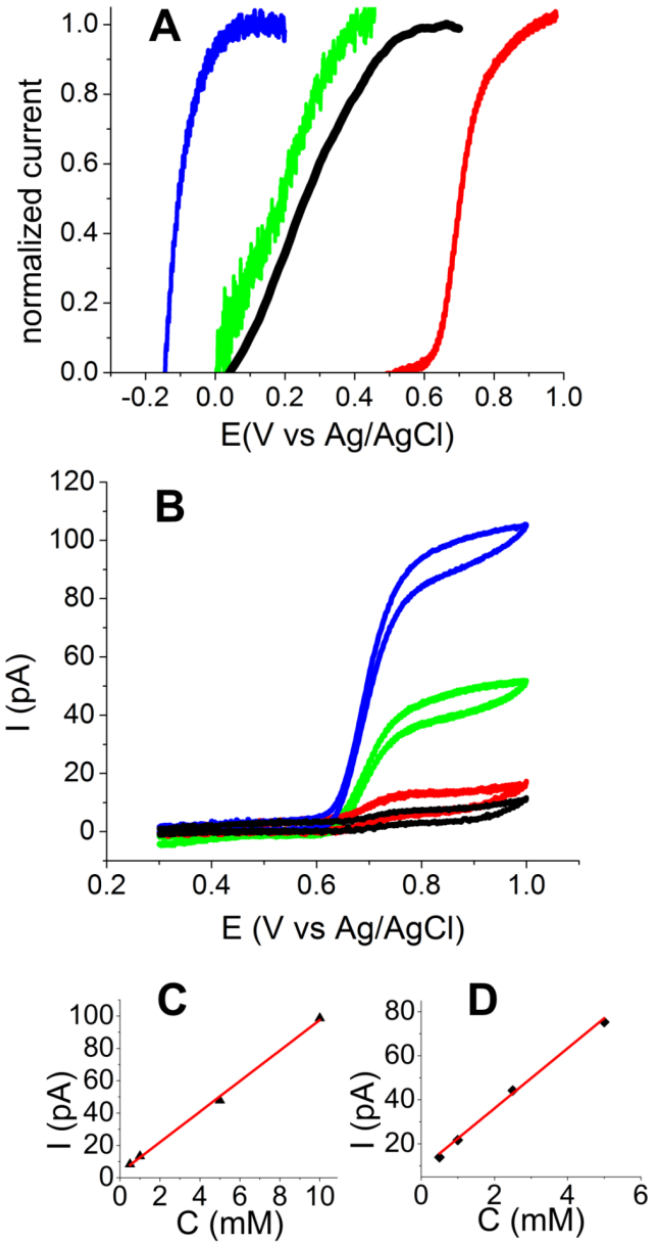

Figure 5.6. *In vitro* voltammetry of ROS/RNS species in aerated PBS. (A) Normalized voltammograms of oxidation of $ONOO^-$ (blue curve; 10 mM, pH 10, see text; the foot of the wave is merged with that of the reduction of dioxygen), NO (green, ~1 mM, see text), H_2O_2 (black; 1mM, pH 7.4), and NO_2^- (red; 5 mM, pH 7.4). Voltammograms were recorded at different platinized nanoelectrodes with the average radius of 60 nm and normalized by their plateau currents. (B) Steady-state voltammograms of NO_2^-, 10 (blue), 5 (green), 1 (red) and 0.5 mM (black) at a platinized nanoelectrode. a = 40 nm. Calibration curves for NO_2^- (C) and H_2O_2 (D) obtained from diffusion limiting currents of steady-state voltammograms.

The importance of platinization is illustrated by Fig. 5.7 showing the voltammograms of NO_2^- oxidation at the same 65 nm Pt electrode before etching (black curve) and after the deposition of Pt black (red curve). Clearly, only platinized nanoelectrodes exhibit analytically useful response to ROS/RNS. The similarity of voltammograms obtained for FcMeOH oxidation (Fig. 5.2 A) and

$Ru(NH_3)_6^{3+}$ reduction (Fig. 5.7 A) at the same electrode before etching and after platinization indicates that the greatly enhanced response to NO_2^- after platinization is not due to the larger electrode radius or protrusion, but to electrocatalytic effects.

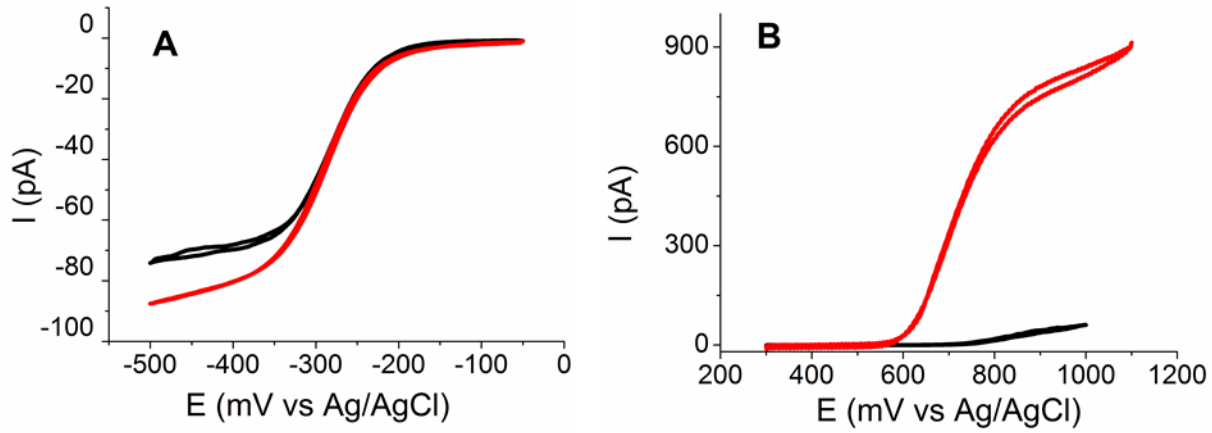

Figure 5.7. Cyclic voltammograms of 5 mM $Ru(NH_3)_6^{3+}$ in 0.1M KCl (A) and 10 mM NO_2^- in pH 7.4 PBS (B) obtained at the same 65-nm-radius Pt electrode after polishing (black curves) and after platinization (red curves). Scan rate was v = 50 mV/s.

In Vivo Detection of ROS/RNS with Platinized Nanoelectrodes. The next step involved the characterization of the global release of the above four ROS/RNS inside activated murine macrophages (RAW 264.7 line). In these experiments, we took advantage of the previous observation that the penetration of the cell membrane by a sub-micrometer tip activates it and induces fast oxidative burst release.[6,7] Hence, a platinized nanoelectrode was inserted inside a macrophage (Fig. 5.8 A) with the purpose of eliciting its response. The intensities of oxidative bursts elicited by the nanoelectrode insertion were monitored outside the macrophage cells with a classical 10 µm platinized fiber electrode (polarized at 850 mV vs. Ag/AgCl) following a previously reported protocol (Fig. 5.8 B).[6,7] The inserted nanoelectrode was also polarized at 850 mV vs. Ag/AgCl and used for monitoring the amount ROS/RNS released intracellularly (Fig. 5.8 C).

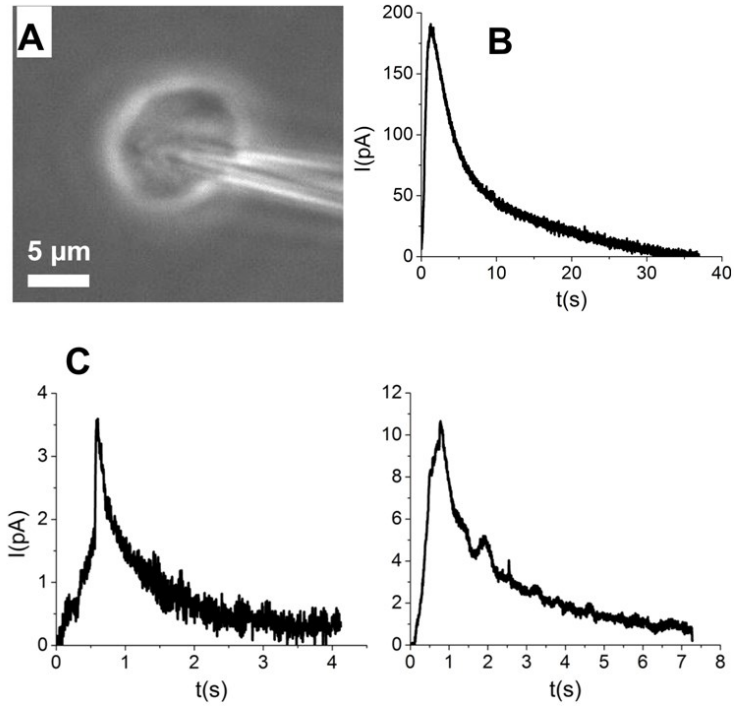

Figure 5.8. Monitoring ROS/RNS release induced by the mechanical stimulation of a macrophage. (A) Optical microscopic micrograph of a nanoelectrode (a = 75 nm; 800 nm O.D.) inside a macrophage. (B) Amperometric detection of ROS/RNS outside the macrophage at the 10 µm platinized carbon fiber electrode polarized at 850 mV vs. Ag/AgCl; the oxidative burst was elicited by the penetration of a platinized nanoelectrode through the macrophage membrane. (C) Two typical amperometric current traces of the ROS/RNS release inside a macrophage induced by the insertion of a platinized nanoelectrode (left: a = 50 nm, 700 nm O.D.; right: a = 40 nm, 900 nm O.D.); E = 850 mV vs. Ag/AgCl.

The comparison of Figures **5.8**B and **5.8**C shows that the responses monitored outside and inside are completely different, the outside response being more intense and lasting longer time (Table **5.**1). It was then essential for us to ensure that the cell membrane formed a tight seal around the nanoelectrode shaft to eliminate a possibility that the response monitored inside the cell resulted from traces of ROS/RNS released outside and leaking into the cell. For this purpose, a series of experiments were performed with macrophages bathed in PBS containing 1 mM $Ru(NH_3)_6Cl_3$ (Fig. **5.9**). The complete absence of the $Ru(NH_3)_6^{3+}$ reduction wave inside the cell, which was observed in ~20% of these experiments, provided evidence for a perfect seal.[15] The

similarity of $Ru(NH_3)_6^{3+}$ voltammograms obtained before (black curve in Fig. **5.9**) and after (green curve) cell penetration indicates that the nanoelectrode capacity to respond to this species has not significantly diminished during the entire experiment. The typical current transients of ROS/RNS shown in Figure **5.8**C were recorded only in cells that have exhibited no solution leakage through the membrane/glass seal.

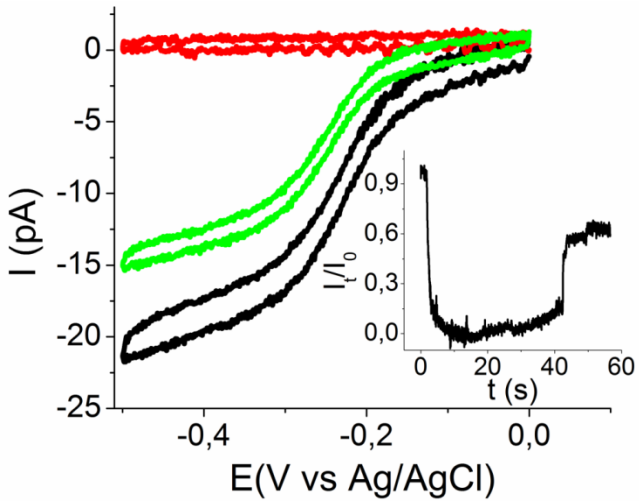

Figure 5.9. Voltammetric reduction of $Ru(NH_3)_6^{3+}$ in solution and inside a macrophage. Voltammograms were obtained before cell penetration (black), inside the cell (red) and after the removal (green) of a platinized nanoelectrode (a = 60 nm) from the cell in a solution of PBS containing 1 mM $Ru(NH_3)_6Cl_3$. The inset shows a current-time trace corresponding to the nanoelectrode insertion into the cell and its subsequent retraction to the external solution; E = -400 mV vs. Ag/AgCl.

Table 5.1. Average parameters of oxidative bursts produced by RAW 264.7 macrophages detected inside or outside the cells by different platinized electrodes.

Detection	**Electrode**	I_{max} **(pA)**	$t_{1/2}$ **(s)**	Q **(pC)**
Intracellular (n = 10)	platinized Pt nanoelectrode	11.7 ± 6.4	0.5 ± 0.1	7.7 ± 3.5
Extracellular (n = 8)	10 µm platinized carbon fiber	86 ± 23	5.8 ± 1.8	703 ± 200

Macrophages were stimulated mechanically by insertion of a platinized nanoelectrode (60 nm average radius). The potential of the detecting electrode was 850 mV vs. Ag/AgCl. All values are reported as a mean ± SEM; n, indicated in parentheses, is the number of experiments of each type (each one involving a different cell and a different electrode).

Relative electroactivity of platinized nanoelectrodes vs. 10µm platinized carbon UMEs. Previously developed methodologies for nanoelectrode fabrication are not suitable for preparing platinized probes. Our new approach based on the *in-situ* AFM control of Pt black deposition was used to produce well-shaped platinized nanoprobes (Figs. 5.3 and 5.4), which exhibited good amperometric responses to ROS and RNS. AFM images also showed the diameter of the insulating glass sheath, which determines the physical size of the probe essential for cell penetration. The response of platinized nanoprobes to ROS and RNS decreases on the time scale of several days; thus it is desirable to prepare new platinized electrodes right before *in-vivo* experiments. To address this need (and also simplify the fabrication), one can detect the end point of Pt black deposition from the current transient instead of using AFM control. Non-contact AFM imaging of the nanoelectrode in air before and after platinization can be used to evaluate its geometry and applicability to intracellular measurements (Fig. 5.5). The latter method is faster and easier than AFM-controlled electrodeposition, but the former approach is more accurate and reliable.

The *in vitro* experiments with ROS/RNS evidenced that the platinized nanoelectrodes yield characteristic steady-state voltammograms for each of the four species composing oxidative bursts. The sensitivity of nanoelectrodes for ROS and RNS (e.g., ~0.2 pA/mM/nm for NO_2^-; a = 60 nm, Fig. 5.6C) was about half that predicted theoretically or monitored for $Ru(NH_3)_6^{3+}$ reduction and FcMeOH oxidation (Figs. 5.2, 5.7A). The same applies when comparing to the initial Pt disk nanoelectrodes (Fig. 5.2A). These relative figures indicate that Pt-black nano-deposits are somewhat less active than expected from their geometrical dimension

presumably because their dendritic growth was constrained by nanometer dimensions of the underlying Pt surface.

The assumption of diffusion controlled ROS/RNS responses for the platinized nanoelectrodes used in this study is validated by the constancy of $i_d/(ca)$, where i_d is the plateau current and c is the bulk concentration; for a given electrode (see calibration curves in Figs. 5.6C and 5.6D). However, $i_d/(ca)$ for ROS/RNS was largely irreproducible and always lower than for $Ru(NH_3)_6^{3+}$ reduction or FcMeOH oxidation which undergo outer-sphere electron transfer processes. Oxidation of ROS/RNS requires the presence of a sufficient density of electrocatalytic sites (compare, for example, the responses before etching, viz. Pt-metal surface, and after platinization, viz. Pt-black, in Fig. 5.7B).

The low measured $i_d/(ca)$ values indicate that only a fraction of the Pt-black dendritic material deposited in the nanocavity was active. This implies that only a fraction of the exposed ends of Pt nanodendrites carried a sufficient density of electroactive sites. Although this hypothesis would be difficult to prove, it is consistent with the stochastic nature of the dendritic nucleation/growth processes. For this reason, only platinized nanoelectrodes that gave plateau currents consistent with their geometrical radii (i.e., $i_d/(ca) \geq 0.1$ pA.mM^{-1}.nm^{-1}) were used in our experiments.

ROS/RNS leakage from phagolysosomes The difference in sensitivity was not critical for our purpose because these electrodes were not used to measure ROS/RNS concentrations, but to collect their fluxes produced either inside (nanoelectrodes) or outside (microelectrodes) stimulated macrophages. The important parameters here are the time durations ($t_{1/2}$) and the integral of the current-time responses (i.e., charge, Q, which reflects the quantity released[6-8]) recorded at the platinized electrode (Table 5.1).

In the absence of solution leakage through the membrane/glass seal, the nanoelectrode insertion into an isolated macrophage elicited a brief current spike and a small amount of charge showing that the collected ROS/RNS flux was of much lower intensity and shorter duration than that detected outside the stimulated cell at the same electrode potential (cf. Figs. 5.8B and 5.8C and Table 5.1). The height of the current peak indicated that the cumulative ROS/RNS concentration released inside the cell peaked at submillimolar values before decaying rapidly.

Because all presented data was obtained with proper sealing of the cell membrane around the nanoelectrode shaft, it is clear that ROS/RNS detected inside the cell represent only species released inside the cell. Moreover, would there be unnoticed leakage from the outside, the kinetic features of the nanoelectrode responses would mimic those recorded outside the cell. On the contrary, two distinct components of the oxidative burst were produced by a mechanically activated macrophage: one small and brief (short $t_{1/2}$ and small Q, Fig. 5.8C, Table 5.1) inside the cell and another one, much longer and with a larger amount of charge—outside (Fig. 5.8B, Table 5.1). This observation is consistent with the view that in response to stimulation a macrophage produces small vacuoles whose membranes are equipped with NADPH-oxidase and NO-synthase enzymes that generate $O_2^{\bullet-}$ and NO, respectively, inside the vacuole (Fig. 5.1).[1,12,22] These two primary species react individually or cross-react to generate the oxidative burst cocktail composed of H_2O_2, ONO_2^-, NO and NO_2^-, which are detected outside the cell cytoplasmic membrane when the vacuoles fuse with it.[6-8,22] Among these species, NO and ONOOH can rapidly diffuse across biological membranes[13,14] into the cell cytoplasm (hence giving rise also to NO_2^-, the product of peroxynitrite decomposition). In agreement with previous qualitative observations,[9-12] our experiments suggest that the transient oxidative bursts detected inside macrophages represent the leakage of these species from vacuoles before they can release

their load outside the cell (Fig. 5.1). The short duration of oxidative bursts monitored inside an activated macrophage, as compared to the responses recorded outside (Table 1), indicates that this cell can rapidly eliminate ROS/RNS, thus avoiding damage to its inside.

5.3 Experimental Setup

Chemicals: All aqueous solutions were prepared from deionized water (Milli-Q, Millipore Corp.). Phosphate buffered saline (PBS; pH 7.4; 0.137 M NaCl, 0.01 M Na_2HPO_4, and 0.003 M KCl) was prepared by dissolving tablets (Sigma) in water and used in experiments with ROS/RNS. Ferrocenemethanol from Aldrich (Milwaukee, WI) was recrystallized twice from acetone. Platinization solution contained 0.087 g hexachloroplatinic acid (Aldrich) and 0.0014 g lead(II) acetate trihydrate (Alfa Aesar) in 1 mL of water to which 36 mL PBS was added. Etching solution was prepared by mixing 60% (by volume) water, 30% 5 M $CaCl_2$, and 10% HCl. DEANONOate and sodium peroxynitrite in alkaline solution were purchased from Cayman Chemical.

Cell culture. The murine macrophage RAW 264.7 (American Type Culture Collection) cell line was cultured at 37°C under a 5 % CO_2 atmosphere in Dulbecco's modified Eagle's medium (DMEM) containing 1.0 g L^{-1} D-glucose and sodium pyruvate (Invitrogen). The medium was supplemented with 5% fetal bovine serum (Invitrogen) and 20 μg mL^{-1} gentamicin (Sigma). Confluent monolayers of RAW 264.7 cells were resuspended through trypsinisation and plated in tissue culture Petri dishes (Nunc; 35 mm diameter) 24 h prior to electrochemical studies.

Preparation of etched Pt nanoelectrodes. Disk-type, flat nanoelectrodes were prepared by pulling 25-μm-diameter annealed Pt wires into borosilicate glass capillaries with the help of a

P-2000 laser pipette puller (Sutter Instrument Co.) and polished under video microscopic control as described previously.[24] The RG (i.e., the ratio of glass radius to that of the Pt tip) varied from 5 to 10. The electrode radius was evaluated from steady-state voltammetry. The electrodes that exhibited good quality voltammetric response were etched with an alternating current of 1.5 V amplitude, 20 MHz frequency (Keithley 3940, multifunctional synthesizer), as described previously.[21] The etched electrode was cleaned by sonication in water during 5 s and imaged by the AFM to determine its radius and the recess depth. The fabrication of 10 μm platinized carbon fiber microelectrodes is described in *SI Appendix*.

AFM imaging and deposition control. An XE-120 scanning probe microscope (Park Systems) was employed for imaging nanoelectrodes and for *in-situ* control of Pt black deposition. PPP-NCHR AFM probes (Nanosensors) were used for non-contact imaging. The procedures for AFM imaging of nanoelectrodes either in air or in solution were developed recently. Briefly, a nanoelectrode was mounted vertically with its polished surface facing the AFM probe using a homemade sample holder, and the cantilever was positioned above it with the help of an optical microscope. In a non-contact mode, the tip was brought within a close proximity of the sample using the approach function, and then the nanoelectrode was moved laterally in 200 nm steps to bring the AFM probe to its apex. The travel direction was selected to effect z-axis retraction of the piezo actuator in a close-loop mode. This corresponded to sliding of the slanted tip surface along the edge of the glass insulating sheath of the electrode. When the piezo approached its upper limit, the z-stage motor was retracted by 1 μm to maintain the actuator within its range (12 μm).

Electrodeposition of Pt black into the etched cavity was carried out in a commercial liquid cell (Park Systems), which was mounted on the stage of the XE-120 scanning probe

microscope. The etched working electrode was biased to -100 ± 30 mV vs. Ag/AgCl reference in the platinization solution using an EI-400 potentiostat (Ensman Instruments). Slightly different potential values were used depending on the initial recess depth to keep deposition time close to 1 min (the larger the recess depth the slower the deposition process). The cavity filling was controlled by line scanning above the central portion of the etched nanoelectrode and monitoring the cavity depth as a function of time.

Fabrication of 10 μm platinized carbon fiber microelectrodes. The detailed procedure for the fabrication of 10 μm diameter platinized carbon electrodes was reported previously.[25.26] Briefly, individual carbon fibers (10 μm diameter; Thornel P-55S, Cytec Engineered Materials, West Paterson, New Jersey, USA) were aspirated into 1 mm diameter glass capillary tubing (GC120F-10, Clark Electromedical Instruments, Harvard Apparatus, Edenbridge, UK); each capillary was then pulled with a microelectrode puller (Model PB-7, Narishige, Tokyo, Japan). The carbon fiber protruding out of the glass tip was insulated by electrodepositing polyoxyphenylene for 3 min at +4 V vs. Pt wire quasi-reference electrode. The deposition solution contained 0.4 M allylamine, 0.23 M 2-allylphenol, and 0.23 M 2-butoxyethanol in water/methanol. After washing with distilled water, the polymer was reticulated at 150°C during 3 h. The tip of the ultramicroelectrode was polished and beveled at an angle of 45° and platinized by electrochemical reduction of hexachloroplatinate in the presence of lead acetate at -60 mV vs. SSCE. The process was interrupted after passing the desired amount of the electric charge, 30 μC.[26]

Voltammetry and electrochemical experiments with macrophages. A two-electrode setup was used for voltammetric experiments with a nanometer-sized Pt working electrode and a commercial Ag/AgCl reference. Steady-state voltammograms of either aqueous

ferrocenemethanol or ferrocene in acetonitrile were obtained for electrode characterization using a BAS 100B electrochemical workstation (Bioanalytical Systems). *In-vitro* voltammetry of ROS/RNS was performed using either a BAS 100B or an EA162 Picostat (eDAQ, Australia) with an e-corder 401 system and EChem software.

Experiments with macrophages were performed at room temperature (22 ± 1^{o}C) on the stage of an inverted microscope (Axiovert 135, Zeiss) placed in a Faraday cage. For intracellular detection, the platinized nanoelectrode was moved slowly with a micromanipulator (MHW-103, Narishige) towards the cell until it touched the membrane. It was then further lowered by 500 nm to penetrate the cell. With the MHW-103 Narishige micromanipulator this last movement could not be performed at a sufficiently slow rate as reported previously.[15] This explains why only ~20% of the insertions provided a perfect seal. In another ~50% experiments the seal seemed to be good, but was not sufficiently tight, as evidenced by a small (a few percent of that recorded in the external solution) $Ru(NH_3)_6^{3+}$ reduction wave obtained inside the cell. In remaining ~30% cases, the cell membrane was ruptured during the nanoelectrode insertion. The transients were recorded until the current attained a constant value corresponding to the baseline.

For extracellular detection of the ROS/RNS release induced by the nanoelectrode insertion, a 10-µm-diameter platinized carbon microelectrode[6-8] was initially positioned ~30 µm above the cell and polarized for 3 min before each measurement. Then, the working microelectrode tip was precisely positioned with the micromanipulator at a fixed distance (5 µm) above the surface of the macrophage. At this point, the nanoelectrode was positioned with the second micromanipulator between the microelectrode platinized surface and the cell and inserted, as described above in the case of intracellular measurements. In both cases, the subsequent release of ROS/RNS was detected in real time by chronoamperometry (AMU130

amperometer, Radiometer Analytical) at +850 mV vs. Ag/AgCl, i.e., sufficiently positive for the oxidation of all H_2O_2, $ONOO^-$, NO, and NO_2^- species. The current transients were recorded using a Powerlab 4SP D/A converter with a Chart 4.2 interface (ADInstruments). The same equipment was used to insert a nanoelectrode into the cell and record current vs. time dependences (digitized at 10 kHz).

In all cases, the total charge (Q), the maximum current (I_{max}) and the half-time width ($t_{1/2}$) were extracted from the response that corresponds to the overall oxidation processes occurring at the measurement potential.

5.4 Conclusion

The presented data supports the hypothesis of the ROS/RNS leakage from phagolysosomes. It also shows that a macrophage can avoid oxidative damage by rapidly reducing ROS/RNS concentration levels in its cytoplasm. One should notice that in our experiments the oxidative stress response was induced by mechanical stimulation of a macrophage in its rest state. However, if the efficiency of the ROS/RNS removal in activated macrophages performing phagocytosis is similar to that observed in this study, no cell damage should occur due to the leakage of ROS/RNS outside phagocytotic vacuoles.

Chapter I References

1. (a) Y. Shao, M. V. Mirkin, *J. Am. Chem. Soc.* **1997**, *119,* 8103.(b) Q. Li, S. Xie, Z. Liang, X. Meng, S. Liu, H. H. Girault, Y.Shao, *Angew. Chem. Int. Ed.* **2009**, *48*, 8010.
2. C. Morris, A. K. Friedman, L. A. Baker, *Analyst* **2010**, *135*, 2190.
3. P. K. Hansma, B. Drake, O. Marti, S. A. C. Gould, C. B. Prater, *Science* **1989**, *243*, 641.
4. C. X. Cai, Y. H. Tong, M. V. Mirkin, *J. Phys. Chem. B* **2004**, *108*, 17872.
5. (a) D. J. Comstock, J. W. Elam, M. J. Pellin, M. C. Hersam, *Anal. Chem.* **2010**, *82*, 1270. (b) Y. Takahashi, A. I. Shevchuk, P. Novak, Y. Murakami, H. Shiku, Y. E. Korchev, T. Matsue, *J. Am. Chem. Soc.* **2010**, *132*, 10118.
6. (a)P. J. Rodgers and S. Amemiya, *Y. Wang* and M. V. Mirkin *Anal. Chem.*, **2010**, *82*, 84. *(b)*Y. Wang, J. Velmurugan and M. V. Mirkin, P. J. Rodgers, J. Kim and S.Amemiya *Anal. Chem.*, **2010**, *82*, 77.
7. Y. Wang, T. Kakiuchi, F. Shigematsu and M. V. Mirkin *J. Am. Chem. Soc.*, **2010**, *132*, 16945.
8. Y. Wang, K. Kececi, M. V. Mirkin, V. Mani, N. Sardesai and J. F. Rusling, *Chem. Sci*., **2013** ,*4*, 655
9. F. O. Laforge, J. Velmurugan, Y. Wang and M. V. Mirkin, *Anal. Chem.*, **2009**, *81*, 3143
10. P. Elsamadisi, Y. Wang, J. Velmurugan, and M. V. Mirkin, *Anal. Chem*., **2011**, *83*, 671.
11. Y. Wang, K. Kececi, J. Velmurugan, M. V. Mirkin, submitted to *Chem. Sci.*
12. Sun, P.; Mirkin, M. V. Kinetics of Electron Transfer Reactions at Nanoelectrodes. *Anal. Chem.* **2006**, *78*, 6526.
13. Y. Wang, J.-M. Noel, J. Velmurugan, W. Nogala, M. V. Mirkin, C. Lu, M. G. Collignonl, F. Lemaître and C. Amatore *Proc. Nat. Acad. Sci.*, **2012**, *109*, 11534.
14. J. Velmurugan, *A dissertation submitted to the Graduate Faculty of Chemistry in partial fulfillment of the requirements for the degree of Doctor of Philosophy, The City University of New York*, **2012**
15. Manual of P-2000 laser puller from Sutter Instrument

16. Y. Shao, M. V. Mirkin, *Anal. Chem.* **1998**, *70*, 3155-3161.

17. Y. Yuan, Y. Shao, *J. Phys. Chem. B* **2002**, *106*, 7809-7814.

18. Amphlett, J. L.; Denuault, G. *J. Phys. Chem. B* **1998**, *102*, 9946–9951.

19. Zoski, C. G.; Mirkin, M. V. *Anal. Chem.* **2002**, *74*, 1986–1992.

20. Y. Wang, J. Velmurugan and M. V. Mirkin *Isr. J. Chem.*, **2010**, *50*, 291.

21. A. J. Bard, L. R. Faulkner, *Electrochemical Methods: Fundamentals and Applications*, 2nd ed., John Wiley & Sons, New York, **2001**.

22. K. B. Oldham, C. G. Zoski, *J. Electroanal. Chem.* **1988**, *256*, 11-19.

23. M. V. Mirkin, A. J. Bard, *Anal. Chem.* **1992**, 64, 2293.

24. P. Jing, M. Q. Zhang, H. Hu, X. D. Xu, Z. W. Liang, B. Li, L. Shen, S. B. Xie, C. M. Pereira, Y. H. Shao, *Angew. Chem. Int. Ed.* **2006**, *45*, 6861.

25. C. Wei, A. J. Bard, S. W. Feldberg, *Anal. Chem.* **1997**, *69*, 4627.

26. M. L. Kovarik, K. Zhou, S. C. Jacobson, *J. Phys. Chem. B* **2009**, *113*, 15960.

27. H. S. White, A. Bund, *Langmuir* **2008**, *24*, 2212.

28. N. Calander, *Anal. Chem.* **2009**, *81*, 8347.

29. G. Wang, B. Zhang, J. R. Wayment, J. M. Harris, H. S. White, *J. Am. Chem. Soc.* **2006**, *128*, 7679.

30. P. J. Rodgers, S. Amemiya, *Anal. Chem.* **2007**, *79*, 9276.

31. M. V. Mirkin, W. Nogala, J. Velmurugan and Y. Wang "Scanning Electrochemical Microscopy in the 21st Century. Update 1: Five Years After." *Phys. Chem. Chem. Phys.,* **2011**, ***13***, 21196.

32. T. Solomon and A. J. Bard, *Anal. Chem.* **1995**, *67*, 2787.

33. (a) Y. Shao, M. V. Mirkin, *J. Electroanal. Chem.* **1997**, *439*, 137. (b) Y. Shao, M. V. Mirkin, *J. Phys. Chem. B* **1998**, *102*, 9915.

34. P. Novak, C. Li, A. I.Shevchuk, R Stepanyan, M. Caldwell, S. Hughes, T. G. Smart, J. Gorelik, V. P. Ostanin, M. J. Lab, G. W. J. Moss, G. I. Frolenkov, D. Klenerman, Y. E. Korchev, *Nat. Methods* **2009**, *6*, 279.

35. D. Zhan, X. Li, W. Zhan, F-R. F. Fan, and A. J. Bard, *Anal. Chem*. **2007**, *79*, 5225.

36. R. Ishimatsu, J. Kim, P. Jing, C. C. Striemer, D. Z. Fang, P. M. Fauchet, J. L. McGrath, and S. Amemiya, *Anal. Chem.* **2010**, *82*, 7127.

37. Y. Yatziv, I. Turyan and D. Mandler *J. Am. Chem. Soc.* **2002**, *124*, 5618.

38. C. L. Lin, J. Rodriguez-Lopez, and A.J. Bard, *Anal. Chem.* **2009**, *81*, 8868.

39. D. A. Walsh, J. L. Fernandez, J. Mauzeroll and A. J. Bard, *Anal. Chem.* **2005**, *77*, 5182.

40. C. G. Williams, M. A. Edwards, A. L. Colley, J. V. Macpherson, and P. R. Unwin, *Anal. Chem.* **2009**, *81,* 2486.

41. P. Sun, F. O. Laforge, T. P. Abeyweera, S.A. Rotenberg, J. Carpino, and M. V. Mirkin. *Proc Natl Acad Sci USA* **2008**, *105*, 443

42. B. Liu, S.A. Rotenberg, M.V. Mirkin *Proc Natl Acad Sci USA* **2000**, *97*, 9855

Chapter II References

2.1

1. (a) H. H. Girault, In *Modern Aspects of Electrochemistry*; R. E. White, B. E. Conway, J. O. M Brockris, Eds.; Plenum Press: New York, **1993**; Vol. 25, pp 1–62.
2. Z. Samec, T. Kakiuchi, In *Advances in Electrochemical Science and Electrochemical Engineering*; Gerischer, H., Tobias, C. W., Eds.; VCH: New York, **1995**; Vol. 4, pp 297.
3. I. Benjamin, *Ann. Rev. Phys. Chem.* **1997**, *48*, 407.
4. F. Scholz, *Annual Reports on the Progress of Chemistry*; Royal Society of Chemistry: London, **2006**.
5. F. Reymond, D. Fermin, H. J. Lee, H. H. Girault, *Electrochimica Acta* **2000**, *45*, 2647.
6. P. Vanysek, *Trends Anal. Chem.* **1993**, *12*, 357.
7. G. Taylor, H. H. Girault, *J. Electroanal. Chem.* **1986**, *208*, 179.
8. Y. Shao, M. V. Mirkin, *J. Am. Chem. Soc.* **1997**, *119*, 8103.
9. B. Liu, M. V. Mirkin, *Electroanalysis* **2000**, *12*, 1433.
10. P. Jing, P. J. Rodgers, S. Amemiya, *J. Am. Chem. Soc.* **2009**, *131*, 2290.
11. R. Cui, Q. Li, D. E. Gross, X. Meng, B. Li, M. Marquez, R. Yang, J. L. Sessler, Y. Shao, *J. Am. Chem. Soc.* **2008**, *130*, 14364.
12. P. J. Rodgers, S. Amemiya, *Anal. Chem.* **2007**, *79*, 9276.
13. S. Amemiya, X. Yang, T. L. Wazenegger, *J. Am. Chem. Soc.* **2003**, *125*, 11832.
14. P. J. Rodgers, P. Jing, Y. Kim, S. Amemiya, *J. Am. Chem. Soc.* **2008**, *130*, 7436.
15. P. Jing, Y. Kim, S. Amemiya, *Langmuir*, 2009, 25, pp 13653
16. Y. Yuan, Y. H. Shao, *J. Phys. Chem. B* **2002**, *106*, 7809.
17. P. Jing, M. Q. Zhang, H. Hu, X. D. Xu, Z. W. Liang, B. Li, L. Shen, S. B. Xie, C. M. Pereira, Y. H. Shao, *Angew. Chem. Int. Ed.* **2006**, *45*, 6861.
18. Cai, C. X.; Tong, Y. H.; Mirkin, M. V. *J. Phys. Chem. B* **2004**, *108*, 17872.
19. Laforge, F. O.; Sun, P.; Mirkin, M. V. *J. Am. Chem. Soc.* **2006**, *128*, 15019.
20. Sun, P.; Laforge, F. O.; Mirkin, M. V. *J. Am. Chem. Soc.* **2007**, *129*, 12410.

21. Q. Li, S. Xie, Z. Liang, X. Meng, S. Liu, H. H. Girault, Y. Shao, *Angew. Chem. Int. Ed*., **2009**, *48*, 8010
22. Y. Shao, M. V. Mirkin, *J. Phys. Chem. B* **1998**, *102*, 9915.
23. P. Sun, Z. Q. Zhang, Z. Gao, Y. H. Shao, *Angew. Chem. Int. Ed.* **2002**, *41*, 3445.
24. G. M. Luo, S. Malkova, J. Yoon, D. G. Schultz, B. H. Lin, M. Meron, I. Benjamin, P. Vanysek, M. L. Schlossman, *Science* **2006**, *311*, 216.
25. G. M. Luo, S. Malkova, J. Yoon, D. G. Schultz, B. H. Lin, M. Meron, I. Benjamin, P.;Vanysek, M. L. Schlossman, *J. Electroanal. Chem.* **2006**, *593*, 142.
26. G. M. Luo, S. Malkova, S. V. Pingali, D. G. Schultz, B. H. Lin, M. Meron, I. Benjamin, P. Vanysek, M. L. Schlossman, *J. Phys. Chem. B* **2006**, *110*, 4527
27. K. Schweighofer, I. Benjamin, *J. Phys. Chem. A* **1999**, *103*, 10274.
28. R. A. Marcus, *J. Chem. Phys.* **2000**, *113*, 1618.
29. Z. Samec, V. Marecek, *J. Electroanal. Chem.* **1986**, *200*, 17.
30. T. Wandlowski, V. Marecek, K. Holub, Z. Samec, *J. Phys. Chem.* **1989**, *93*, 8204.
31. T. Wandlowski, V. Marecek, Z. Samec, R. Fuoco, *J. Electroanal. Chem.* **1992**, *331*, 765.
32. V. Marecek, A. Lhotský, S. Racinský, *Electrochim. Acta* **1995**, *40*, 2905.
33. A. Lhotsky, K. Holub, P. Neuzil, V. Marecek, *J. Chem. Soc. Faraday Transac.* **1996**, *92*, 3851.
34. T. Kakiuchi, J. Noguchi, M. Kotani, M. Senda, *J. Electronanal. Chem.* **1990**, *296*, 517.
35. T. Kakiuchi, J. Noguchi, M. Senda, *J. Electroanal. Chem.* **1992**, *336*, 137.
36. T. Kakiuchi, Y. Teranishi, *J. Electroanal. Chem.* **1995**, *396*, 401.
37. M. Aminur Rahman, H. Doe, *J. Electroanal. Chem.* **1997**, *424*, 159.
38. Z. Samec, *Electrochim. Acta* **1998**, *44*, 85.
39. Y. Shao, M. V. Mirkin, *Anal. Chem.* **1998**, *70*, 3155.
40. S. Amemiya, A. J. Bard, *Anal. Chem.* **2000**, *72*, 4940
41. N. Tsujioka, S. Imakura, N. Nishi, T. Kakiuchi, *Anal. Sci.* **2006**, *22*, 667.
42. N. Nishi, S. Imakura, T. Kakiuchi, *J. Electroanal. Chem.* **2008**, *621*, 297.

43. P. J. Rodgers and S. Amemiya, Y. Wang and M. V. Mirkin *Anal. Chem.*, **2010**, *82*, 84.

44. Y. Shao, H. H. Girault, *J. Electroanal. Chem.* **1991**, *282*, 59.

45. J. L. Amphlett, Denuault, G. *J. Phys. Chem. B* **1998**, *102*, 9946.

46. C. G. Zoski, M. V. Mirkin, *Anal. Chem.* **2002**, *74*, 1986.

47. F. O. Laforge, J. Velmurugan, Y. Wang, Mirkin, M. V. *Anal. Chem.* **2009**, *81*, 3143.

2.2

1. D. R. MacFarlane, M. Forsyth, P. C. Howlett, J. M. Pringle, J. Sun, G. Annat, W. Neil, E. I. Izgorodina *Acc. Chem. Res.* **2007**, *40*, 1165.
2. X. Han, D. W. Armstrong, *Acc. Chem. Res.* **2007**, *40*, 1079.
3. *Electrochemical aspects of ionic liquids* (Ohno, H., Ed.); Wiley, Hoboken, 2005.
4. P. Hapiot, C. Lagrost, *Chem. Rev.* **2008**, *108*, 2238.
5. (a) A. A. Kornyshev, *J. Phys. Chem. B* **2007**, *111*, 5545. (b) M. V. Fedorov, A.A.
6. Kornyshev, *Electrochim. Acta* **2008**, *53*, 6835. (c) M. V. Fedorov, A. A. Kornyshev, *J. Phys. Chem. B* **2008**, *112*, 11868.
7. M. M. Islam, M. T. Alam, T. Okajima, T. Ohsaka, *J. Phys. Chem. C* **2009**, *113*, 3386.
8. (a) F. O. Laforge, T. Kakiuchi, F. Shigematsu, M. V. Mirkin, *J. Am. Chem. Soc.* **2004**, *126*, 15380. (b) F. O. Laforge, T. Kakiuchi, F. Shigematsu, M. V. Mirkin, *Langmuir* **2006**, *22*, 10705.
9. N. Nishi, H. Murakami, S. Imakura, T. Kakiuchi, *Anal. Chem.*, **2006**, *78*, 5805.
10. (a) Y. Yasui, Y. Kitazumi, R. Ishimatsu, N. Nishi, T. Kakiuchi, *J. Phys. Chem. B* **2009,** *113,* 3273. (b) T. Kakiuchi, Y. Yasui, Y. Kitazumi, N. Nishi, *ChemPhysChem, in press.*
11. For review of IT processes at the ITIES see (a) H. H. Girault in Modern Aspects of Electrochemistry, Vol. *25* (J. O'M. Bockris, B. E. Conway, R. E. White, Eds.), Plenum Press, New York, 1993, p. 1. (b) P. Vanýsek in Biomembrane Electrochemistry, (Blank, M.; Vodyanoy, I., Eds.) ACS, Washington, 1994, p. 55. (c) Z. Samec, T. Kakiuchi in

Advances in Electrochemical Science and Electrochemical Engineering, Vol. *4* (H. Gerischer, C. W. Tobias, Eds.), VCH, New York, 1995, p. 297. (d) R. A. W. Dryfe in Advances in Chemical Physics, V. 141, Wiley-Interscience, New York, 2009, p. 153.

12. N. Nishi, S. Imakura, T. Kakiuchi, *Anal. Chem.* **2006**, *78*, 2726.
13. (a) A. J. Bard, L. R. Faulkner *Electrochemical Methods: Fundamentals and Applications*; 2nd ed.; Wiley & Sons: New York, 2001. (b) M. V. Mirkin, A. J. Bard *Anal. Chem.* **1992**, *64*, 2293.
14. Y. Shao, M. V. Mirkin, *J. Am. Chem. Soc.* **1997**, *119*, 8103.
15. Y. Yuan, Y. H. Shao, *J. Phys. Chem. B* **2002**, *106*, 7809.
16. P. Jing, M. Q. Zhang, H. Hu, X. D. Xu, Z. W. Liang, B. Li, L. Shen, S. B. Xie, C. M. Pereira, Y. H. Shao, *Angew. Chem. Int. Ed.* **2006**, *45*, 6861.
17. C. X. Cai, Y. H. Tong, M. V. Mirkin, *J. Phys. Chem. B* **2004**, *108*, 17872.
18. Q. Li, S. Xie, Z. Liang, X. Meng, S. Liu, H. H. Girault, Y. Shao, *Angew. Chem. Int. Ed*. **2009**, *48*, 8010.
19. Y. Wang, J. Velmurugan, M. V. Mirkin, P. J. Rodgers, J. Kim, S. Amemiya, *Anal. Chem.* **2010**, *82*, 77.
20. A. A. Stewart, G. Taylor, H. H. Girault, J. McAleer, *J. Electroanal. Chem.* **1990**, *296*, 491.
21. Y. Tong, Y. Shao, E. Wang, *Anal. Chem.* (in Chin.) **2001**, *11*, 1241.
22. P. J. Rodgers, S. Amemiya, *Anal. Chem.* **2007**, *79*, 9276.
23. N. Tsujioka, S. Imakura, N. Nishi, T. Kakiuchi, *Anal. Sci.* **2006**, *22*, 667.
24. N. Nishi, S. Imakura, T. Kakiuchi, *J. Electroanal. Chem.* **2008**, *621*, 297
25. P. J. Rodgers, S. Amemiya, Y. Wang, M. V. Mirkin, *Anal. Chem.* **2010**, *82*, 84.
26. Y. Shao, H. H. Girault, *J. Electroanal. Chem.* **1991**, *282*, 59.
27. Y. Shao, M. V. Mirkin, *Anal. Chem.* **1998**, *70*, 3155.
28. K. R. J. Lovelock, F. N. Cowling, A. W. Taylor, P. Licence, D. A. Walsh, *J. Phys. Chem. B* **2010,** *114,* 4442.

29. F. O. Laforge, J. Velmurugan, Y. Wang, M. V. Mirkin, *Anal. Chem.* **2009,** *81,* 3143.

30. J. A. Manzanares, R. Lahtinen, B. Quinn, K. Kontturi, D. J. Schiffrin *Electrochim. Acta* **1998**, *44*, 59.

31. A. Menjoge, J. Dixon, J.F. Brennecke, E. J. Maginn, S. Vasenkov, *J. Phys. Chem. B* **2009,** *113,* 6353.

32. (a) C. P. Smith, H. S. White, *Anal. Chem.* **1993**, *65*, 3343-3353. (b) R. He, S. Chen, F. Yang, B. Wu, *J. Phys. Chem. B* **2006**, *110*, 3262. (c) Y. Liu, R. He, Q. Zhang, S. Chen, *J. Phys. Chem. C* **2010**, *114*, 10812.

33. T. Kakiuchi, *J. Electroanal. Chem.* **1992**, *322*, 55.

34. K. Kontturi, J. A. Manzanares, L. Murtomaki, D. J. Schiffrin, *J. Phys. Chem.* **1997**, *101*, 10801.

35. W. Schmickler, *J. Electroanal. Chem.* **1997**, *426*, 5.

36. R. A. Marcus, *J. Chem. Phys.* **2000**, *113*, 1618.

37. N. Nishi, K. Izawa, M. Yamamoto, T. Kakiuchi, *J. Phys. Chem. B* **2001,** *105,* 8162.

38. Y. Wang, J. Velmurugan, M. V. Mirkin, *Isr. J. Chem.*, **2010**, *50*, 291

39. C. Wei, A. J. Bard, S. W. Feldberg, *Anal. Chem.* **1997**, *69*, 4627.

40. H. S. White, A. Bund, *Langmuir* **2008**, *24*, 2212.

41. G. Wang, B. Zhang, J. R. Wayment, J. M. Harris, H. S. White, *J. Am. Chem. Soc.* **2006**, *128*, 7679.

42. (a) B. L. Bhargava, S. Balasubramanian, *J. Am. Chem. Soc.* **2006**, *128*, 10073. (b) D. Roy, N. Patel, S. Conte, M. Maroncelli, *J. Phys. Chem. B*, **2010**, *114*, 8410.

43. J. Bowers, M. C. Vergara-Gutierrez, J. R. P. Webster, *Langmuir* **2004**, *20*, 309.

44. M. Mezger, H. Schröder, H. Reichert, S. Schramm, J. S. Okasinski, S. Schöder, V. Honkimaki, M. Deutsch, B. M. Ocko, J. Ralston, M. Rohwerder, M. Stratmann, H. Dosch, *Science* **2008**, *322*, 424.

Chapter III References

3.1

1. (a) S. Amemiya, A. J. Bard, F.-R. F. Fan, M. V. Mirkin, and P. R. Unwin, *Annu. Rev. Anal. Chem.* **2008**, *1*, 95 (b) F. O. Laforge, P. Sun, and M. V. Mirkin, *In Advances in Chemical Physics*; S. A. Rice, Ed.; Wiley & Sons, **2008**; Vol. 139, p 177
2. (a) Y. Shao, and M. V. Mirkin, *J. Am. Chem. Soc.* **1997**, 119, 8103(b) Y. Shao, and M. V. Mirkin, *J. Phys. Chem. B* **1998**, 102, 9915(c) C. Cai, Y. Tong, and M. V. Mirkin, *J. Phys. Chem. B* **2004**, 108, 17872
3. *Scanning Electrochemical Microscopy*; A. J. Bard, M. V. Mirkin, Eds.; Marcel Dekker: New York, **2001**.
4. Y. Shao, M. V. Mirkin, *J. Am. Chem. Soc.* **1997**, *119*, 8103.
5. Q. Li, S. Xie, Z. Liang, X. Meng, S. Liu, H. H. Girault, Y. Shao, *Angew. Chem. Int. Ed*. **2009**, *48*, 8010.
6. (a) C. X. Cai, Y. H. Tong, M. V. Mirkin, *J. Phys. Chem. B*. **2004**, *108*, 17872. (b) C. X. Cai, M. V. Mirkin, *J. Am. Chem. Soc.* **2006**, *128*, 171.
7. (a) Y. Shao, M. V. Mirkin, G. Fish, S. Kokotov, D. Palanker, A. Lewis, *Anal. Chem.* **1997**, *69*, 1627. (b) P. Sun, M. V. Mirkin, *Anal. Chem.* **2006**, *78*, 6526.
8. Y. Shao, H. H. Girault, *J. Electroanal. Chem.* **1991**, *282*, 59.
9. Y. Wang, J. Velmurugan, M. V. Mirkin, P. J. Rodgers, J. Kim, S. Amemiya, *Anal. Chem.* **2010**, *82*, 77.
10. R. Cornut, C. Lefrou, *J. Electroanal. Chem.* **2007**, *608*, 59.
11. M. V. Mirkin, F.- R. F. Fan, A. J. Bard, *Science* **1992**, *257*, 364.
12. (a) P. K. Hansma, B. Drake, O. Marti, S. A. C. Gould, and C. B. Prater, Science **1989**, *243*, 641 (b) Y. E. Korchev, C. L. MBashford, M. Milovanovic, I. Vodyanoy, and M. Lab, *J. Biophys. J.* **1997**, *7*, 653

3.2

1. *Scanning Electrochemical Microscopy* (A. J. Bard, M. V. Mirkin, Eds.), 2nd Ed., CRC Press: Boca Raton, FL, 2012.
2. M. V. Mirkin, W. Nogala, J. Velmurugan and Y. Wang, *Phys. Chem. Chem. Phys*., **2011**, *13*, 21196.
3. (a) P. Bertoncello, *Energy Environ. Sci*., **2010**, *3*, 1620; (b) S. C. S Lai, J. V. Macpherson and P. R. Unwin, *MRS Bulletin*, 2012**,** *37*, 668.
4. (a) A. Schulte, M. Nebel and W. Schuhmann, *Annu. Rev. Anal. Chem.*, **2010**, *3*, 299; (b) I. Beaulieu, S. Kuss, J. Mauzeroll and M. Geissler, *Anal. Chem.*, **2011**, *83*, 1485.
5. Y. Takahashi, A. I. Shevchuk, P. Novak, B. Babakinejad, J. Macpherson, P. R. Unwin, H. Shiku, J. Gorelik, D. Klenerman, Y. E. Korchev and T. Matsue, *Proc. Natl. Acad. Sci. USA*, **2012**, *109*, 11540 and references cited therein.
6. G. Wittstock, M. Burchardt, S. E. Pust, Y. Shen and C. Zhao, *Angew. Chem. Int. Ed.*, **2007**, *46,* 1584.
7. (a) D. O. Wipf, A. J. Bard, *Anal. Chem.*, **1992**, *64*, 1362; (b) D. O.Wipf, A. J. Bard and D. E. Talman, *Anal. Chem*., **1993**, *65*, 1373; (c) M. A. Edwards, A. L. Whitworth and P. R. Unwin, *Anal. Chem.*, **2011**, *83*, 1977.
8. A. Hengstenberg, C. Kranz and W. Schuhmann, *Chem.–Eur. J.*, **2000**, *6*, 1547.
9. (a) K. Eckhard, M. Etienne, A. Schulte and W. Schuhmann, *Electrochem. Commun.*, **2007**, *9*, 1793; (b) P. M. Diakowski, Z. F. Ding, *Electrochem. Commun.*, **2007**, *9*, 2617; (c) P. M. Diakowski, Z. F. Ding, *Phys. Chem. Chem. Phys.*, **2007**, *9*, 5966; (d) K. Eckhard, W. Schuhmann, *Analyst*, **2008**, *133*, 1486.
10. L. Q. Wang, C. Kranz and B. Mizaikoff, *Anal. Chem.*, **2010**, *82*, 3132.
11. K. McKelvey, M. A. Edwards and P. R. Unwin, *Anal. Chem.*, **2010**, *82*, 6334.
12. S. Isik, M. Etienne, J. Oni, A. Blochl, S. Reiter, W. Schuhmann, *Anal Chem*, **2004,** *76*, 6389.

13. Y. Takahashi, A. I. Shevchuk, P. Novak, Y. Zhang, N. Ebejer, J. Macpherson, P. R. Unwin, A. J. Pollard, D. Roy, C. A. Clifford, H. Shiku, T. Matsue, D. Klenerman and Y. E. Korchev, *Angew. Chem. Int. Ed.*, **2011**, *50*, 9638.
14. (a) D. J. Comstock, J. W. Elam, M. J. Pellin and M. C. Hersam, *Anal. Chem.*, **2010**, *82*, 1270; (b) Y. Takahashi, A. I. Shevchuk, P. Novak, Y. Murakami, H. Shiku, Y. E. Korchev and T. Matsue, *J. Am. Chem. Soc.*, **2010**, *132*, 10118.
15. S. Kuss, R. Cornut, I. Beaulieu, M. A. Mezour, B. Annabi and J. Mauzeroll, *Bioelectrochemistry*, **2011**, *82*, 29.
16. A. J. Bard, M. V. Mirkin, P. R. Unwin and D. O. Wipf, *J. Phys. Chem.*, **1992**, *96*, 1861.
17. R. C. Engstrom, B. Small and L. Kattan, *Anal. Chem.*, **1992**, *64*, 241.
18. (a) G. Wittstock, W. Schuhmann, *Anal. Chem.*, **1997**, *69*, 5059; (b) A. Minguzzi, M. A. Alpuche-Aviles, J. Rodríguez López, S. Rondinini, A. J. Bard, *Anal. Chem.*, **2008**, *80*, 4055.
19. Y. Yatziv, I. Turyan and D. Mandler, *J. Am. Chem. Soc.*, **2002**, *124*, 5618.
20. C. L. Lin, J. Rodriguez-Lopez and A. J. Bard, *Anal. Chem.*, **2009**, *81*, 8868.
21. D. A. Walsh, J. L. Fernandez, J. Mauzeroll and A. J. Bard, *Anal. Chem.*, **2005**, *77*, 5182.
22. (a) A. Bruckbauer, L. Ying, A. M. Rothery, D. Zhou, A. I. Schevchuk, C. Abell, Y. E. Korchev and D. Klenerman, *J. Am. Chem. Soc.*, **2002**, *124*, 8810; (b) A. Bruckbauer, D. Zhou, L. Ying, Y. E. Korchev, C. Abell and D. Klenerman, *J. Am. Chem. Soc.*, **2003**, *125*, 9834; (c) K. T. Rodolfa, A. Bruckbauer, D. Zhou, Y. E.Korchev, D. Klenerman, *Angew. Chem. Int. Ed.*, **2005**, *44*, 6854; (d) K. T. Rodolfa, A. Bruckbauer, D. Zhou, A. I. Schevchuk, Y. E. Korchev, D. Klenerman, *Nano Lett.*, **2006**, *6*, 252.
23. C. G. Williams, M. A. Edwards, A. L. Colley, J. V. Macpherson and P. R. Unwin, *Anal. Chem.*, **2009**, *81*, 2486.
24. (a) Y. Shao, M. V. Mirkin, *J. Phys. Chem. B*, **1998**, *102*, 9915; (b) C. Cai, Y. Tong, M. V. Mirkin, *Phys. Chem. B*, **2004**, *108*, 17872.

25. (a) J. L. Amphlett, G. Denuault, *J. Phys. Chem. B*, **1998**, *102*, 9946; (b) R. Cornut, C. Lefrou, *J. Electroanal. Chem.*, **2007**, *608,* 59.

26. (a) P. J. Rodgers, S. Amemiya, *Anal. Chem.*, **2007**, *79*, 9276; (b) P. J. Rodgers, S. Amemiya, Y. Wang, M. V. Mirkin, *Anal. Chem.* **2010**, *82*, 84.

27. D. A. Treichel, M. V. Mirkin, A. J. Bard, *J. Phys. Chem.,* **1994**, *98*, 5751.

28. J. Kim, M. Shen, N. Nioradze, S. Amemiya, *Anal. Chem.*, **2012**, *84*, 3489.

29. F. O. Laforge, J. Velmurugan, Y. Wang and M. V. Mirkin, *Anal. Chem.*, **2009**, *81*, 3143.

Chapter IV References

1. (a) L. T. Sexton, L. P. Horne, C. R. Martin, *Mol. BioSyst.* **2007**, *3*, 667. (b) J. Griffiths, *Anal. Chem*. **2008**, *80*, 23. (c) S. Howorka, Z. Siwy, *Chem. Soc. Rev.* **2009**, *38*, 2360.
2. (a) J. J. Kasianowicz, E. Brandin, D. Branton, D. W. Deamer, *Proc. Nat. Acad. Sci. USA* **1996**, *93,* 13770. (b) H. Bayley, P. S. Cremer, *Nature* **2001**, *413*, 226. (c) S. Majd, E. C. Yusko, Y. N. Billeh, M. X. Macrae, J. Yang, M. Mayer, *Curr. Opin. Biotechnol.* **2010**, *21*, 439.
3. (a) T. Ito, L. Sun, R. R. Henriquez, R. M. Crooks, *Acc. Chem. Res.* **2004**, *37*, 937. (b) Y. Choi, L. A. Baker, H. Hillebrenner, C. R. Martin, *Phys. Chem. Chem. Phys.* **2006**, *8*, 4976.
4. D. Branton, D. W. Deamer, A. Marziali, H. Bayley, S. A. Benner, T. Butler, M. Di Ventra, S. Garaj, A. Hibbs, X. Huang, S. B. Jovanovich, P. S. Krstic, S. Lindsay, X. S. Ling, C. H. Mastrangelo, A. Meller, J. S. Oliver, Y. V. Pershin, J. M. Ramsey, R. Riehn, G. V. Soni, V. Tabard-Cossa, M. Wanunu, M. Wiggin, J. A. Schloss, *Nat. Biotechnol.* **2008**, *26*, 1146.
5. (a) R. Fan, R. Karnik, M. Yue, D. Li, A. Majumdar, P. Yang, *Nano Lett.* **2005**, *5*, 1633. (b) M. Gershow, J. A. Golovchenko, *Nat. Nanotechnol.* **2007**, *2*, 775. (c) S. W. Kowalczyk, L. Kapinos, T. R. Blosser, T. Magalhães, P. van Nies, R. Y. H. Lim, C. Dekker, *Nat. Nanotechnol.* **2011**, *6*, 433.
6. (a) J. H. Shim, J. Kim, G. S. Cha, H. Nam, R. J. White, H. S. White, *Anal. Chem.* **2007**, *79*, 3568. (b) C. Song, B. Corry, *J. Phys. Chem. B* **2009**, *113*, 7642.
7. E. A. Heins, Z. S. Siwy, L.A. Baker, C. R. Martin, *Nano Lett.* **2005**, **5**, 1824.
8. C. R. Martin, Z. S. Siwy, *Science* **2007**, *317*, 331.
9. (a) R. J. White, E. N. Ervin, T. Yang, X. Chen, S. Daniel, P. S. Cremer, H. S. White, *J. Am. Chem. Soc.* **2007**, *129*, 11766. (b) A. E. P. Schibel, T. Edwards, R. Kawano, W. Lan, H. S. White, *Anal. Chem.* **2010**, *82*, 7259.
10. H. Bayley, C. R. Martin, *Chem. Rev.* **2000**, *100*, 2575.

11. M. Karhanek, J. T. Kemp, N. Pourmand, R. W. Davis, C. D. Webb, *Nano Lett.* **2005**, *5,* 403.

12. H. Liu, R. Malhotra, M. W. Peczuh, J. F. Rusling, *Anal. Chem.* **2010**, *82*, 5865.

13. S. H. Shreffler, A. Munoz-Furlong, H. A. Sampson, *J. Allergy Clin. Immunol.* **2003**, *112*, 1203.

14. (a) S. J. Koppelman, M. Wensing, M. Ertmann, A. C. Knulst, E. F. Knol, *Clin. Exp. Allergy* **2004**, *34*, 583. (b) W. G. Shreffler, D. A. Lencer, L. Bardina, H. A. Sampson, *J. Allergy Clin. Immunol.* **2005**, *116*, 893.

15. G. W. Warr, K. E. Magor, D. A. Higgins, *Immunol. Today* **1995**, *16*, 392.

16. (a) H. Chang, F. Kosari, G. Andreadakis, M. A. Alam, G. Vasmatzis, R. Bashir, *Nano Lett.* **2004**, *4*, 1551. (b) R. M. M. Smeets, U. F. Keyser, D. Krapf, M.-Y. Wu, N. H. Dekker, C. Dekker, *Nano Lett.* **2006**, *6*, 89.

17. C. Morris, A. K. Friedman, L. A. Baker, *Analyst* **2010**, *135*, 2190.

18. (a) Y. Shao, M. V. Mirkin, *J. Am. Chem. Soc.* **1997**, *119,* 8103.(b) Q. Li, S. Xie, Z. Liang, X. Meng, S. Liu, H. H. Girault, Y.Shao, *Angew. Chem. Int. Ed.* **2009**, *48*, 8010.

19. P. K. Hansma, B. Drake, O. Marti, S. A. C. Gould, C. B. Prater, *Science* **1989**, *243*, 641.

20. C. X. Cai, Y. H. Tong, M. V. Mirkin, *J. Phys. Chem. B* **2004**, *108*, 17872.

21. (a) D. J. Comstock, J. W. Elam, M. J. Pellin, M. C. Hersam, *Anal. Chem.* **2010**, *82*, 1270. (b) Y. Takahashi, A. I. Shevchuk, P. Novak, Y. Murakami, H. Shiku, Y. E. Korchev, T. Matsue, *J. Am. Chem. Soc.* **2010**, *132*, 10118.

22. C. Gao, S. Ding, Q. Tan, L.-Q. Gu, *Anal. Chem.* **2009**, *81*, 80.

23. S. Umehara, M. Karhanek, R. W. Davis, N. Pourmand, *Proc. Nat. Acad. Sci. USA* **2009**, *106*, 4611.

24. P. D. Beattie, A. Delay, H. H. Girault, *J. Electroanal. Chem.* **1995**, *380*, 167.

25. (a) F. O. Laforge, J. Carpino, S. A. Rotenberg, M. V. Mirkin *Proc. Nat. Acad. Sci. USA* **2007**, *104*, 11895. (b) P. J. Rodgers, S.Amemiya, *Anal. Chem.* **2007**, *79*, 9276. (c) P. J. Rodgers, S. Amemiya, Y. Wang, M. V. Mirkin, *Anal. Chem.* **2010**, *82*, 84.

26. (a) C. Wei, A. J. Bard, S. W. Feldberg, *Anal. Chem.* 1997, **69**, 4627. (b) H. S. White, A. Bund, *Langmuir* **2008**, *14*, 2212. (c) J. P. Guerrette, B. Zhang, *J. Am. Chem. Soc.* **2010**, *132*, 17088. (d) J. Liu, M. Kvetny, J. Feng, D. Wang, B. Wu, W. Brown, G. Wang *Langmuir* **2012**, *28*, 1588.
27. J. Newman, K. E. Thomas-Alyea, *Electrochemical Systems*, John Wiley & Sons: Hoboken, **2004**, p. 424.
28. W.-J. Lan, D. A. Holden, B. Zhang, H. S. White, *Anal. Chem.* **2011**, *83*, 3840.
29. G. R. Willmott, B. E. T. Parry, *J. Appl. Phys.* **2011**, *109*, 094307.
30. J. C. Myland, K. B. Oldham, *J. Electroanal. Chem.* **1993**, *347*, 49.
31. R. Vogel, G. Willmott, D. Kozak, G. S. Roberts, W. Anderson, L. Groenewegen, B. Glossop, A. Barnett, A. Turner, M. Trau, *Anal. Chem.* **2011**, *83*, 3499.
32. M. Firnkes, D. Pedone, J. Knezevic, M. Döblinger, U. Rant, *Nano Lett.* **2010**, *10*, 2162.
33. H. S. White, private communication.
34. S. Krishnan, V. Mani, D. Wasalathanthri, C. V. Kumar, J. F. Rusling, *Angew. Chem. Int. Ed.* **2011**, *50*, 1175.
35. (a) K. Aslan, V. H. Perez-Luna, *Langmuir* **2002**, *18*, 6059. (b) K. Aslan, C. C. Luhrs, V. H. Perez-Luna, *J. Phys. Chem. B* **2004**, *108*, 15631.
36. K. Aslan, V. H. Perez-Luna, *J. Fluoresc.* **2004**, *14*, 401.
37. E. A. Heins, Z. S. Siwy, L.A. Baker, C. R. Martin, *Nano Lett.* **2005**, *5*, 1824.
38. J. Newman, K. E, Thomas-Alyea, *Electrochemical Systems*, John Wiley & Sons: Hoboken, **2004**, p. 424.
39. D. C. Harris, *Quantitative Chemical Analysis*, W.H. Freeman and Company, 6th edition, **2002**, p. 657.
40. J. Newman, *J. Electrochem. Soc*. **1966**, *113*,501.
41. M. Firnkes, D. Pedone, J. Knezevic, M. Döblinger, U. Rant, *Nano Lett.* **2010**, *10*, 2162.

Chapter V References

1. Bogdan C, M. Rollinghoff, A. Diefenbach, *Curr Opin Immunol,* **2000**, *12*, 64.
2. D.G. Russell, B.C. VanderVen, S. Glennie, H. Mwandumba, R.S. Heyderman *Nature Reviews Immunology* **2009**, *9*, 594.
3. F.C. Fang, *Nat Rev Microbiol*, **2004**, *2*, 820.
4. D.S. Schrock, J.E. Baur, *Anal Chem*, **2007**, *79*, 7053
5. C. Amatore, S. Arbault, M. Guille, F. Lemaître *Chem Rev,* **2008**, *108*, 2585.
6. C. Amatore, S. Arbault, D. Bruce, P. de Oliveira, M. Erard, M. Vuillaume, *Faraday Discuss*, **2000**, *116*, 319.
7. C.Amatore, S. Arbault, C. Bouton, K. Coffi, J-C. Drapier, H. Ghandour, Y. Tong, *ChemBioChem,* **2006**, *7*, 653.
8. C. Amatore, S. Arbault, C. Bouton, J-C. Drapier, H. Ghandour, A.C.W. Koh, *ChemBioChem,* **2008**, *9*, 1472.
9. E. Nilsson, R. Ghassemifar, U.T. Brunk, *Histochem J,* **1997**, *29*, 857.
10. U.T. Brunk, I. Svensson, *Redox Report* , **1999**, *4*, 3.
11. P. Cech, R.L. Lehrer, *Blood* , **1984**, *64*,147.
12. X.M. Yuan, W. Li, U.T. Brunk, H. Dalen, Y.H. Chang, A. Sevanian, *Free Radic Biol Med*, **2000**, *28*, 208.
13. A. Denicola, J.M. Souza, R. Radi, *Proc Natl Acad Sci USA*, **1998**, *95*, 3566.
14. A. Denicola, J.M. Souza, R. Radi, E. Lissi, *Arch Biochem Biophys,* **1996**, *328*, 208.
15. P. Sun, F.O. Laforge, T.P. Abeyweera, S.A. Rotenberg, J. Carpino, M.V. Mirkin, *Proc Nat Acad Sci USA*, **2008**, *105*, 443.
16. S. Arbault, P. Pantano, J.A. Jankowski, M. Vuillaume, C. Amatore, *Anal Chem*,**1995**, *67*, 3382.
17. J.M. Elliott, P.R. Birkin, P.N. Bartlett, G.S. Attard, *Langmuir*, **1999**, *15*, 7411.
18. S.A.G. Evans, J.M. Elliott, L.M. Andrews, P.N. Bartlett, P.J. Doyle, G. Denuault, *Anal Chem*, **2002**, *74*, 1322.

19. J.H. Shim, Y. Lee, *Anal Chem*, **2009**, *81*, 8571.

20. J. Velmurugan, M.V. Mirkin, *ChemPhysChem*, **2010**, *11*, 3011.

21. P. Sun, M.V. Mirkin, *Anal Chem*, **2007**, *79*, 5809.

22. C. Amatore, S. Arbault, D. Bruce, P. de Oliveira, M. Erard, M. Vuillaume, *Chem Eur J*, **2001**, *7*, 4171.

23. C. Amatore, S. Arbault, Y. Bouret, B. Cauli, M. Guille, A. Rancillac, J. Rossier, *ChemPhysChem*,**2006**, *7*,181.

24. P. Sun, M.V. Mirkin, *Anal Chem*, **2006**, *78*, 6526.

25. C. Amatore, S. Arbault, C. Bouton, K. Coffi, J-C. Drapier, H. Ghandour, Y. Tong, *ChemBioChem*, **2006**, *7*, 653.

26. S. Arbault, P. Pantano, J.A. Jankowski, M. Vuillaume, C. Amatore, Anal Chem, **1995**, *67*, 3382.